Numerical Simulation of Sand Retention Mechanisms

by

Seyedehfatemeh Razavi

A thesis submitted in partial fulfillment of the requirements for the degree of

Doctor of Philosophy

Department of Mechanical Engineering

University of Alberta

Abstract

The primary motivation of this research is to investigate the conditions and parameters that influence the formation, stabilization, destruction and reformation of the multi-particle sand arching (bridging) that occurs at the opening of the sand filters to support sand retention. In particular, this research will examine the performance of the multi-particle arch under transient fluid flow conditions.

The computational fluid dynamic (CFD) - discrete element method (DEM) model is applied to predict multi-particle arch formation, stabilization, breakage and reformation under steady and transient flow conditions of the well-bore. By using coupled CFD-DEM (CFD to model the fluid flow, and DEM to model the particle flow), the physics involved in the multi-particle arching phenomenon is studied and industry-relevant problems are investigated. The coarse grid unresolved and the smoothed unresolved (refined grid unresolved) coupling approaches implemented in STAR-CCM+ (SIEMENS PLM) are used to transfer data between the fluid and solid phases and calculate the forces. The filter slots under investigation have different geometries: straight, keystone, wire-wrapped screen (WWS) and seamed slot and the particles are considered with different shapes and different aspect ratios and size distributions. The flow regime is laminar in all simulations conducted.

The CFD-DEM model is validated from the perspectives of particle-fluid, particle-particle and particle-wall interactions. Verification of the CFD-DEM model is conducted by mesh sensitivity analysis to investigate the coupling resolution between the CFD and DEM.

Various simulations of the sand retention mechanisms with the slurry flow and unstable/stable packed-bed cases, under steady and transient flow conditions, at the opening of filters are conducted.

Surface deposition, size exclusion and sequential arching of particles are observed as retention mechanisms with the slurry flow, whereas multi-particle arching is observed in packed-beds only. The importance of the gravity force and interaction forces on retention mechanisms are confirmed at the micro-scale in comparison with the drag force, lift force, cohesive force, buoyancy force and virtual mass force. Multi-particle arching occurs after several particles flow through the opening. The ratio of the particle size to the sand screen opening is an important factor in arch formation.

At the micro-scale, multi-particle arching is controlled mainly by the particle interactions, particle concentration, and particle-domain interactions. The results confirm that bridge formation and stability are controlled by particle shape, relative slot size-to-particle size, and interaction forces between particles forming the bridge. The results also show that two forces are critical to forming the multi-particle arch: gravity force and interaction forces between the particles and particle-domain at the micro-scale. The results show that multi-particle arching is the result of particle interaction and surface deposition at the slot entrance.

Particle size distribution supports the multi-particle arch and the arch stays stable for a longer time than the case with the uniform-size distribution of particles. Particle shape affects the arch stability with non-spherical particles with sharp corners resulting in a more stable arch, as long as the aspect ratio

of particles is not too large.

A stable packed bed supports stabilization of the multi-particle arch. Instabilities caused by transient flow changes, such as flow interruptions, can result in arch breakage and increased sand production. A curved surface at the slot entrance, such as the modeled simplified seamed slot shape, can result in lower arch stability and more sand production.

Preface

This dissertation is original, and an independent work by the author, Fatemeh Razavi. Numerical simulations were validated by the collaborating experimental labs at the University of Alberta. From Dr. Nobes's group, Lisa Kinsale's particle shadowgraph velocimetry (PSV) results[1] [2] were used to validate the simulated retention mechanism and particle build-up around the filter opening. From Dr. Nouri's group, Chenxi Wang's experimental results[3] and[4] were used to validate the transient flow simulation results obtained in this research. Here is the list of documents published and/or accepted for publication out of this work.

1. Chapter 4 of the thesis has been partly accepted for publication as Fatemeh Razavi, Alexandra Komrakova and Carlos F. Lange, "CFD-DEM Simulation of Multi-particle Arching at Sand Filter Opening", Canadian Society for Mechanical Engineering Conference Proceeding, CSME 2021, (PhD Work), 2021. I was responsible for data collection, numerical simulations, analysis as well as the manuscript composition.

2. Chapter 4 of the thesis has been partly published as Fatemeh Razavi, Alexandra Komrakova and Carlos F. Lange, "Modeling Slurry Flow in Sand Filter: CFD-DEM Simulation", Proceedings of the 28^{th} Annual Conference of the Computational Fluid Dynamics Society of Canada, CFDSC2020, (PhD Work), 2020. I was responsible for data collection, numerical simulations, analysis as well as the manuscript composition.

3. Chapter 3 of the thesis has been partly published as Fatemeh Razavi,

Alexandra Komrakova and Carlos F. Lange, "Simulation of Bouncing Solid Particle in Oil: Spherical vs. Polyhedral Particle Shape Effect", Progress in Canadian Mechanical Engineering, Volume 3 by Canadian Society for Mechanical Engineering, CSME 2020, (PhD Work), 2020. I was responsible for data collection, numerical simulations, analysis as well as the manuscript composition.

4. Chapter 3 of the thesis has been partly published as Fatemeh Razavi, Alexandra Komrakova and Carlos F. Lange, "Coupled CFD-DEM Model to Simulate Two-Particle Settlement in a Newtonian Fluid: A Grid Comparison", Annual Conference of CFD Society of Canada, London, Ontario, (PhD Work), 2019. I was responsible for data collection, numerical simulations, analysis as well as the manuscript composition.

5. Chapter 3 of the thesis has been partly published as Fatemeh Razavi, Alexandra Komrakova and Carlos F. Lange, "CFD-DEM Model of Particulate Flow", Okanagan Fluid Dynamics Meeting, Canmore, Alberta, (PhD Work), 2019. I was responsible for data collection, numerical simulations, analysis as well as the manuscript composition.

6. Chapter 3 of the thesis has been partly published as Fatemeh Razavi, Alexandra Komrakova and Carlos F. Lange, "On the Fluid Mechanics of Wire-Wrap Screens in Horizontal Wells", 26^{th} Annual Conference of CFD Society of Canada, Winnipeg, Manitoba, (PhD Work), 2018. I was responsible for data collection, numerical simulations, analysis as well as the manuscript composition.

7. Chapter 3 of the thesis has been partly published as Fatemeh Razavi, Alexandra Komrakova and Carlos F. Lange, "On the CFD Simulation of the Wire-Wrapped Screen and Porous Media Around it", 67^{th} Canadian Chemical Engineering Conference, Edmonton, Alberta, (PhD Work), 2017. I was responsible for data collection, numerical simulations, analysis as well as the manuscript composition.

This project was recognized and supported by industry and academia through achieving 8 awards including Petro-Canada Graduate Scholarship in Petroleum Engineering for 3 consecutive years as well as Computational Fluid Dynamics (CFD) Society of Canada graduate scholarship award.

A graduate-level course syllabus was developed by the author out of this thesis under the UofA Graduate Teaching and Learning Program (GTLP), level 3.

There is no beauty better than intellect.

Prophet Muhammad (PBUH)

To God for his endless knowledge.

To the souls of my father and my grandfather for their wisdom.

To my mother, my grandmother and my aunt for their unconditional love.

To my husband and my daughter for their love and support.

To all women in STEM for their perseverance.

To Sana Charity Network for its life-changing philosophy.

To all victims of Ukraine Flight PS752 for the memories left behind.

To all healthcare workers during the COVID-19 pandemic for their sacrifices.

Acknowledgments

I would like to thank my supervisors, Dr. Carlos F. Lange and Dr. Alexandra Komrakova, for the patient guidance, encouragement and advice they have provided throughout my time as their student. I have been extremely lucky to have supervisors who cared so much about my work, and who responded to my questions and queries so promptly. I thank them for being wonderful mentors, and teachers to me. I would like to express my gratitude to Dr. Clayton V. Deutsch for his support and encouragement as my supervision committee member.

I would also like to express my gratitude to Natural Sciences and Engineering Research Council of Canada (NSERC) and RGL Reservoir Management Inc for their financial support.

I would like to offer my special thanks to my technical coaches, Dr. David Nobes, Dr. Dora Farkas, Dr. Kate Pratt and Dr. Deanna Davis, for their generous support, insightful comments and suggestions. I would like to express the deepest appreciation to my non-technical coaches, Jim Rohn, Dr. Steve Knish (Psychologist and Yoga instructor), Soodeh Heravi (Psychologist), Parastoo Karimzadeh-Naeim (Psychologist and mathematician), Mona Naseri (Yoga instructor) and Tayebe Joodaki (Painting instructor), for supporting my journey and being mentors and spiritual guide to me.

I would like to offer my special thanks to my colleagues, lab-mates and friends for their constructive comments and warm encouragement, particularly Niloofar Kamali, Dr. Ghader Manafiazar, Dr. Fatemeh Baghbani, Mojgan Jalali, and Dr. Sara Soleimanifar for being loyal and supportive friends in this

journey.

I would like to offer my thanks to Mechanical Engineering department staff, particularly Gail Dowler for her high discipline and enormous support during my journey.

My deepest heartfelt appreciation goes to my family specifically those in Canada, Mehdi, Maria and Saeide, for their patience, love and support. Without them, this thesis would not have been possible.

Table of Contents

List of Tables

List of Figures

Nomenclature

$\boldsymbol{\delta}_{n,ij}$	Normal overlap
$\boldsymbol{\delta}_{t,ij}$	Tangential overlap
$\boldsymbol{\omega}_i$	Angular velocity of particle i
$\boldsymbol{\tau}_f$	Fluid shear stress tensor
ΔV	Volume of the computational cell or elements
$\dot{\boldsymbol{\delta}}_{n,ij}$	Normal overlap derivatives with respect to time
$\dot{\boldsymbol{\delta}}_{t,ij}$	Tangential overlap derivatives with respect to time
$\dot{\boldsymbol{u}}$	Particle acceleration
$\dot{\boldsymbol{v}}$	Fluid acceleration
ϵ_f	Fluid void fraction in cell
$\gamma_{n,ij}$	Normal damping coefficient
$\gamma_{t,ij}$	Tangential damping coefficient

$\mathrm{Re_p}$	Particle Reynolds number
$\mathrm{Re_s}$	Reynolds number for shear flow
$\mathrm{S_{tr}}$	Strouhal number
μ_f	Fluid dynamic viscosity
ϕ	Porosity of porous media
ϕ_2	Particle sphericity
ρ_f	Density of fluid
ρ_p	Particle density
ρ_s	Sphere density
τ_v	Momentum relation time-scale
$\boldsymbol{f}_{\nabla p,i}$	Pressure gradient
$\boldsymbol{f}_{\nabla.\boldsymbol{\tau},i}$	Shear stress
$\boldsymbol{f}_{B,i}$	Basset force
$\boldsymbol{f}_{d,i}$	Drag force on particle i
$\boldsymbol{f}_{Mag,i}$	Magnus lift force of particle i
$\boldsymbol{f}_{pf,i}$	Individual force acting on the particle
$\boldsymbol{F}_{pf}$	Momentum transfer term also called momentum coupling term

$\boldsymbol{f}_{Saff,i}$ Saffman lift force on particle i

$\boldsymbol{f}_{vm,i}$ Virtual mass force on particle i

$\boldsymbol{g}$ gravity

$\boldsymbol{F}_b$ Body forces

$\boldsymbol{F}_c$ Contact force

$\boldsymbol{F}_d$ Drag force

$\boldsymbol{F}_g$ Gravity force (body forces)

$\boldsymbol{F}_n$ Normal interaction force

$\boldsymbol{F}_p$ Pressure gradient force (surface force)

$\boldsymbol{F}_s$ Forces acting on the particle surface: sum of all surface forces

$\boldsymbol{F}_t$ Tangential interaction force

$\boldsymbol{F}_\tau$ Shear stress force (surface force)

$\boldsymbol{F}_b$ Basset force (surface force)

$\boldsymbol{f}_{c,ij}$ Contact force between the particle i and particle j

$\boldsymbol{f}_{c,iw}$ Contact force between the particle i and wall w

$\boldsymbol{F}_l$ Lift force (Magnus and Saffman) (surface force)

$\boldsymbol{F}_{mg}$ Magnetic force (body forces)

$\boldsymbol{F}_{nc}$ Non-contact force on particle i due to other particles such as electrostatic, van der Walls forces or cohesive forces (such as liquid bridges)

$\boldsymbol{F}_{vm}$ Virtual mass force (an unsteady surface force)

$\boldsymbol{T}_{c,ij}$ Contact torque applied on the particle i due to the collision with particle j

$\boldsymbol{T}_{c,iw}$ Contact torque applied on the particle i due to the collision with the wall section w

$\boldsymbol{T}_{r,ij}$ Rolling friction torque applied on the particle i due to the collision with particle j

$\boldsymbol{T}_{r,iw}$ Rolling friction torque applied on the particle i due to the collision with the wall section w

$\boldsymbol{v}_i$ Instantaneous velocity of the particle i

$\boldsymbol{V}_n$ Normal velocity components of the relative sphere surface velocity at the contact point

$\boldsymbol{V}_p$ Instantaneous velocity of the particle

$\boldsymbol{V}_s$ Particle slip velocity

$\boldsymbol{V}_t$ Tangential velocity components of the relative sphere surface velocity at the contact point

A_p Projected area of the particle

C_d Drag coefficient of the particle

C_{fs} Static friction coefficient

C_{lr} Coefficient of rotational lift

C_{nrest} Normal coefficient of restitution

C_{trest} Tangential coefficient of restitution

C_{vm} Virtual mass coefficient

d_* Dimensionless particle diameter

d_n Representative of the normal losses (inelastic forces)

D_n Overlap in the normal direction at the contact point

d_p Particle diameter

D_p Particle diameter

d_t Representative of the shear losses (inelastic forces)

D_t Overlap in the tangential direction at the contact point

D_{10} Portion of particles with diameters smaller than D_{10} is 10%

D_{50} Portion of particles with diameters smaller than D_{50} is 50%

D_{90} Portion of particles with diameters smaller than D_{90} is 90%

E Young's modulus of elasticity

E_{eq} Equivalent Young's modulus

f Frequency of the flow oscillations

i Counter for the particle

I_i Moment of inertia of particle i

k Permeability of porous media

k_n Normal spring stiffness (spring constant)

k_t Tangential spring stiffness (spring constant)

$k_{n,ij}$ Normal stiffness coefficient

$k_{t,ij}$ Tangential stiffness coefficient

L Characteristic length

M_A Mass of particle A

M_B Mass of particle B

m_p Particle mass

M_{eq} Equivalent particle mass

mu_c Viscosity of continuous phase

n_p number of particles

N_{ndamp} Normal damping coefficient

p	Pressure
P_i	Inertial resistance factor
P_v	Viscous resistance factor
R_A	Radii of particle A
R_B	Radii of particle B
R_{eq}	Equivalent radius
s	Surface of a sphere having the same volume as the particle
S	Particle actual surface area
t_{DL}	Dimensionless time
u	Fluid velocity
U	Particle velocity
u_*	Dimensionless terminal velocity
v	Poisson's ratio
v_A	Poisson's ratio of particle A
V_p	Volume of the particle
V_t	Particle terminal velocity
W	Slot width

x_i Instantaneous linear displacement of the particle i

St Stokes number

Figure 0.1: Patience and Perseverance: Author's first oil painting started when the thesis writing process began and ended when the thesis was finished. The thesis and this artwork are strongly related in the author's opinion.

Chapter 1

Introduction

1.1 Motivation

During the in-situ extraction of oil from oil sands, it is a challenge to produce oil without producing sand at the same time. In steam assisted gravity drainage (SAGD), the reservoir produces an emulsion of condensed water and liquefied bitumen with a large amount of unconsolidated sand. Sands destroy the oil production equipment, such as pipes and pumps[14]. Sand control technology reduces energy costs for oil and gas industry[15]. By using sand filtration[16], with the same amount of energy, more oil will be produced[15]. The multi-particle arching phenomenon[17] also known as bridging, that occurs at filter opening, helps with sand retention[18] and is critical in sand filtration because a stable multi-particle arch supports sand filtration[19]. In this research, the conditions and parameters that support the stability of the multi-particle sand arching are explored. The conditions that may cause this arching to break[20],

as well as the reformation after breakage are investigated. The following gaps serve as motivation for this study.

Researchers have not investigated retention mechanisms specifically multi-particle arching with non-spherical particles[21]. Previous research on this subject has been mostly restricted to study of limited factors influencing the multi-particle arch formation such as particle concentration and particle velocity at the pore level[22] [23]. This study makes a contribution to exploring new parameters that affect the particle retention mechanisms, such as the role of physical forces[24] [25].

Previous studies of the bridging phenomenon have not dealt with transient conditions in the fluid flow domain. This study aims to offer an insight into the performance of the multi-particle bridge under transient conditions[26]. Majority of the studies in the field of the multi-particle bridge have only focused on multi-particle bridging phenomena in the porous media[27] and at pore-scale[28], not at the filter openings[29] [30]. This research tried to fill that gap by engaging with the bridging at the filter opening and at micro-scale[29].

Similar studies have not investigated retention mechanisms specifically multi-particle bridging having fluids with high viscosity[31]. This study aims to offer an insight into the performance of the multi-particle bridge having heavy oil as the carrier phase of the particulate flow[32].

Previous studies have not dealt with retention mechanisms specifically multi-particle bridging in a sand filter applied in horizontal wells[33]. This research tries to fill that gap by engaging with the multi-particle bridging at the filter opening of a horizontal well.

Similar studies have not investigated retention mechanisms specifically multi-particle arching by numerical simulation[34] and they have applied experimental studies[35]. This research aims to offer an insight into the performance of the multi-particle bridge through numerical simulations.

The research outcomes of this study will be a computational fluid dynamics (CFD)-discrete element method (DEM) model cable of predicting multi-particle bridge formation, stabilization, breakage and reformation under steady and transient conditions of the well-bore as well as break down of the physics involved in the multi-particle bridging phenomenon.

Applying and advancing these findings will help industry partner of the research make better decisions about filter selection and filter opening design while dealing with non-spherical sand particles at micro-scale having heavy oil and under transient flow condition in a horizontal well.

This research supports reduced sand production in oil wells and increased oil production while consuming the same amount of energy. The arching phenomenon helps with sand-retention and is critical in sand filtration because a stable sand arch supports sand filtration[36].

Project Filtration is an operation that separates solids from fluids (liquids or gases) by having a medium through which only the fluid can pass[19]. This medium is called filter. In filter, oversize solids in the fluid are retained while fluid and small particles pass through. Filtration happens in nature and engineering applications[16]. For instance, in the human body, kidney filtration removes waste from the blood, during water treatment, unwanted materials are removed by the filter medium, and in the oil industry, sand filters are used to

prevent and control sand production, and to increase the oil production while using the same amount of energy.

The filter open flow area, that is the area of filter open to flow, and mesh size or opening size of the filter are the factors considered when selecting a filter. Solid particle buildup and plugging[35] [37] at the entrance and throughout the length of the filter opening are the common failure[38] mechanisms in filters. Plugging is the reduction in the open flow area of the filter, mainly due to trapped solid particles. Plugging is an issue because it decreases the efficiency of filter. Particle buildup[39], another undesirable phenomenon, also happens due to the transport of very small particles in the system.

In some cases, solid particles can form bridges (arches) on the filter opening, which is known as bridging (arching) phenomenon. This bridging could be a hydrodynamic[40] phenomenon that happens due to flow convergence[41], or mechanical[42] due to the high concentration of the particles at the opening. The bridging phenomenon is important because it plays a key role in preventing plugging and stops the solid particles from passing through the filter. Investigation of the physics of the bridging phenomenon and the factors which might affect its stability or failure, such as force distribution (interaction forces, drag, buoyancy, pressure gradient, gravity, etc), particle shape and size, particle concentration, fluid properties (such as non-Newtonian viscosity[42]), and the geometry of the opening can help to improve the criteria for filter selection.

Objectives The objectives of this research are as follows: analyze the physics of the bridging phenomenon at the filter opening, and investigate the sand arching stability[22] or failure. The key is to understand and analyze

the science behind the scenes of the arching phenomenon and break down the physics of this phenomenon. This will be accomplished by investigating the factors and conditions affecting arching[24] [43].

Methodology This problem is explored by numerical modeling[44]: the computational fluid dynamic (CFD) to model the fluid flow behavior, and the discrete element method (DEM) to model particle flow. This coupling is done in STAR-CCM+ (SIEMENS PLM)[5]. Validation of the developed simulations is conducted through benchmarking by experiments[45] and/or possible theoretical/analytical solution.

Data The information related to the type and size of the filter are provided by the industrial partner of this research, RGL Reservoir Management Inc. Considering the interest of the RGL and the need of Alberta local industry[46], the priority of the research is given to filters used in steam-assisted gravity drainage (SAGD)[31]. The rest of the data, including particle size distribution (PSD)[47] are accessible through collaborating labs at the University of Alberta[48].

In this research, the conditions and parameters that support the stability of the sand arching are explored. The conditions that may cause it to break, as well as the reformation after breakage are also investigated.

The primary motivation of this research was to explore physics of the sand bridging phenomenon on the filter opening and to develop a model that helps to quantify the enhanced range for the opening size of a filter, and to answer this question: which filter opening size allows for minimum particles passing the filter where there is not only plugging but also minimum sand

particles production. This research could support selecting suitable screen design (aperture size) to have a stable sand arch which results in more oil production consuming the same amount of energy. Findings might be applied to other types of filters, for instance, the filters used in the pharmaceutical industry.

1.2 Particulate Flow in Sand Filters

Particulate flow, or particle-laden flow through sand screens is of special interest to the oil and gas industry for sand control purposes[49]. The selection of sand screens for specific applications has primarily been based on experimental data, rules of thumb and/or some correlations[17]. The experimental results on sand retention mechanisms are strongly dependent on how the tests are conducted and interpreted which could result in various recommendations for screen type and the opening size of the sand screen. Simulations could provide a better understanding of the problem physics and overcome some of the experimental limitations.

Simulation of the bridging phenomenon and the factors affect bridging stability and destabilization will be helpful to enhance the criteria for the sand screen selection and design[18],[50],[51]. All these phenomena: plugging, particle build up and bridging can be explored further through simulation of the particulate flow around and through the sand screen device.

Two popular types of sand screens widely used in the oil industry are: slotted liners[52] and wire-wrapped screens (WWS)[36], both with rectangular

screen openings, Figure 1.1. The sand screen acts as an obstacle to prevent the solid particles from flowing into the well. Sand-retention mechanisms, such as particle size-exclusion and bridging phenomena help this prevention. In Figure 1.2, schematics of the two types of multi-particle bridge are presented.

Figure 1.1: Slotted liner and wire-wrapped screen widely used in Alberta SAGD wells (used from rglinc.com with permission)

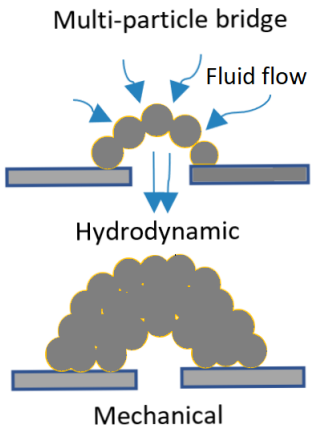

Figure 1.2: Slotted liner, wire-wrapped screen and bridge formation on an opening

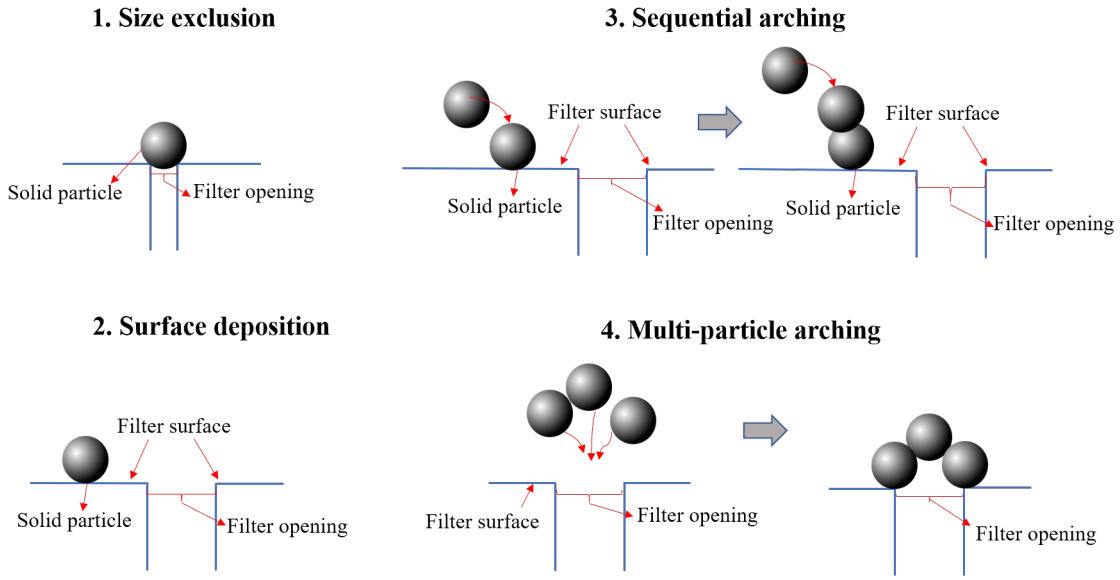

Figure 1.3: Schematic illustrating the four main particle retention mechanisms at the filter opening.

Figure 1.3 presents the main particles retention mechanisms at a granular scale while having particles larger than 100 μm[19]:

1. Size exclusion mechanism that happens due to large particle size in comparison with the constriction. It is also known as straining.

2. Surface deposition mechanism occurs due to forces existing between the particles and the wall. The roughness[53] of the wall could cause surface deposition mechanism as well.

3. The sequential bridging mechanism that happens following surface deposition.

4. Multi-particle bridging mechanisms could happen due to the high concentration of particles (mechanical bridging) or because of flow convergence

at constriction called hydrodynamic bridging. See Figure 1.2.

Figure 1.4 illustrates how a standalone WWS in open-hole completion[39] works. Sand particles are produced at various concentrations depending on how the formation (1) collapses. The screen (2) acts as an obstacle to prevent the particles from flowing into the well. This prevention is successful with the aid of sand-retention (3) due to size-exclusion and multi-particle bridging mechanisms[8].

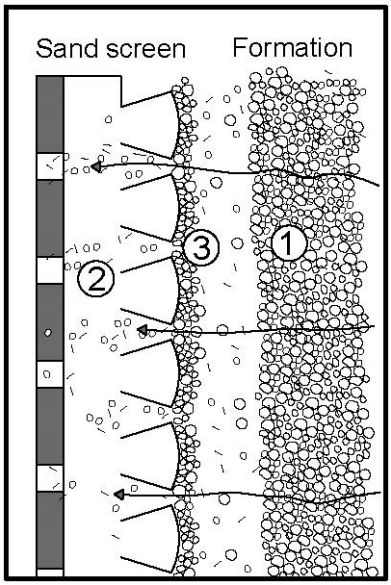

Figure 1.4: Standalone WWS in an open-hole completion of a vertical well, the collapse of sand particles make bridges at the WWS opening (GEKEngineering.com), adapted from King[8].

There are various factors involved in the investigation of the bridging and plugging. Examples of these factors are the physical forces such as the interaction forces[54], drag force[55] and gravity, particles' velocity, particles' concentration, particle geometry, fluid velocity, fluid properties[56], slot geome-

try[15], particle properties as well as particle's size and shape.

The rest of this chapter includes a review of available literature on plugging and bridging. There is also a section devoted to an overview of methods to model the particulate flow and an overview of discrete element method theory. Bridging and arching will be used alternatively in this thesis.

1.3 Plugging and Bridging Phenomena

1.3.1 Plugging

Solid particle plugging[35],[37] at the entrance and throughout the length of the filter opening are the common failure mechanisms in filters. Plugging is the reduction in the filter open flow area, mainly due to trapped solid particles and is an issue because it decreases the filter efficiency. To investigate plugging, the retention mechanisms: size exclusion mechanism, surface deposition mechanism, sequential bridging mechanism, and multi-particle bridging mechanism must be well-understood.

Particle retention mechanisms have been experimentally studied by several researchers. Tran et al.[57] experimentally studied the plugging of well perforations and pore throats in porous formation. They developed empirical correlations for the effect of pore throat to particle size ratio on flowing fluid conditions and plugging time that could lead to particle build up. They correlated the critical pore throat to particle size ratio, the particle volume fraction and the Reynolds number.

Agbangla et al.[58] studied pore fouling and plugging dynamics experimen-

tally at the pore level in microchannels. Using spherical particles, they found a critical particle flux density for plugging. Their experimental results helped to identify two-pore plugging mechanisms: deposition and particle bridging at pores. They claimed that the plugging is controlled by the particle interactions, the effect of hydrodynamics, particle concentration, flow rate, and surface interactions. Their experiments showed that plugging is the result of the collective behaviors of particles at the channel entrance.

Guariguarta et al.[59] measured the jamming (plugging) probability of suspended 2D disks experimentally in an open channel with a restriction and for a dense particle system. In their experiment, they did not observe the intermediate state of suspension, and particles went directly from a flowing state to a jammed state (plugged state). The probability of jamming was found to be dependent on the ratio of channel opening to particle size.

Dai and Grace[60] performed experiments to measure a multi-particle hydrodynamic "blockage (plugging) index" along with a horizontal rectangular channel leading to constrictions. The constrictions had different geometries: circular and rectangular. They used different shapes for particles such as cuboids, cylinders, cones, and spheres. Experimental results revealed that small constriction size, high particle concentration, and high particle compressibility will increase the probability of blockage (plugging).

Wyss et al.[30] have also studied experimentally the plugging of microchannels. They observed that plugging happens after a critical number of particles flow through the outlet regardless of the flow rate or the particle concentration. In their case, particles did not have a chance to arrive at the

pore simultaneously.

Sharma et al.[19] showed experimentally that the plugging of a sandstone core was a function of the in-situ concentration particles in the pore space.

1.3.2 Bridging (Arching)

In some cases, solid particles could make bridges (arches) on the filter opening, which is known as the bridging phenomenon.

Bianco et al.[61] experimentally investigated the morphology and stability of sand bridges in two-phase saturated sand samples subjected to a water influx. They analyzed the changes in fluid flow velocity and water saturation and the distributions of porosity and water saturation in the arched region. They investigated the effect of wetting-phase saturation on the stability of the bridge at the pores. The results of that study showed that single-phase saturated sand did not develop enough cohesive strength to support a stable arch. However, a small increase in wetting-phase saturation developed enough cohesive strength to stabilize an arch reducing sand production.

Valdes et al.[29] showed by experiments in a tube with a circular orifice that the bridging chance will increase by increasing particle size and particle volume fraction. They connected the stable bridge with particle size and pressure drop in the tube.

Ramachandran et al.[62] experimentally investigated particulate flow through cylindrical pores. They described the effects of velocity, particle concentration, and the ratio of pore size to a particle size on retention mechanism by hydrodynamic bridging in the pores. They reported a critical flow velocity

necessary for particle bridging to occur. This critical velocity is a measure of the net colloidal inter-particle and particle–porous medium repulsion that must be overcome by the hydrodynamic forces for bridging to occur.

Valdes et al.[22] experimentally investigated the migration of the mobile particles through porous networks. Experimental results showed that bridge formation and its stability were controlled by particle shape, relative pore throat-to-particle size, and skeletal forces between particles forming the bridge.

Feng et al.[23] and Wu et al[44] presented the combined experimental and numerical modeling study to investigate the sand screen device performance. They have developed a new sand-retention test apparatus and a computational fluid dynamic (CFD)-discrete element method (DEM) model for numerical studies. The parametric study using the DEM-CFD model has demonstrated the strong effect of liquid phase velocity, solid volume ratio and slot size on the amount of the sand produced. They did not investigate the bridging phenomenon.

Han et al.[63] used the lattice Boltzmann method (LBM)-DEM coupling to simulate the sand bridge in the pore space. The collapse and reconstruction of sand bridges in the perforation cavity were also investigated. The LBM-DEM model could simulate the collapse and reconstruction of the sand arch in the perforation cavity.

Polillo et al.[64] simulated the sand production mechanics in an open vertical well using a finite element method. The initial stress field around the well-bore and the mechanical rock properties were taken from previous sand arching experiments. The effect of variations of cohesion and pressure drop across the

well was observed. They concluded that the stability of the sand around the well-bore depends on the pressure drop across the sand face and the cohesion of the sand grains. They did not investigate the plugging and bridging phenomena.

Few experiments have studied multi-particle hydrodynamic bridging at the pore-level[40],[22]. Hydrodynamic multi-particle bridging in neutral systems such as granular matter is controversially the least understood of all the retention mechanisms[42]. Additionally, considerable research on plugging and bridging has been done experimentally in porous regions and with the focus on the monodispersed particle size[65],[66]. Few studies have focused on the simplified polydispersity such as tri-disperse and bi-disperse particle size distribution. Instead, they used the average particle diameter obtained by the number of particles (number-average) or volume of particles (volume-averaged) to study plugging[67],[68],[69]. Some of the research on bridging and screen selection criteria in the literature are also based on a couple of points of the PSD, for instance, D_{10} and D_{50}[50],[70]. Valdes et al.[29] showed that at low concentration of the particles, sand bridging was negligible, and the retention mechanisms were exclusion and surface deposition. Accordingly, they claimed that the bridging should happen at intermediate and high particle concentration of the particles, which is applicable to the SAGD case.

Mondal et al.[34] showed through CFD-DEM simulation that if no frictional force existed between the sand grains, there was no bridging. They investigated the effect of the shear forces on the bridge formation. Their investigations also confirmed that the ratio of the particle to the sand screen opening size was the most critical factor in the number of particles produced.

Guo et al.[71] studied the effect of the stress in a large-scale unconsolidated sand pack over a multi-slot coupon of the slotted liner. The experimental results showed that the slotted liner performance is significantly affected by the stress of the packed-bed on the liner. They concluded that the higher stresses help stabilize the sand bridges over the slots which result in less sand production.

Wang et al.[72] investigated the effect of anisotropic stress buildup around slotted liners having multiphase flow. Brine, oil, and gas were used as fluids. Lateral and axial stresses were applied to the liner to simulate the stress conditions around the slotted liner. Experimental results showed the importance of the stress around the liner on its performance. With increased stress on the slotted liner, less sands were produced.

Fattahpour et al.[73] also studied the effect of the increasing stress on the performance of the sand filter. They applied varying levels of stress to the sand-packs around the slotted liner in parallel and perpendicular to the multi-slot coupon. With increased stress, they reported a reduced amount of the sand production.

1.4 Research Gaps

The research on the bridging phenomenon is applicable and helpful to various filtration industries. Considering the need of the industry partner of this research, the concentration of the work is on the sand filters applied in oil wells with the focus on the production well in SAGD[36].

Sand control in SAGD wells[33] works satisfactory when the flow is steady. However, it comes to an issue as soon as there are time-dependent flow phenomena that could cause reverse flow[74] at the filter opening or instability in the bridging. Water hammer[75] and vibrational flow are examples of transient well-bore phenomena happening in the SAGD production well that affect bridge stability. These transient well-bore events can be mathematically simulated through time-dependent boundary conditions of the flow domain[75].

There are gaps in the field of bridging phenomenon that will be covered through this project. Previous studies of the bridging phenomenon have not dealt with transient conditions in the fluid flow domain. This study aims to offer an insight into the performance of the bridge under transient conditions. The findings will help with the decision making on filter selection and the design. Also, researchers have not investigated multi-particle bridging with non-spherical particles at micro-scale. This study will make a major contribution to explore parameters that affect the bridge formation, stabilization, destruction and reformation of the arch after breakage.

Additionally, previous research on this subject has been mostly restricted to study of limited factors influencing the bridge formation such as particle concentration and particle velocity at pore level[22],[23]. This project aims to provide an opportunity to advance the understanding of bridging phenomenon. Finally, most of the studies in the field of the multi-particle bridge have only focused on bridging phenomenon in the porous media, not at the filter/screen openings[29],[30]. This research will engage with the bridging at the filter opening.

The research outcome will be a CFD-DEM model capable of predicting bridge breakage and reformation under transient conditions of the well-bore.

1.5 Particulate Fluid Flow Modeling

There are two main methods to model particulate flow behavior: Eulerian-Eulerian and Eulerian-Lagrangian. The fluid phase in both approaches is considered as a continuous phase, and in the governing equations locally averaged variables are used[32]. Eulerian perspective considers the solid phase as a continuous phase and equations are derived based on a fluid characteristic. This approach requires empirical equations to model the behaviour of the dispersed phase.

The other approach, called a Lagrangian perspective, such as DEM. The Lagrangian approach considers every single particle and by applying Newton's laws of motion, the equations of motions of the particles are derived based on the mass and velocity.

In DEM, the motion of each particle is analyzed incorporating the fluid dynamic forces, the contact forces, and the moments due to the neighboring particles. Solid phase in the particulate fluid can also be simulated on a discrete scale or the continuum scale. Discrete element method can model the discrete nature of the granular substance.

The two-fluid model (TFM) is a continuum approach where both the fluid and the solid phase are treated as continuum media described by macroscopic conservation equations. Among these, the TFM, coupled direct numerical sim-

ulation (DNS)-DEM and coupled CFD-DEM are the most popular approaches for particulate fluid flow simulation[76].

The CFD-DEM approach is the most attractive one for simulating particulate fluid flow at the particle scale. Some of CFD-DEM advantages over other approaches[77] are less computational cost in comparison with LB-DEM and DNS-DEM and the possibility of capturing the particle-particle interactions compared to TFM. The details of the advantages and disadvantages of these different models have been discussed in Zhu et al.[78].

DEM was originally proposed by Cundal et al[79] in 1979. DEM simulations are important as they are capable of tracking the trajectory of the particles dynamically, considering various forces acting on individual particles. These features are not easily accessible from experimental techniques. Process of tracking particles is often slow, and costly to achieve using experiments. Fundamental laws of Newtonian mechanics govern the interaction between discrete particles in DEM[79]. Researchers have used DEM to study particle packing, hopper flow, mixing and granulation which are all particulate flow over the past two decades[80]. Zhu et al[81] published a comprehensive review of the theoretical developments on DEM and its applications. The governing equations in DEM for describing translational and rotational motions of individual solid particles are Newton's laws of motion. It relies on the motion of each particle individually as well as particles' interactions.

Coupled CFD-DEM, the approach that is applied in this research, was employed firstly by Tsuji et al.[82] and has gained popularity rapidly due to advances in computational power. The advantage of CFD-DEM is that it

is applicable for various sizes of particles and geometries[83]. Considering the relative size between the particles and the numerical grid, there are two CFD-DEM methods: unresolved and resolved CFD-DEM approaches. The unresolved method is applicable for small particles relative to the grid used for the flow. In this approach, DEM is applied to calculate particle motion without resolving the detailed flow around each particle. Resolved methods are suitable for larger particles relative to the numerical grid and also for dealing with complicated geometries where small grids are necessary to increase the accuracy.

Sand filtration operation is a multiphase flow process of a granular-fluid system where CFD-DEM is a promising approach to apply[78]. To simulate plugging and particles migration in sand screen device, a fully coupled DEM-CFD model is applied. The concentration of the particles in the particulate flow is an important factor in the selection of the methodology.

In a solid-fluid flow dominated by solid particles, due to the high concentration of the particles, DEM alone could be used for simulation. In high concentration of the particles, the hydraulic bridge will be destroyed, and the mechanical bridge will be constructed. The stable hydraulic bridge is expected to be seen in the medium concentrations[34], which is the case that will be studied here. Chapter 2 has a detailed description of the CFD-DEM approach.

1.5.1 DEM Theory

Discrete element method is a modelling methodology focused on particulate systems simulations. It considers a group of computational points and each

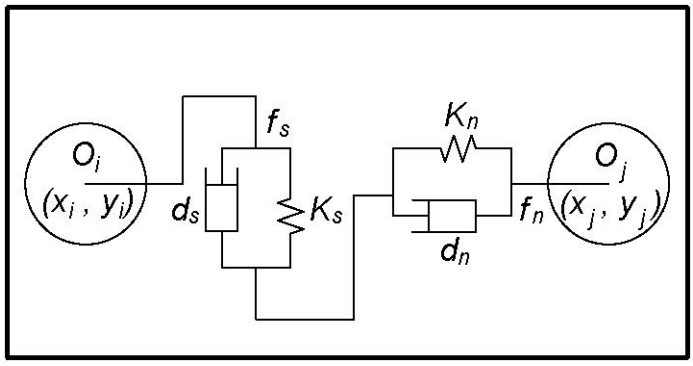

Figure 1.5: Springs and dashpots between two particles (O_i and O_j) to model normal and tangential contact forces in particle collision, adapted from Kawamura[9].

point is associated with a physical particle. The behavior of the particle is assumed to be governed by the particle body force, surface force and contact force[9].

The relationship between the two particles is investigated by introducing two types of interaction forces: inelastic interaction force and elastic interaction force[9]. In the DEM approach, the contact force acting on a solid particle is calculated using a spring-dashpot system. Dashpots and springs are installed between the two particles to represent the inelastic collision between the two particles and the elastic interaction respectively (see Figure 1.5). In Figure 1.5, K_s and K_n are spring constants and representatives of the elastic forces. d_s and d_n are the representative of the shear and normal losses (inelastic forces) in the collision.

DEM equations rely on the motion of each particle individually as well as particles' interactions. In a Lagrangian frame, the information about each particle within the computational domain including mass, velocity, force, angular

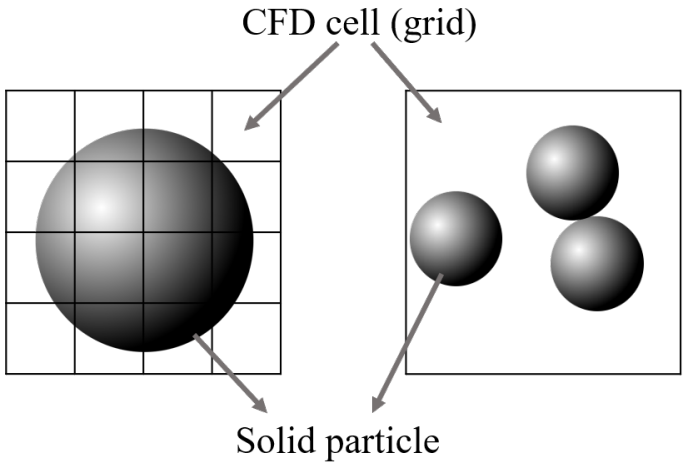

Figure 1.6: Particle size versus computational grid size: a) Resolved CFD-DEM or smoothed unresolved CFD-DEM b) Unresolved CFD-DEM.

momentum is individually trackable.

Over the past two decades, DEM has been used to study solid particle flow such as particle packing, hopper flow, mixing and granulation[80]. CFD is applied to analyze the fluid flow and Navier-Stokes equations describe the flow behavior. The advantage of CFD-DEM is that it is applicable for various sizes of the particle and geometries[83]. Considering the size of the particle and the flow geometry, there are two distinct CFD-DEM methods: unresolved and resolved approaches (see Figure 1.6). The unresolved method is applicable for small particles relative to the flow geometry. Resolved methods are suitable for larger particles relative to the flow geometry also dealing with complicated geometries where small grids are necessary to increase the accuracy[77]. Detailed information on coupling CFD-DEM could be found in Kloss et al[77].

DEM calculations are computationally expensive and require integration

on small time-steps to resolve surface contacts between the particles[78]. DEM practical CPU time limits are reported to be less than few million particles and less than one minute of physical time[5]. There is no mesh required for DEM since each particle is a computational point by itself.

Coupled CFD-DEM is a promising approach to explore particulate flow in sand screen device and helpful to investigate the interaction forces between the particles and particle-fluid. This research aims to apply analytical models and numerical simulations to investigate the solid flow and fluid flow in filter opening and to explore the bridging phenomenon[84]. The CFD-DEM model will be validated with the results of the benchmark problems and the experimental work in the collaborating labs.

1.6 Research Phases

1.6.1 CFD-DEM Setup, Validation and Mesh Investigation

The CFD-DEM model is being setup and validated using problems with known analytical and experimental results. Another approach is comparing the results obtained in Computational Fluid Dynamic Lab with the results of the experimental studies in the collaborating labs such as Optical Diagnostics Group[1],[41],[56] and RGL Reservoir Management Inc. labs. Chapter three of this thesis is devoted to the CFD-DEM model setup, verification and validation. Mesh sensitivity study is also conducted to find the coupling resolution between

the CFD and DEM.

1.6.2 Bridging Simulation and Observation

Following the validation of the CFD-DEM model, the first step would be simulation and observation of the bridging phenomenon on a single slot (with a fixed width). There are various factors involved in bridge formation such as particle properties, particle concentration, particle size and shape, fluid properties (viscosity and density), interaction forces forces between fluid and particle, and interaction forces between particles. Chapter 4 of this thesis is devoted to testing various conditions to get the arch. This phase is started with the low-concentration of particulate flow (slurry flow) and is continued on high concentration of the particles (packed-bed). Finally the arch behavior is studied under transient condition of the flow domain.

1.6.3 Investigating the Physics of Bridging

When the bridge is successfully formed, analyzing the physics behind the stable bridge formation, stabilization, destruction and reformation is the next phase of this study. Part of this investigation is on learning the roles of the various forces involved in the formation of the bridge. In the bridging phenomenon, multiple variables are involved. The parametric study is applied following the observation of the bridging to study of the parameters playing roles in bridge formation including the breakdown of the forces involved and to determine the most important parameters on arch formation. Testing time-dependent

boundary conditions and simulation of the common well-bore phenomena, it is expected that the stable sand bridges respond differently to different time-dependent boundary conditions of the flow domain. The response means how stable is the bridge under sudden pressure and velocity changes of the fluid in the well-bore? How is the bridge breakage and reformation after a sudden change in the pressure and velocity of the fluid in the well-bore? These time-dependent conditions (such as the periodic pressure change in the outlet) could be equivalent to the realistic phenomenon in the well-bore, such as vibrational flow.

1.7 Summary

Finally, this part of chapter 1 gives a summary on the knowledge gaps, and accordingly, research phases proposed to investigate the stabilization, destabilization, formation, destruction and reformation of the multi-particle bridge under various conditions. Here are some gaps in this field of study:

1. Previous studies of the bridging phenomenon have not dealt with transient conditions in the fluid flow domain. This study aims to offer an insight into the performance of the bridge under transient conditions. The findings will help with the decision making on filter selection and the design.

2. Researchers have not investigated multi-particle bridging with non-spherical particles at microscale. This study will make a major contribution to

explore parameters that affect the bridge formation, stabilization, destruction and reformation of the arch after breakage.

3. Previous research on this subject has been mostly restricted to study of limited factors influencing the bridge formation such as particle concentration and particle velocity at pore level[22],[23]. This project aims to provide an opportunity to advance the understanding of bridging phenomenon considering more parameters affecting it.

4. Finally, most of the studies in the field of the multi-particle bridge have only focused on bridging phenomenon in the porous media, not at the filter/screen openings[29],[30]. This research will engage with the bridging at the filter opening.

This project will provide a unique opportunity to advance the understanding of multi-particle bridge formation under various conditions. First phase of this work is setting up a CFD-DEM model as well as verification and validation process. Following the verification and validation of the CFD-DEM model, three more phases will be followed:

1. Bridge observation on the validated CFD-DEM setup.

2. Analyze the physics involved in multi-particle bridging phenomena.

3. Investigation of the bridge response under common wellbore phenomena.

Next chapters are organized accordingly. Chapter 2 is the methodology. Chapter 3 is about CFD-DEM model development, verification and Validation.

Chapter 4 is the investigation of multi-particle arch formation under various conditions and chapter 5 is the discussion and future Work.

Chapter 2

Methodology

This chapter is an overview of the particulate flow modeling approach applied in this research work. It emphasizes on the details of the mathematical and computational models behind the computational fluid dynamics-discrete element method (CFD-DEM) technique. The framework to apply the CFD-DEM to solve the problems in the current research will be also discussed.

2.1 Particulate Flow Modeling Techniques

As discussed in chapter 1, there are two main approaches to model particulate flow behaviour: Eulerian-Eulerian and Eulerian-Lagrangian [6]. The Eulerian-Lagrangian approach will be used in this study to allow the tracking of individual particles.

Among the Lagrangian models, the CFD-DEM approach is the most attractive for this study. Some of the advantages of CFD-DEM over other

approaches[77] are less computational cost in comparison with DNS-DEM and the possibility of capturing the particle-particle interactions compared to TFM. Another advantage of CFD-DEM is its application for various sizes of particles and geometries[83]. The details of the advantages and disadvantages of these different approaches have been discussed in Zhu et al.[78]. Zhu et al.[81] published a comprehensive review of the theoretical developments on DEM and its applications.

DEM simulations are capable of tracking the trajectory of the particles dynamically, considering various forces acting on the individual particles. This feature is not easily accessible by experimental techniques. Simulations are properly suited to study the effect of various parameters and develop correlations for general use, in comparison with experiments[6].

The remaining part of this chapter proceeds as follows; an overview of the DEM theory will be discussed in section 2. Mathematical model of particulate flow will be presented in detail in section 3. In section 4, the data transfer between the two phases, solid-fluid coupling, is discussed. In section 5, discretization scheme and numerical solution method will be reviewed briefly. Finally, the conclusion gives a brief summary.

2.2 Overview of the DEM Theory

Discrete element method (DEM) model is a Lagrangian modeling methodology applies to model dense particle flow[79]. The governing equations in DEM for describing translational and rotational motions of individual solid particles

are Newton's laws of motion. Both forms of Newton's second law of motion, linear momentum equation and angular momentum equation, are applied as the governing equations. DEM relies on the motion of each particle individually as well as particles' interactions and considers a group of computational points where each point is associated with a physical particle. The behaviour of the particle is governed by the particle body force, surface force and contact force[9]. Particles are modeled as the rigid body having two types of motions: translation and rotation. The relationship between the two particles is investigated by introducing two types of interaction forces: inelastic interaction force and elastic interaction force[9]. In the DEM approach, the contact force acting on a solid particle is calculated using a spring-dashpot system. Dashpots and springs are installed between the two particles to represent the inelastic collision between the two particles and the elastic interaction respectively. Energy is dissipated to heat and sound during an inelastic collisions between particles. The distinct characteristic of the DEM is that the inter-particle contact forces are included in the equations of motion. These forces cannot be ignored for flows including many interacting particles. A DEM calculation is computationally expensive, since it requires integration on small timesteps to resolve surface contacts between particles. Using an unresolved CFD-DEM coupling approach, as it will be the case in this study, there is no mesh required for DEM as it is required for CFD and each particle is a computational point[85]. The DEM particles can have various shapes and volumes[6].

STAR-CCM+ from Siemens PLM is the commercial software that is mainly used in this research work. Classical mechanics is used in STAR-CCM+

to model DEM, that is coupled with CFD through unresolved approach in STAR-CCM+, and it is based on soft-particle formulation, where particles can develop an overlap, but they do not deform[6]. The overlap during the collision is decomposed into normal and tangential directions and introduced into contact models[86]. STAR-CCM+ provides three contact models to calculate the contact force in DEM: Hertz Mindlin, Linear Spring and Walton Braun[6]. The Hertz Mindlin model has been applied in the majority of this research work.

2.3 Mathematical Model of Particulate Flow: Governing Conservation Equations

In this section, fluid flow conservation equations, solid flow conservation equations and coupling approaches are discussed.

2.3.1 Fluid Flow Conservation Equations

To simulate fluid flow, the conservation equations for mass (continuity equation) and momentum (Navier-Stokes equations (NS)) are solved. In the case of particulate flow, the CFD cells (fluid mesh) are not fully occupied by fluid. NS considers that the volume occupied by the fluid in each cell is dependent on the volume of the solid particles in that cell. Consider cell A where there is no particle which means the fluid void fraction (ϵ_f) is 1. Cell B is occupied by solid particles for 50% which means void fraction is 0.5. Fluid that flows from cell A to cell B must accelerate to ensure that the mass is conserved through

the continuity equation. The continuity equation is written as:

$$\frac{\partial}{\partial t}(\epsilon_f) + \nabla \cdot (\epsilon_f \boldsymbol{u}) = 0 \tag{2.1}$$

where ϵ_f is the fluid void fraction and $\boldsymbol{u}$ is the fluid velocity.

Comparing equation (2.1) to the incompressible continuity equation $\nabla \cdot \boldsymbol{u} = 0$, the presence of a time-dependent and space-dependent void fraction results in the non-divergence free velocity field to ensure the mass conservation. It means that the divergence of the velocity is not zero. The momentum equation is written as:

$$\rho_f \left(\frac{\partial}{\partial t}(\epsilon_f \boldsymbol{u}) + \nabla \cdot (\epsilon_f \boldsymbol{u} \otimes \boldsymbol{u}) \right) = -\nabla p + \nabla \cdot (\boldsymbol{\tau}_f) - \boldsymbol{F}_{pf} + \rho_f \epsilon_f \boldsymbol{g} \tag{2.2}$$

$$\boldsymbol{F}_{pf} = \frac{1}{\Delta V} \sum_{i}^{n_p} \boldsymbol{f}_{pf,i} \tag{2.3}$$

where:

$$\boldsymbol{f}_{pf,i} = \boldsymbol{f}_{d,i} + \boldsymbol{f}_{\nabla p,i} + \boldsymbol{f}_{\nabla . \boldsymbol{\tau},i} + \boldsymbol{f}_{vm,i} + \boldsymbol{f}_{B,i} + \boldsymbol{f}_{Saff,i} + \boldsymbol{f}_{Mag,i} \tag{2.4}$$

p is pressure, $\boldsymbol{\tau}_f$ is fluid shear stress tensor, ρ_f is fluid density and $\boldsymbol{g}$ is gravity. $\boldsymbol{F}_{pf}$, as a force, is the momentum transfer term also called momentum coupling term. n_p is the number of particles and $\boldsymbol{f}_{pf,i}$ is the individual force acting on the particle i in the presence of the surrounding fluid including drag $\boldsymbol{f}_{d,i}$, pressure gradient $\boldsymbol{f}_{\nabla p,i}$, shear stress $\boldsymbol{f}_{\nabla . \boldsymbol{\tau},i}$, virtual mass $\boldsymbol{f}_{vm,i}$, Basset $\boldsymbol{f}_{B,i}$, Saffman lift

force $\boldsymbol{f}_{Saff,i}$ and Magnus lift force $\boldsymbol{f}_{Mag,i}$ of particle i. ΔV in equation (2.3) is the volume of the computational cell or elements. $\otimes$ is the tensor product of two vectors. This form of the momentum equation is generic and is applicable to any concentration of particles and any Reynolds number in non-turbulent flow regime[86].

2.3.2 Solid Flow Conservation Equations[5]

DEM equations track the position and velocity of each particle and accounts for the interactions between the particles. The particles are allowed to have overlaps. The overlap must be less than 5% of the particle diameter and is decomposed into normal and tangential directions in contact models. Contact models simulate the contact forces in solid-solid collisions and accounts for elastic and inelastic (dissipative) collisions.

The conservation equation of linear momentum for a particle of mass m_p is written as equation (2.6) in the Lagrangian framework. The change in momentum is balanced by surface and body forces that act on the particle.

$$\frac{dx_i}{dt} = \boldsymbol{v}_i \tag{2.5}$$

$$m_p \frac{d\boldsymbol{v}_i}{dt} = \boldsymbol{F}_s + \boldsymbol{F}_b \tag{2.6}$$

$$\boldsymbol{F}_s = \boldsymbol{F}_d + \boldsymbol{F}_p + \boldsymbol{F}_{vm} + \boldsymbol{F}_l + \boldsymbol{F}_b + \boldsymbol{F}_\tau \tag{2.7}$$

$$\boldsymbol{F}_b = \boldsymbol{F}_g + \boldsymbol{F}_{mg} + \boldsymbol{F}_c + \boldsymbol{F}_{nc} \tag{2.8}$$

x_i is the instantaneous linear displacement of the particle i, $\boldsymbol{v}_i$ is the instanta-

neous velocity of the particle i, $\boldsymbol{F}_s$ is the forces acting on the particle surface and $\boldsymbol{F}_b$ represents the body forces.

$\boldsymbol{F}_d$ is the drag force that is a particle-fluid interaction force. $\boldsymbol{F}_p$ is the pressure gradient force also a particle-fluid interaction force. $\boldsymbol{F}_{vm}$ is the virtual mass force that is an unsteady force. $\boldsymbol{F}_l$ is the lift force (Magnus and Saffman), $\boldsymbol{F}_b$ is the Basset force and $\boldsymbol{F}_\tau$ is the shear stress force. $\boldsymbol{F}_d$, $\boldsymbol{F}_p$, $\boldsymbol{F}_{vm}$, $\boldsymbol{F}_l$, $\boldsymbol{F}_b$ and $\boldsymbol{F}_\tau$ are all surface forces. The momentum transfer from the continuous phase to the particle is represented by these surface forces $\boldsymbol{F}_s$ in the coupling process. $\boldsymbol{F}_g$ is the gravity force and $\boldsymbol{F}_{mg}$ is the magnetic force, both are body forces.

DEM modeling introduces extra body force $\boldsymbol{F}_c$ representing inter-particle interaction due to particle contacts with other particles and domain boundaries. $\boldsymbol{F}_c$ is called the contact force. The contact force that represents inter-particle and particle-boundary interaction is calculated for each particle considering the contacts that particle i has. This force is exerted at the contact point between the two particles or the particle and the boundary.

$$\boldsymbol{F}_c = \sum_j \boldsymbol{f}_{c,ij} + \sum_w \boldsymbol{f}_{c,iw} \tag{2.9}$$

$\boldsymbol{f}_{c,ij}$ is the contact force between the particle i and particle j. $\boldsymbol{f}_{c,iw}$ is the contact force between the particle i and wall w. The contact forces between the two particles or particle and wall are divided into elastic and dissipative forces that

have normal and tangential components.

$$\boldsymbol{f}_{c,ij} = k_{n,ij}||\boldsymbol{\delta}_{n,ij}||^a\boldsymbol{\delta}_{n,ij} + \gamma_{n,ij}||\boldsymbol{\delta}_{n,ij}||^b\dot{\boldsymbol{\delta}}_{n,ij} + k_{t,ij}||\boldsymbol{\delta}_{t,ij}||^c\boldsymbol{\delta}_{t,ij} + \gamma_{t,ij}||\boldsymbol{\delta}_{t,ij}||^d\dot{\boldsymbol{\delta}}_{t,ij} \tag{2.10}$$

$k_{n,ij}$ and $k_{t,ij}$ are the normal and tangential stiffness coefficients. $\gamma_{n,ij}$ and $\gamma_{t,ij}$ are the normal and tangential damping coefficients. k and γ are related to the material properties. $\boldsymbol{\delta}_{n,ij}$ and $\boldsymbol{\delta}_{t,ij}$ are the normal and tangential overlaps. $\dot{\boldsymbol{\delta}}_{n,ij}$ and $\dot{\boldsymbol{\delta}}_{t,ij}$ are the normal and tangential overlaps derivatives with respect to time. The expressions to define the k and γ and $\boldsymbol{\delta}$ and the a, b, c, d are dependent on the contact model. For linear contact models, a, b, c, d values are zero[86].

$\boldsymbol{F}_{nc}$ is the non-contact force on particle i due to other particles such as electro-static, van der Walls forces or cohesive forces (such as liquid bridges).

Particles angular momentum must also be conserved. The conservation equation of angular momentum for a particle is written as equation (2.11) in the Lagrangian framework.

$$I_i\frac{d\boldsymbol{\omega}_i}{dt} = \sum_j(\boldsymbol{T}_{c,ij} + \boldsymbol{T}_{r,ij}) + \sum_w(\boldsymbol{T}_{c,iw} + \boldsymbol{T}_{r,iw}) \tag{2.11}$$

I_i is the moment of inertia of particle i and $\boldsymbol{\omega}_i$ is the angular velocity of particle i. $\boldsymbol{T}_{c,ij}$ and $\boldsymbol{T}_{r,ij}$ are contact torque and rolling friction torque applied on the particle i due to the collision with particle j. $\boldsymbol{T}_{c,iw}$ and $\boldsymbol{T}_{r,iw}$ are the contact torque and rolling friction torque applied on the particle i due to the collision with the wall section w.

Hertz-Mindlin Contact Model

DEM can handle the situations when particles are densely packed and there are frequent collisions between the particles. Contact models are applied to simulate the contact force. Hertz-Mindlin no-slip contact model is a non-linear spring-dashpot contact model based on the Hertz-Mindlin contact theory [7] that is applied in this study to model the interactions between the particles and particles and domain walls.

For particle-particle collisions, the normal and tangential contact forces in the non-linear Hertz-Mindlin contact model are defined as follows:

$$
\begin{aligned}
&\boldsymbol{F}_{contact} = \boldsymbol{F}_n + \boldsymbol{F}_t \\
&\boldsymbol{F}_n = -k_n D_n - N_n \boldsymbol{V}_n \\
&k_n = \frac{4}{3} E_{eq} \sqrt{D_n R_{eq}} \\
&N_n = \sqrt{(5 k_n M_{eq})} N_{ndamp} \\
&R_{eq} = \frac{1}{\frac{1}{R_A} + \frac{1}{R_B}} \\
&M_{eq} = \frac{1}{\frac{1}{M_A} + \frac{1}{M_B}} \\
&E_{eq} = \frac{1}{\frac{1-{v_A}^2}{E_A} + \frac{1-{v_B}^2}{E_B}}
\end{aligned}
$$

$$
\boldsymbol{F}_t = \begin{cases} -k_t D_t - N_t \boldsymbol{V}_t & |k_t D_t| \leq |k_n D_n| C_{fs} \\ \frac{|k_n D_n| C_{fs} D_t}{|D_t|} & \text{Otherswise} \end{cases}
$$

$$N_{tdamp} = \frac{-\ln(C_{trest})}{\sqrt{\pi^2 + \ln(C_{trest})^2}}$$
$$N_{ndamp} = \frac{-\ln(C_{nrest})}{\sqrt{\pi^2 + \ln(C_{nrest})^2}}$$

In Table 2.1, all the parameters used in this contact model are defined. k is the spring stiffness (spring constant) that is the measure of the resistance offered to deformation by an elastic body. C_{nrest} and C_{trest} are coefficients of restitution for energy dissipation due to damping of normal and tangential components of the contact force, respectively.

To calculate particle-wall contact forces, the approach is the same as calculation of particle-particle contact forces, however, the wall radius and mass are assumed to be infinity. Consequently, the equivalent radius and equivalent mass will be particle radius and mass, respectively.

Table 2.1: Parameters Used in Hertz-Mindlin Model

Quantity	**Description**	**SI unit**
$\boldsymbol{F}_n$	Normal interaction force	N
$\boldsymbol{F}_t$	Tangential interaction force	N
k_n, k_t	Normal and tangential spring stiffness (spring constant)	$\frac{\text{N}}{\text{m}}$
R_{eq}	Equivalent radius m	
E_{eq}	Equivalent Young's modulus	Pa
D_n, D_t	Overlaps in the normal and tangential directions at the contact point	m
N_{ndamp}	Normal damping coefficient	[-]
M_A, M_B	Mass of particles A and B	kg
R_A, R_B	Radii of particles A and B	m
M_{eq}	Equivalent particle mass	kg
$\boldsymbol{V}_n$, $\boldsymbol{V}_t$	Normal and tangential velocity components of the relative sphere surface velocity at the contact point	$\frac{\text{m}}{\text{s}}$
v_A	Poisson's ratio of particle A	[-]
C_{fs}	Static friction coefficient	[-]
$\boldsymbol{V}_p$	Instantaneous velocity of the particle	$\frac{\text{m}}{\text{s}}$
C_{nrest}, C_{trest}	Normal and tangential coefficient of restitution	[-]

2.4 Solid-Fluid Coupling

2.4.1 Void Fraction Calculation

In simulating solid-fluid flow, the actual volume that is occupied by the fluid phase is reduced by the presence of the dispersed phase. Two projections must be done:

- Projection of particle volume onto the CFD mesh which helps to define the fluid volume fraction ϵ_f.
- Projection of the forces between solid and fluid phases onto the CFD mesh which helps to calculate the momentum exchange between the solid and fluid phases.

In the projection process, mass must be conserved and void fraction, ϵ_f, field should lead to a stable CFD simulation. The projection scheme is cell-centered in case of applying cell-centered finite volume for CFD. In this case, the void-fraction corresponding to each cell will define the void fraction. There are other projection schemes such as nodal/vortex-centered (in case of vortex-centered finite volume or finite element) where the nodal void fraction values are calculated based on the values within the cell and can be defined by a weighting procedure[86]. To calculate the void fraction, there are various methods proposed in the literature such as: particle counting method, particle cloud, conservative particle cloud, moment preserving approach, two-grid formulation, divided approach[86].

The particle counting method is a standard approach that is widely used

in solid-fluid coupling[86]. In this approach, the full volume of a particle is assigned to the cell where the centroid of that particle resides in the cell. Particle counting method is applicable for cases with $\frac{d_p}{\Delta x} \leq 3$ where d_p is the particle diameter and Δx is the CFD mesh characteristic length. The mesh needs to be sufficiently large meeting the criterion: $\frac{\Delta x}{d_p} > 3$[86]. Calculation of the void fraction is usually followed by the smoothing techniques such as parabolic filtering, darning socks and trajectory smoothing[86]. The smoothing techniques apply to smooth variable such as void fraction or momentum exchange in coupling process. They lead to diffusion of the coupling terms to cells that have not seen particles.

Another approach to calculate the void fraction is the two-grid formulation[87] which generally gives superior results[86] but complex and hard to apply in case of unstructured grids[86]. It applies a coarser grid than the CFD mesh and fluid flow is solved on a finer mesh to maintain the stability condition necessary for the particle counting method. This will result in a well-defined void fraction. In this work, two-grid formulation is applied to calculate the void fraction field. Other approaches are well-explained in the review paper written by Ariane Berard in 2020[86].

2.4.2 Hydrodynamic Forces

According to equations 2.4 and 2.7, the interaction between the particle and fluid leads to the hydrodynamic forces. The hydrodynamic forces include drag force, Basset force, Magnus lift force, Saffman lift force, pressure force, virtual mass force and viscous shear force.

The lubrication and other surface interaction forces are not directly listed in the model description, but their effect is considered by the model, as demonstrated in the bouncing particle tests in section 3.4.

Drag Force

Drag force is the result of pressure and viscous stresses that are applied to the particle surface. Drag force resists against the relative velocity and is also the result of the relative velocity between the particles and the fluid. Relative velocity is the particle velocity at the center of mass of the particle minus the extrapolated fluid velocity at the center of mass of the particle[21]. Drag force is defined as follows:

$$\boldsymbol{F}_d = \frac{1}{2} C_d \rho_f A_p |\,\boldsymbol{V}_s|\,\boldsymbol{V}_s \tag{2.12}$$

C_d is the drag coefficient of the particle, ρ_f is the density of fluid, $\boldsymbol{V}_s$ is the particle slip velocity that is the difference between the fluid instantaneous velocity and particle velocity. A_p is the projected area of the particle. The equation 2.12 is also written as

$$\boldsymbol{F}_d = \frac{m_p \boldsymbol{V}_s}{\tau_v} \tag{2.13}$$

where τ_v is the momentum relation time-scale and is defined as:

$$\tau_v = \frac{2 m_p}{C_d \rho A_p |\,\boldsymbol{V}_s|} \tag{2.14}$$

Several definitions of drag coefficient were developed as a function of particle Reynolds number and drag model. Particles experience higher drag as they become less spherical[55].

Drag Coefficient The drag coefficient is a function of the small-scale flow features around each particle. These features are not resolved spatially and drag coefficient is calculated based on correlations (submodels). These correlations are obtained from experiment or theoretical studies and are dependent to the nature of the discontinues phase. Droplets, bubbles, and solid particles have different correlations. The shape of the particle, the presence of inter-phase mass and energy transfer, and so on, affect these correlations. There are 3 drag force coefficient models available in STAR-CCM+ that can be used with the DEM drag force model having solid spherical particles.

Schiller-Naumann Correlation[6],[7] The Schiller-Naumann correlation is suitable for spherical solid particles, liquid droplets, and small-diameter bubbles. It is formulated as follows. Re_p is the particle Reynolds number.

$$C_d = \begin{cases} \frac{24}{Re_p}(1 + 0.15\ Re_p^{0.687}) & Re_p \leq 10^3 \\ 0.44 & Re_p > 10^3 \end{cases}$$

$$Re_p = \frac{\rho_f |\ \boldsymbol{V}_s| D_p}{\mu_f} \tag{2.15}$$

D_p is particle diameter and μ_f is fluid dynamic viscosity. This correlation is applicable for the viscous continuous phase.

Di Felice Drag Coefficient Method[6],[7] This drag method introduces an extra term in the fluid drag force expression to account for the presence of other particles around a particle. The Di Felice drag coefficient is given as:

$$C_d = (0.63 + \frac{4.8}{\sqrt{\epsilon_i Re_p}})^2 \epsilon^{2-\zeta} \tag{2.16}$$

$$\zeta = 3.7 - 0.65\, exp[-0.5\,(1.5 - log[\epsilon Re_p])^2] \tag{2.17}$$

where Re_p is particle Reynolds number and ϵ_i is the void fraction around a particle. $\epsilon^{2-\zeta}$ accounts for the effect of enhanced drag on a particle, due to the presence of other particles around it.

Gidaspow Drag Coefficient Method[6],[7] The Gidaspow model is useful in systems with regions of high particle density, for example, in fluidized beds. The model covers a wide range of void fractions by combining the Wen-Yu[32] and the Ergun equations[88]. STAR-CCM+ incorporates the equations in drag coefficient form as follows if $\epsilon < \epsilon_{min}$:

$$C_d = \frac{4}{3}(150\frac{1-\epsilon}{\epsilon Re_p} + 1.75) \tag{2.18}$$

Otherwise:

$$C_d = \begin{cases} \frac{24(1+0.15 Re_p^{0.687})}{\epsilon Re_p}\epsilon^{1-\omega} & \text{if} \epsilon Re_p \leq 10^3 \\ 0.44 & \text{if} \epsilon Re_p > 10^3 \end{cases}$$

ϵ is the void fraction. ϵ_{min} is the cutoff void fraction and ω is the Wen-Yu exponent.

Lift Forces

Lift forces can arise from particle rotation, particle shear (gradients in the velocity profile), or due to the shape of the particles. For the latter case, they depend on the orientation of the particles with respect to the flow[86]. In this context, lift forces refer to mean forces normal to the particle velocity and they are not necessarily forces in the upward direction. There are two main factors causing lift force for the irregularly-shaped particles: the pressure difference on an asymmetrical surface and the deviation of the center of pressure from geometric centers[86].

Particle Spin Lift Force This force applies to a spinning particle moving relative to a fluid. The force is given by:

$$\boldsymbol{F}_{lr} = \frac{\rho\pi}{8} D_p^2 C_{lr} |\, \boldsymbol{V}_s| \frac{\boldsymbol{\Omega} \times \boldsymbol{V}_s}{|\boldsymbol{\Omega}|} \tag{2.19}$$

Sommerfeld[89] defines the coefficient of rotational lift C_{lr} as below:

$$C_{lr} = 0.45 + \left(\frac{Re_r}{Re_p} - 0.45\right) e^{-0.5684 Re_r^{0.4} Re_p^{0.3}} \tag{2.20}$$

where $\boldsymbol{\Omega}$ is the relative angular velocity of the particle to the fluid also called slip-rotation and is given by:

$$\boldsymbol{\Omega} = \frac{1}{2}\boldsymbol{\nabla} \times \boldsymbol{V} - \boldsymbol{\omega}_p \tag{2.21}$$

$\boldsymbol{V}$ is the fluid velocity and $\boldsymbol{\omega}_p$ is the angular velocity of the particle. Re_p is the particle Reynolds number defined in equation (2.15). Re_r is the rotational Reynolds number and is defined as:

$$Re_r = \frac{\rho_f D_p^2 |\boldsymbol{\Omega}|}{\mu_f} \tag{2.22}$$

ρ_f is the density of the continuous phase. D_p is the diameter of the particle and μ_f is the dynamic viscosity of the continuous phase. Sommerfeld reports this formula for C_{lr} as valid for particle Reynolds numbers below 140 and restricts the rotational Reynolds number to values below 1000. In STAR-CCM+, C_{lr} can be defined using a user-defined function.

Particle Shear Lift Force This force applies to a particle moving relative to a fluid where there is a velocity gradient in the fluid orthogonal to the relative motion. Saffman[90] gives the shear lift force as:

$$\boldsymbol{F}_{ls} = 1.615 D^2 (\rho\mu)^{0.5} \left| \frac{\partial \boldsymbol{V}}{\partial y} \right| \boldsymbol{V}_s \tag{2.23}$$

The y direction is the direction of the velocity gradient. The three-dimensional version of this equation is:

$$\boldsymbol{F}_{ls} = C_{ls}\frac{\rho\pi}{8}D_p^3(\,\boldsymbol{V}_s \times \boldsymbol{\omega}_{cur}) \tag{2.24}$$

$\boldsymbol{\omega}_{cur} = \nabla \times \boldsymbol{V}$ is the curl of the fluid velocity. Saffman[90] provides a definition that recovers the original Saffman asymptotic solution for low Reynolds numbers:

$$C_{ls} = \frac{4.1126}{Re_s^{0.5}} \tag{2.25}$$

Sommerfeld[89] provides a definition for a broader range of Reynolds numbers:

$$C_{ls} = \frac{4.1126}{Re_s^{0.5}} f(Re_p, Re_s) \tag{2.26}$$

$$f(Re_p, Re_s) = \begin{cases} (1 - 0.3314\beta^{0.5})\; e^{-0.1Re_p} + 0.3314\;\beta^{0.5} & \text{if } Re_p \leq 40 \\ 0.0524\;(\beta Re_p)^{0.5} & \text{if } Re_p > 40 \end{cases}$$

$$\beta = 0.5\;\frac{Re_s}{Re_p} \tag{2.27}$$

Re_s is the Reynolds number for shear flow:

$$Re_s = \frac{\rho D_p^2 |\boldsymbol{\omega}|}{\mu} \tag{2.28}$$

C_{ls} can be also defined as a user-defined field function.

Gravity Force

The gravity force is defined as:

$$\boldsymbol{F}_g = m_p \boldsymbol{g} \tag{2.29}$$

where $\boldsymbol{g}$ is the gravitational acceleration.

Pressure Gradient Force and Shear Stress Force

When particles are subject to gravity and acceleration in fluid, undistributed flow is present and it includes forces due to pressure gradients and shear stress. These forces are non-negligible when density ratio of the fluid and solid is around 1 or the surrounding fluid is viscous[32]. The pressure gradient force is defined as[81]:

$$\boldsymbol{F}_p = -V_p \boldsymbol{\nabla} P_{static} = -\frac{1}{6}\pi D_p^3 \boldsymbol{\nabla} P_{static} \tag{2.30}$$

and the shear stress force is[81]:

$$\boldsymbol{F}_\tau = -V_p \boldsymbol{\nabla} \cdot \boldsymbol{\tau} \tag{2.31}$$

where V_p is the volume of the particle, $\boldsymbol{\nabla} P_{static}$ is the gradient of the static pressure in the continuous phase and $\boldsymbol{\tau}$ is the shear stress.

Virtual Mass Force

The virtual mass force is the force that particle exerts on the fluid when particle velocity is changing. It is a transient force only occurs in an unsteady flow

system and negligible when the velocity of the flow and particle are equal. This force is equivalent to adding a virtual mass to a sphere. A general form of function for virtual mass force is[25]:

$$\boldsymbol{F}_{vm} = C_{vm}\rho V_p\left(\frac{\dot{\boldsymbol{u}} - \dot{\boldsymbol{v}}}{2}\right) \tag{2.32}$$

$$C_{vm} = 2.1 - \frac{0.132}{0.12 + \boldsymbol{A}_c^2} \tag{2.33}$$

$$\boldsymbol{A}_c = \frac{(\boldsymbol{u} - \boldsymbol{v})^2}{D_p \frac{d(\boldsymbol{u}-\boldsymbol{v})}{dt}} \tag{2.34}$$

where C_{vm} is the virtual mass coefficient. This coefficient equals to 0.5 for a sphere in a uniform, inviscid and incompressible flow[91]. ρ is fluid density, D_p is particle diameter (m) and V_p is the volume of the particle. $\dot{\boldsymbol{u}}$ and $\dot{\boldsymbol{v}}$ are particle and fluid acceleration, respectively.

Basset Force

Basset force applies to an unsteady flow as a virtual mass force and known as history force[24]. It is a viscous effect and is negligible when the particle acceleration is low and for the gaseous systems with the low viscosity. It accounts for the temporal delay in the boundary layer around the particle. This boundary layer is created when the relative velocity changes with time[86].

A common model to define the Basset force is defined as[6]:

$$\boldsymbol{F}_{Basset} = \frac{3}{2} D_p^2 \sqrt{\pi \rho_f \mu_f} \left[\int_{t_0}^{t} \frac{\boldsymbol{u} - \boldsymbol{v}}{\sqrt{t - t'}} dt' + \frac{(\boldsymbol{u} - \boldsymbol{v})_0}{\sqrt{t}} \right] \tag{2.35}$$

Equation (2.35) is based on the integral of the particle acceleration.

Figure (2.1) presents a simplified schematic of the forces acting on a particle in a fluid and forces between interacting particles in a fluid.

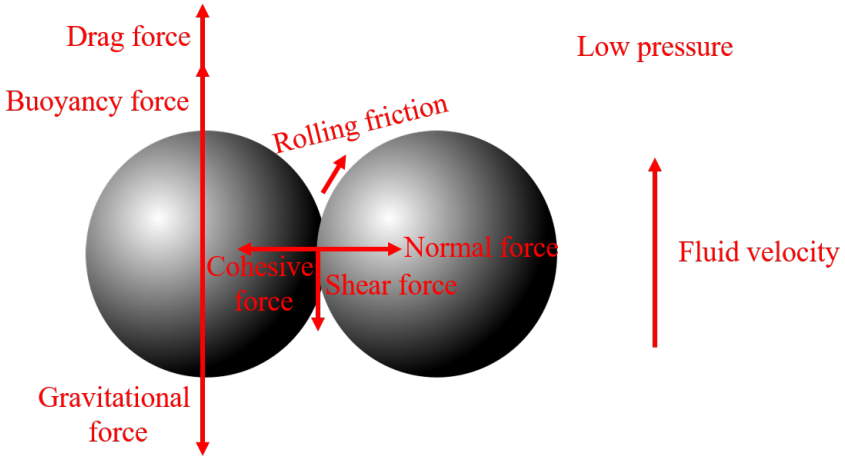

Figure 2.1: Forces acting on a particle in a fluid and forces between interacting particles in a fluid.

2.4.3 Coupling Approaches and Grid Resolution

The coupling refers to momentum, heat, and mass exchanges between the continuous phase and the dispersed phase. The important contribution to the particle-fluid momentum exchange is established by the drag force dependent on the granular volume fraction. In contrast to the drag force acting on a single sphere, the granular volume fraction must be considered for the drag

force calculation in the CFD-DEM coupling.

Zero-way, One-way and Two-way Coupling

There are three general ways of coupling approaches between the solids and the fluid flow:

- Zero-way coupling or uncoupled where dispersed phase and continuous phase evolve independently.
- In one-way coupling, the dispersed phase feels the continuous phase influence and the effect of the dispersed phase on the fluid is not taken into account.
- In two-way coupling, the effects of the dispersed phase on the continuous phase and the effects of the continuous phase on the dispersed phase such as displacement, inter-phase momentum, mass, and heat transfer are considered.

In all three coupling approaches, the particle-particle interactions and particle-domain interactions have been considered.

Coupling and Grid Resolution

From the perspective of the momentum exchange between fluid and particles, CFD-DEM coupling can be of two types: unresolved and resolved. This distinction is based on the method used for calculation of the forces on the particles. Depending on the method used, the resolution of the mesh must be adapted to the size of the particles.

- Unresolved: In this approach, DEM is applied to calculate particle motion without resolving the detailed flow around each particle. Submodels are used to calculate the forces on each particle and the same models are used as momentum sources in the CFD simulation. In unresolved approach, the fluid flow is solved without resolving the flow around the particle. Generally, it means that the mesh is coarser than the particle size. Then the coupling is established by submodels consisting of expressions for the drag force and other forces[86].

- Resolved: Resolved methods simulate the detailed flow around the particles and calculate the forces between the flow and particles without submodels. Resolved methods require a grid much finer than the particle size, and they can also deal with complicated geometries where small grids are necessary to increase the accuracy. Resolved DEM means that the fluid flow around each particle is resolved. Consequently, the coupling between the fluid and the particles is conducted by applying a no-slip boundary condition. There is no need to use submodels to calculate the forces on particles. The forces applied to the particle are due to the application of the no-slip boundary condition at the surface of the particle. For this reason, the grid resolution must be much smaller than the particle size.

In STAR-CCM+, DEM simulations coupled with CFD are always unresolved. But the software allows for continuous mesh refinement, including meshes that are finer than the particle size. The particle equations of motion

are based on contact theory and Lagrangian tracking. The particle position is tracked by the Particle Centroid field function, and its shape is also a property of the particle. From these, contact detection algorithms are used to determine when a particle is contacting either another particle or a wall. This is represented by an overlap of the particle with the opposing particle. The force exerted between the particles is a function of the size of the overlap, as well as material properties such as Young's Modulus. Larger overlap means a larger repulsive force between the particles. This calculation is done on a particle by particle basis, with wall contacts using the surface mesh for its geometry. When DEM is coupled with CFD, one or more additional forces are applied to the particle from the CFD results. Usually, this includes a pressure gradient force and a drag force. These forces are calculated based on the data in the cell that the particle centroid is located in. These flow-based forces are applied to the particle as momentum source terms, and together with the contact forces are used to determine the motion of the particle. If the two-way Coupling model is activated, the equal and opposite momentum source term is applied in the CFD model to the cell in which the particle centroid resides.

This unresolved approach will never show a flow redirecting around the surface of a particle, because the particle shape is not resolved.

In STAR-CCM+, when the particle size is smaller than the grid size, the approach will be called "coarse grid unresolved method" or "coarse unresolved" for short in this thesis. The case with grid refinement, that is when the particle size larger than the grid size, will be called "smoothed source on refined grid unresolved method" or "smoothed unresolved" for short in this thesis.

The resulting impact on the flow is an effect similar to a porous zone in the cell where the centroid is. While this impact is confined to a single cell in coarse grids (coarse grid unresolved approach), in the case of fine grids (refined grid unresolved approach) this source term needs to be adjusted for two-way coupling. If a particle is larger than a cell, the forces applied to the particle can be much larger than the fluid in the cell will realistically experience. This can cause unphysical velocities and instability. In STAR-CCM+, this issue of the refined grid unresolved approach is solved by using the Volume Source Smoothing technique, which is activated in the Lagrangian solver settings. This technique creates a secondary grid composed of cells from the original grid, which is used exclusively for the two-way coupling. The smoothing technique ensures that the momentum source is spread across several cells occupied by the particle. During smoothing, the "volume fraction" scheme is used to calculate the void fraction and forces.

Unresolved CFD-DEM Coupling The unresolved CFD-DEM coupling routine consists of the following steps[77]:

1. Particles positions and velocities are calculated in the DEM solver.
2. Particles positions and velocities are passed to the CFD solver.
3. The corresponding cell in the CFD mesh is determined for each particle.
4. The volume fraction and a mean particle velocity are determined for each CFD cell.

5. The fluid forces acting on the particles are calculated based on the particles volume fraction and equations are integrated over the cell.

6. Particle–fluid momentum exchange terms are calculated from particle-based forces by averaging over all particles in one CFD cell.

7. The forces on the particles due to the flow field are transferred to the DEM solver to be applied in the next time step.

8. Considering the local volume fraction and momentum exchange, the CFD solver calculates the velocity and the pressure of the fluid in the CFD cells.

9. Additional equations can be optionally solved for both phases such as heat transfer.

10. The routine is repeated from the beginning.

The unresolved CFD-DEM coupling approach is the only one used in this work, as implemented in STAR-CCM+. It is also called the refined grid unresolved approach. For this refined grid unresolved approach, the steps are very similar to those described above. The only difference occurs in steps 5 to 7, when the Volume Source Smoothing technique is used to distribute the momentum sources across all affected cells, instead of a single cell.

The whole picture of the CFD-DEM model that has been applied to the subsequent chapters problems is presented in Figures (2.2) and (2.3).

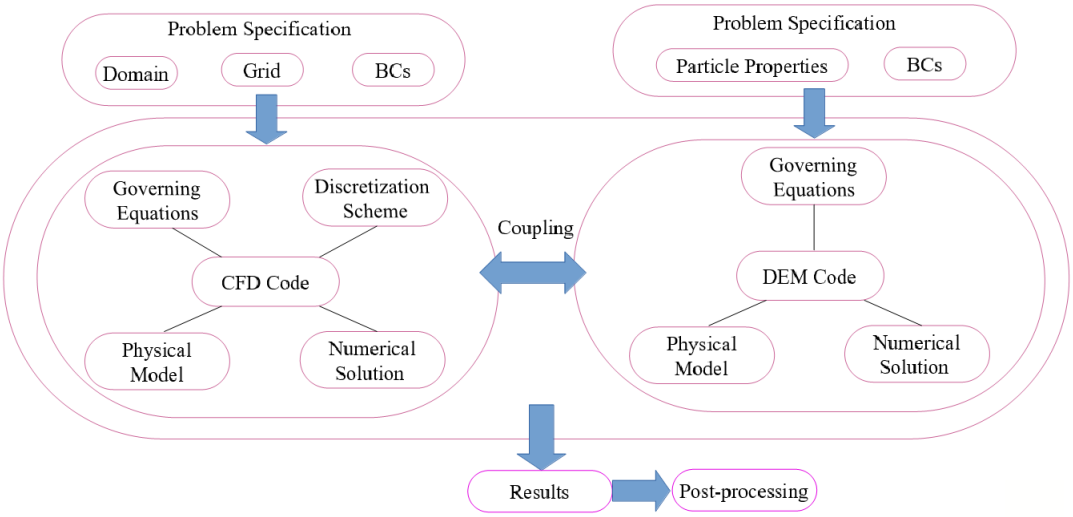

Figure 2.2: Steps of numerical simulation of the CFD-DEM model.

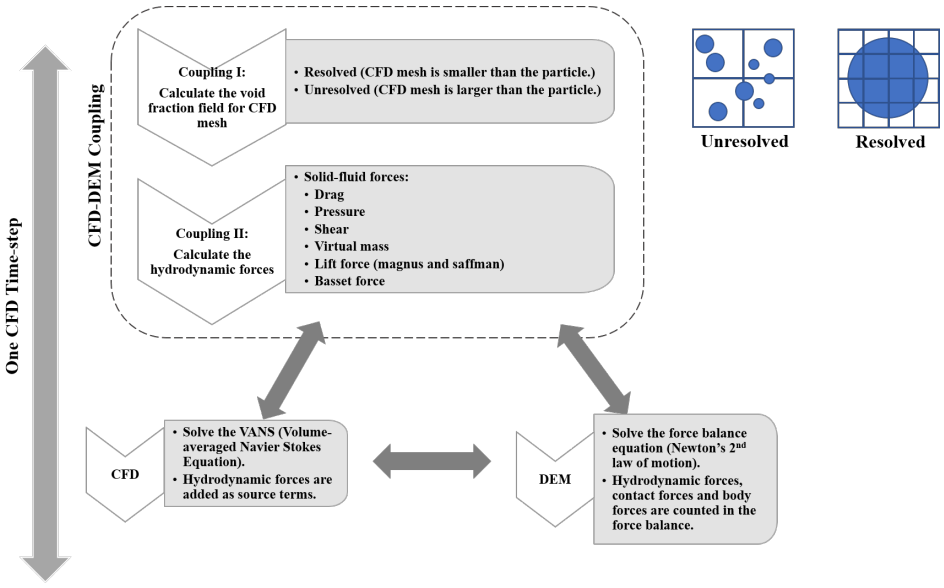

Figure 2.3: CFD-DEM coupling

2.5 Discretization Scheme and Numerical Solution Method

2.5.1 CFD Discretization Scheme

Discretization methods are applied to convert the continuous system of equations to a set of discrete algebraic equations which can be solved by applying numerical techniques. Discretization methods follow similar steps[5]:

1. The continuous domain is divided into a finite number of cells called mesh.

2. The unknowns are stored at vertices, cell centroids, face centroids, or edges of the cells.

3. The integral form of the differential equations is used for spatial discretization. Following discretization, a non-linear system of algebraic equations is solved at each time-step.

In the current work, finite volume method is applied to transform the mathematical model into a system of algebraic equations. This transformation includes discretizing the governing equations in space and time. The resulting linear equations are solved with the Algebraic Multi-grid (AMG) solver. The theory behind the AMG linear flow solver can be found in[6]. For transient (unsteady) problems, the physical time interval is divided into an arbitrary number of sub-intervals called time steps. The general settings for the discretization schemes applied to the Navier-Stokes transport equations are as

follows:

- For the convective flux term, second-order upwind discretization scheme is used.
- For the diffusive flux term, second-order central difference discretization scheme is used.
- To have high-accuracy temporal discretization, the temporal discretization is mainly set to the second-order in the implicit unsteady solver for transient simulations.

2.5.2 DEM Numerical Solution Method

Contact detection between the particles colliding is the number one task following calculation of the contact force[6] in DEM calculations. This is done by the DEM solver. Detailed information on various algorithms used to detect contacts are presented in[6]. Grid scale is the key parameter used in contact detection in the DEM solver. It parametrizes the particle-particle and particle-wall contacts and affect the CPU time required to detect all collisions. Grid scale for specific packing is important since one of the main problem of the interest is fluid/solid flow in the packed bed.

In this research work, the contact detection is employed through tree-based algorithms or grid-based algorithms as implemented in STAR-CCM+. C-Grid (or D-cell) is used in the current research. The code builds a virtual hexahedral mesh in the background and only particles from neighboring cells are considered for collisions. The optimal value for the grid scale, Table 2.2, is dependent on

the particle size distribution and density of the packed bed. This can be used to fine-tune the parameter for specific packing. The CPU time of DEM contact detection is trackable by turning on the verbose parameter in STAR-CCM+. Following the contact detection, the DEM equations are integrated in time using time integration schemes[86]. Great details on time integration schemes can be found in[6].

Table 2.2: Grid scale as a fine-tune parameter for the specific packing.

Particle Distribution	Packed Bed Density	Grid Scale	Base Mesh Cell Size
Uniform	Dense	1	= grid scale × particle diameter
Non-uniform	Sparse	> 1	= grid scale × particle diameter

2.6 Summary

An overview of the particulate flow modeling was presented in this chapter. The theory behind the discrete element method was discussed. Mathematical model of particulate flow modeling applied in this research, CFD-DEM modeling, was presented in details. The data transfer between the two phases, solid-fluid coupling, was discussed. Finally, discretization scheme and numerical solution method applied in this work were reviewed.

Chapter 3

Verification and Validation

The main purpose of this chapter is to verify and validate a CFD-DEM model. This model will be applied to investigate the particulate flow in an opening of the sand screen applied in the oil industry for sand control in the next chapter. This verification and validation process includes solving benchmarking problems to assure that the developed model was capable of capturing the physics of the particle-fluid, particle-wall and particle-particle interactions.

3.1 Flow Through the Wire-Wrapped Screen: CFD Model Verification and Validation

As an initial phase of this research, computational fluid dynamic (CFD) was applied to investigate the details of the interaction between the near well-bore flow and the flow of fluids through and along the wire-wrapped screens (WWS). The study started with the single phase flow simulation of water in WWS. The

CFD model in the pipe and wire-wrapped screen governed by the Navier–Stokes equations was coupled to the porous media model outside of the well, governed by the modified Darcy's law, the Ergun equation. A laminar-steady state CFD model was applied to investigate the flow behavior in wire wrapped screen in SAGD production well and study the effect of the particle size distribution in porous media on the flow in wire wrapped screen. The particles in porous media were assumed to be not transportable. Consequently, flow in WWS and pipe was single phase flow of oil. This work was a feasibility study on CFD application in wire wrapped screens as well as a parametric study which gave us an assessment of the practicality of CFD and the work-flow for next complex models.

Introduction to SAGD and WWS Steam assisted gravity drainage (SAGD) is an eminent heavy oil recovery technique broadly used in Alberta, Canada[33]. In SAGD operations, there are two horizontal wells drilled into the depth of 300 meters in the reservoir[33]. The wells are five meters vertically apart and their length is between 500 to 1000 meters. Steam is injected into the top well injection well to warm up the formation and lower the viscosity of the oil. Due to gravity, heated oil flows down to the production well located underneath the injection well and get produced to the surface[33]. In most sandstone reservoirs, sand is produced with oil. This process is called sanding. Sanding occurs near the wellbore area because of redistribution of stresses during drilling or production[92]. Control and mitigation of sand production is crucial to achieving maximum well productivity as well as well-bore stability.

Wire-wrapped screens (WWS) are sand control devices commonly used for thermal oil sands recovery operations, such as SAGD, in both injection and production wells[93]. Wire-wrapped screens can be designed as a base pipe with holes and wrap wires around it. Wrap wires are attached to the based pipe through rib wires parallel to the base pipe. Flow comes from around the pipe; solid particles make bridges on wrap wires and liquid flows into the pipe. Solid particles get screened by the wrap wires. Figure 3.1 shows a WWS; base pipe with hole, rib wires parallel to the base pipe and wrap wires.

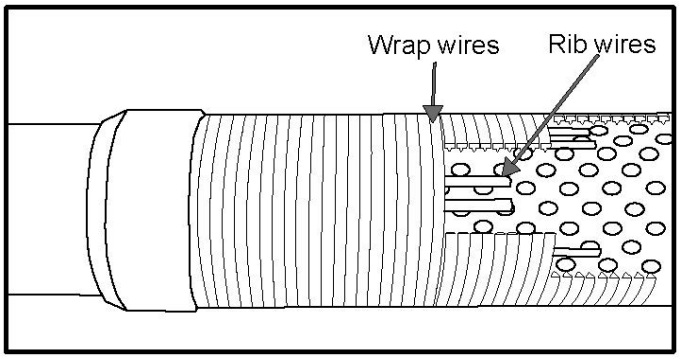

Figure 3.1: Wire-wrapped screen adapted from premiumcompletion.com

To predict the flow performance in WWS, the interaction between near well-bore flow and the flow of fluids through and along the WWS should be investigated. Hole pattern, wrap wire cross section, rib wire cross section, rib wire distances, and particle size distribution in porous media are among parameters that could affect the flow behavior in WWS. By investigating the PSD, the impact of formation heterogeneities and well-bore heterogeneities is quantifiable. The objective of this research was to have a computational fluid dynamic model of a WWS and the porous media around it to complete this

investigation. There are few studies done in this area numerically where the focus has been on other types of sand screen devices, not WWS[93].

3.1.1 Single Phase Flow Simulation of Athabasca Oil in WWS

PSD of the reservoir as a parameter could affect the flow in the sand screen device. A comparative study was conducted on four PSDs using conditions that simulate a SAGD production well. Porous media around the well was coupled with the fluid region inside of the WWS. Pressure and velocity fields were assessed and compared in various parts of the model. The effect of particle size distribution on the flow and pressure drop along the WWS was investigated. The solid domain of a WWS was created in 3D-CAD, STAR-CCM+. The fluid domain was extracted for a pie-shape section of the domain consisting of two rib wires and a hole located between them. Figure 3.2 presents the WWS solid domain and the extracted fluid in a pie-shape of the WWS domain. The dimensions of the pie-shape is also shown.

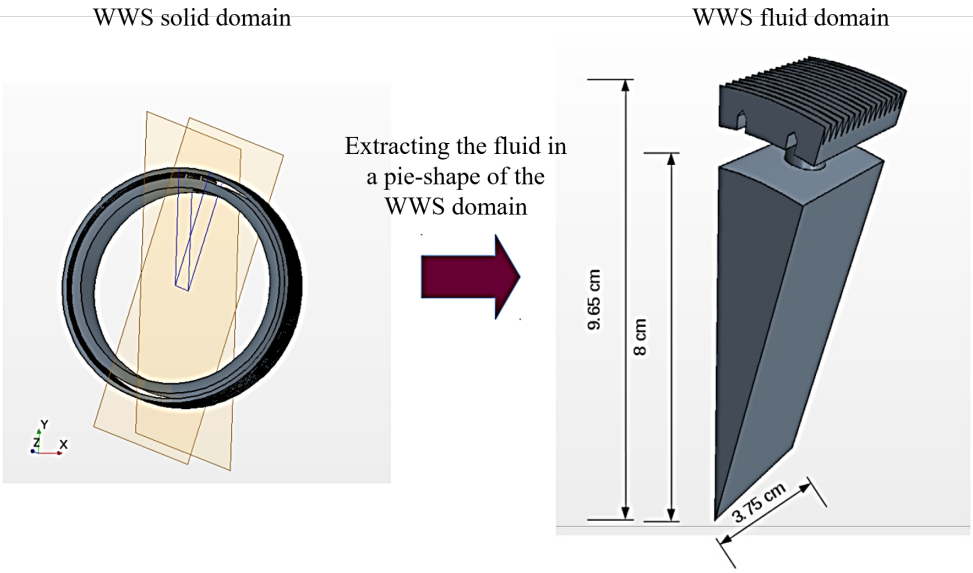

Figure 3.2: Solid-domain on the left and extracted pie-shape fluid domain dimensions on the right.

Two porous regions around the well-bore were considered (Figure 3.3). The closest to the well-bore was unconsolidated porous region with higher porosity (ϕ), while the next region, away from the well-bore, was a consolidated porous region with lower porosity than the unconsolidated region. Oil was passing through consolidated porous media, unconsolidated porous media, WWS, annular region, orifice and finally flowed into the pipe (Figure 3.4).

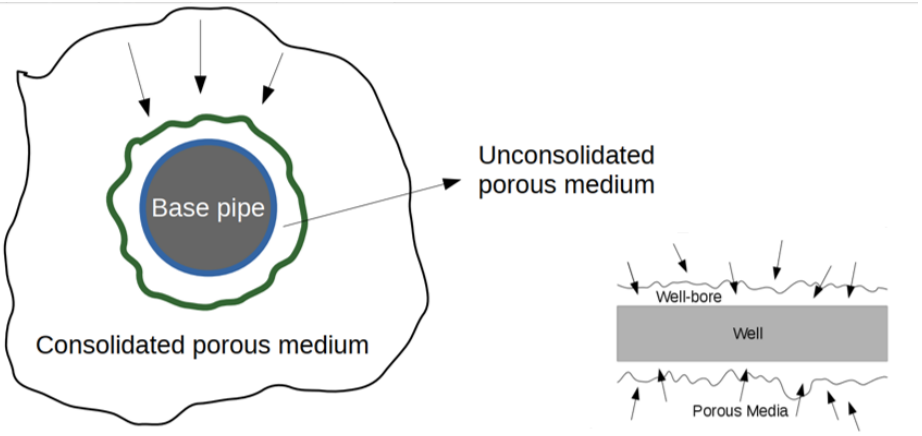

Figure 3.3: Presentation of consolidated and unconsolidated regions.

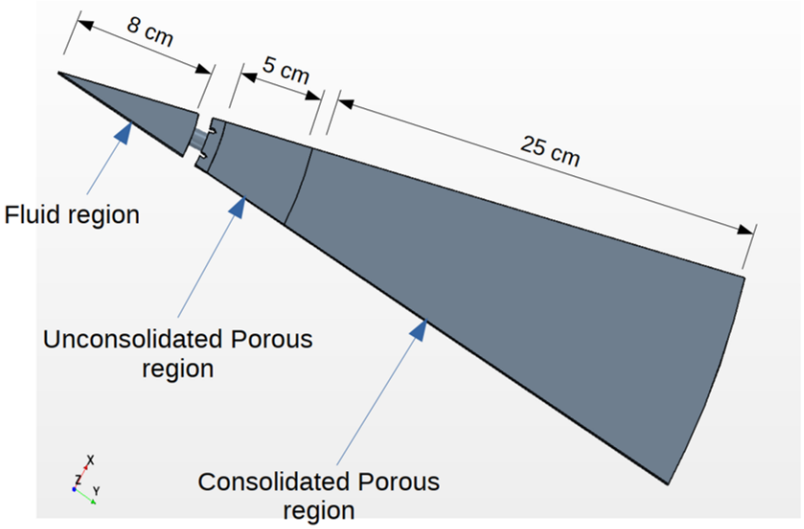

Figure 3.4: Three regions of study: fluid, unconsolidated and consolidated porous media with dimensions.

The properties of porous media can be estimated through lab experiments as well as theoretical methods. Porous media are characterized with porosity and permeability[36]. PSD is a measurement of the size of the particles (weight

based), which also helps to characterize porous media and can be related to permeability. In this work, Equation 3.1, the Berg equation[94] was used to estimate the permeability considering various PSDs. It connects the permeability with the porosity and two characteristic particle sizes, which are D_{10} and D_{50}. The portion of particles with diameters smaller than D_{10} is 10%. The portions of particles with diameters smaller and larger than D_{50} are 50%, also known as the median diameter. Uniformity coefficient (UC) is a statistic used to describe porous media. It is defined as the ratio of D_{60} over D_{10}. The portion of particles with diameters smaller than D_{60} is 60%. In Equation 3.1, C is a constant[94], ϕ is porosity and PD_ϕ is in Krumbein phi scale. D_{50} is in millimeter, and k is permeability in Darcy.

$$k = C\phi^{5.1} D_{50}^2 e^{-1.385 PD_\phi} \tag{3.1}$$

$$PD = D_{10} - D_{50} \tag{3.2}$$

Darcy's law was used to model fluid flow through porous media[95]. Ergun equation, Equation 3.3, was applied as an empirical model for the pressure drop through a packed bed. There are two resistance factors, called inertial (P_i)and viscous resistance (P_v) factors, in the Ergun equation to connect viscosity, porosity, particle size, velocity and density to pressure drop in porous media [7].

$$-\frac{dp}{L} = \frac{150\mu(1-\phi)^2}{D_p^2\phi^3} v + \frac{1.75\rho(1-\phi)}{D_p\phi^3} v^2 = P_v v + P_i v^2 \tag{3.3}$$

where

$$P_v = \frac{mu}{k} \tag{3.4}$$

In Equation 3.3, μ is dynamic viscosity, ϕ is porosity, D_p is particle diameter. P_v and P_i are viscous and inertial resistance factors respectively.

Inlet boundary condition was set at the beginning of the consolidated region as well as at the inlet of the flow inside of the pipe. Symmetry and periodic boundary conditions were set at the rest of the domain. To avoid a reversed flow, the outlet was forced to be far from the inlet in the pipe. Figures 3.5 presents the assigned boundary conditions. Polyhedral mesh was used to discretize the domain due to the balance between the accuracy and computational cost. The discretized domain is presented in Figure 3.6.

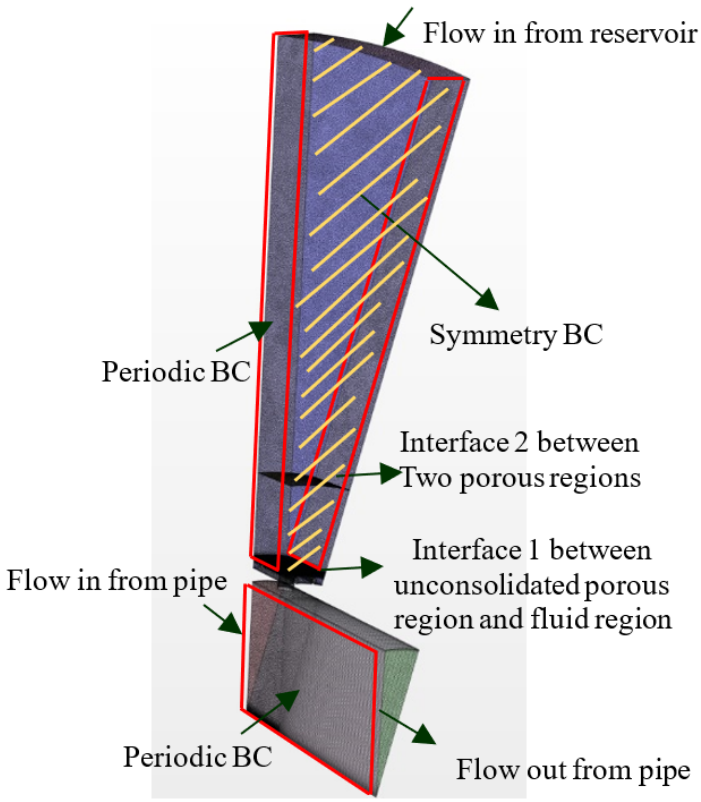

Figure 3.5: Assigned boundary conditions to the domain.

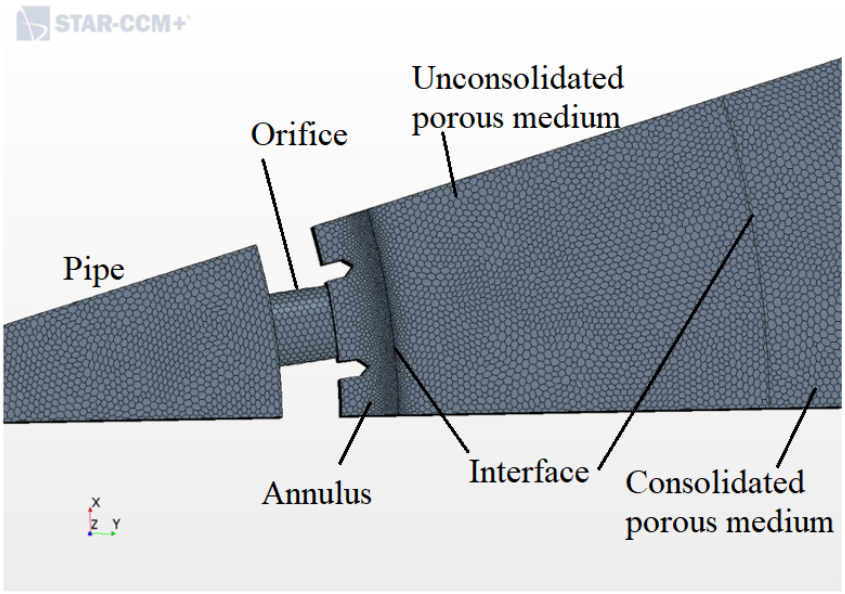

Figure 3.6: Domain discretized with the polyhedral mesh: total numbers of cells less a million.

There is usually oil, water, gas flow in the well besides unscreened solid particles. At this stage, the focus was on the single-phase flow of oil.

The Athabasca bitumen thermophysical properties were used in the simulations at 190 °C and 2.5 mPa[96]. Experimental dynamic viscosity and density of bitumen was considered as 13.6 mPa $\cdot$ s and 915.2 $\frac{\text{kg}}{\text{m}^3}$, respectively. The production rate is assumed to be 260 $\frac{\text{m}^3}{\text{day}}$ which is within the range of oil production for SAGD production well. Velocity in the pipe is 0.15 $\frac{\text{m}}{\text{s}}$. The Reynolds number in the pipe is 1615. The flow regime in the pipe is laminar and in porous media and WWS inlet is creeping as the Re was much less than 1 ($Re = 0.03$). This pie section of the well was assumed to be located at the heel of the production well since there is an accumulation of the flow at the heel and the flow will be fully-developed. For this reason, the fully-developed

flow in the pipe was simulated separately and the parabolic velocity profile was extracted as the inlet boundary condition inside the pipe for the pie section Figure 3.7.

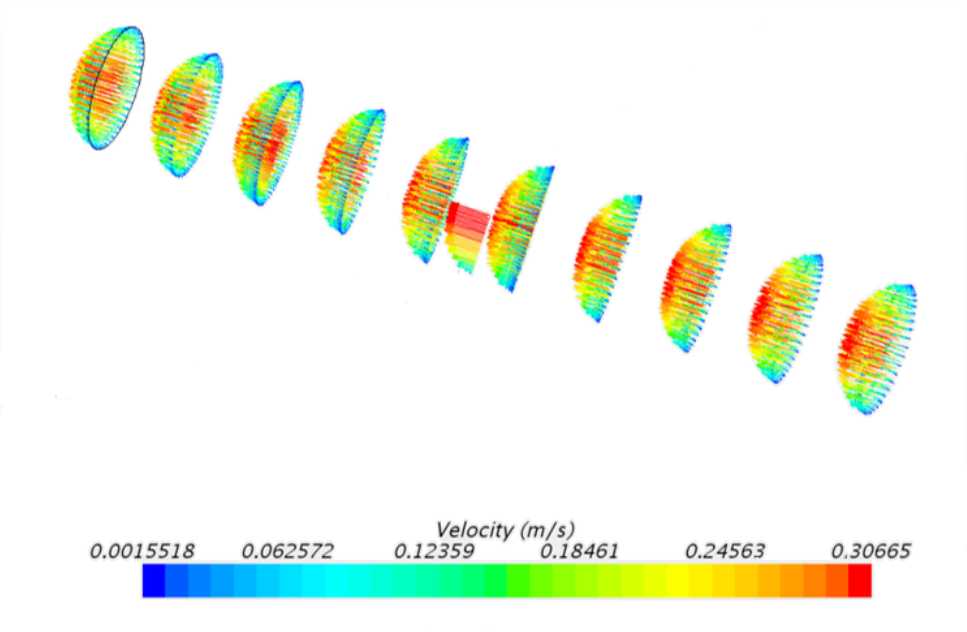

Figure 3.7: Simulated fully-developed flow in the pipe to extract the inlet boundary condition inside the pipe.

Here is the list of assumptions that have been applied to the model:

- The fluid is oil (single phase flow).
- The porous media particles are not transportable.
- The flow is incompressible.
- The process is isothermal.

- Gravity effect is neglected, which means the pie-section could be in any location of the WWS.
- Permeability is isotropic.
- Flow is steady state.

3.1.2 Results and Analysis

This part presents results on the interaction of the incoming jet and the flow in the pipe. The effect of particle size distribution in porous media on flow through WWS and into the pipe is also discussed.

Figure 3.8 presents the simulation results of velocity magnitude contour plot on a section plane. Velocity is maximum in the middle of the pipe and zero close to the pipe wall. In Figure 3.8, velocity is higher when the flow is facing a contraction and where the streamlines are closer, which is known as vena contracta and is highlighted by ovals in Figure 3.9. Figure 3.10 presents pressure contours (gauge pressure) at the T-junction. The pressure values are the highest at the inlet of the WWS and when it comes down to the hole, the pressure is lower as expected.

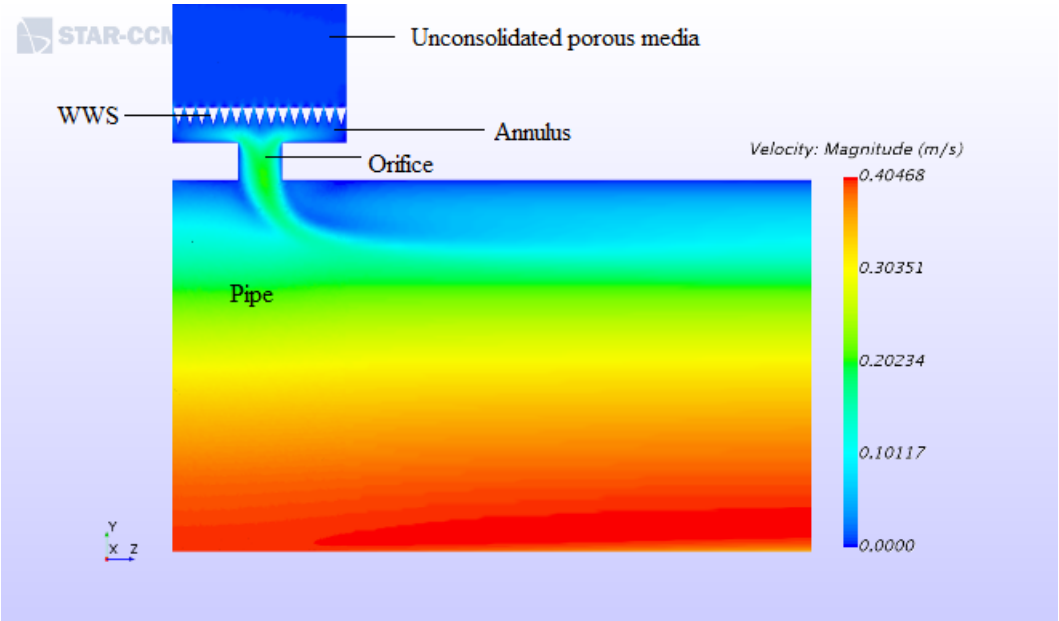

Figure 3.8: Velocity magnitude contours at the pipe, orifice, annulus and WWS.

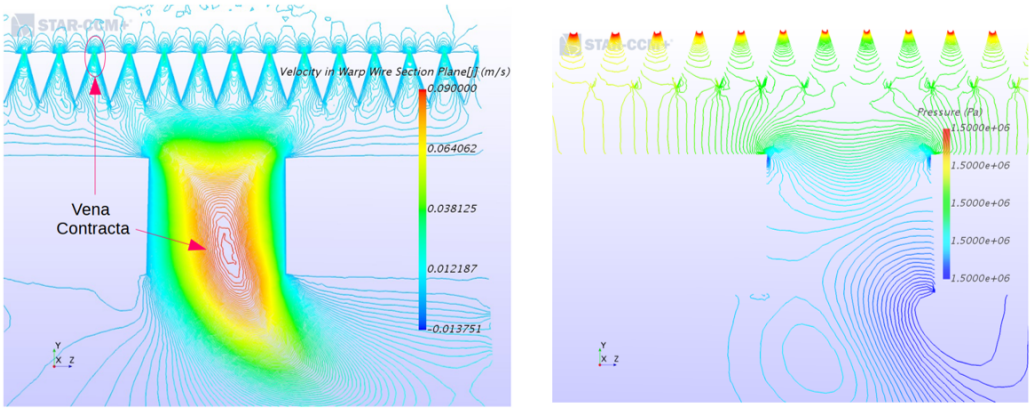

Figure 3.9: Velocity magnitude and pressure contours in T junction of fluid domain.

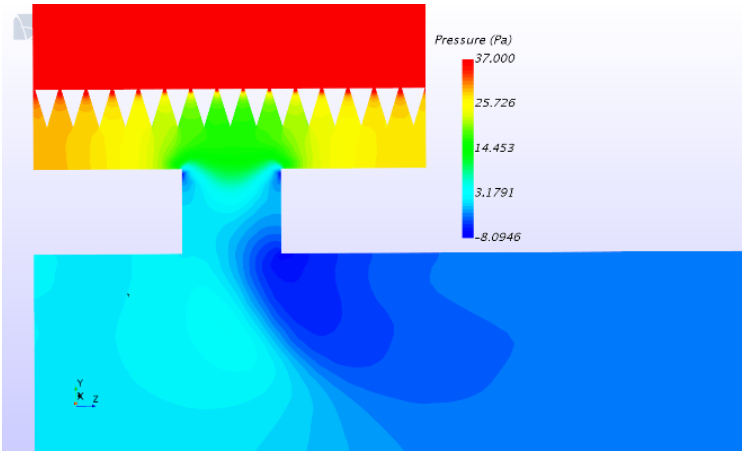

Figure 3.10: Pressure contours at T junction.

There were stagnation zones at the rib wire locations, where flow hits a wall, Figure 3.11. The pressure drop was low in the pipe and in the annular region. In Figure 3.12, velocity magnitude vectors revealed a flow separation region after the jet comes into the pipe. Figure 3.12 shows this region through vectors and streamlines. In fact, the jet coming down into the pipe from the hole is acting like a barrier and produces the separation. At the separation, there is recirculation. Streamlines in Figures 3.13, 3.14, 3.15 present this separation region better. Figure 3.16 presents fluid flow simulation in the whole domain. Low velocity in the porous media and maximum velocity in the middle of the pipe are obtained.

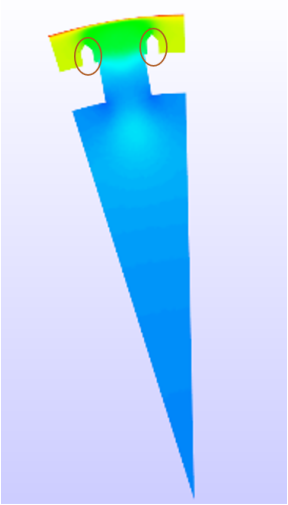

Figure 3.11: Stagnation zones at the rib wire locations.

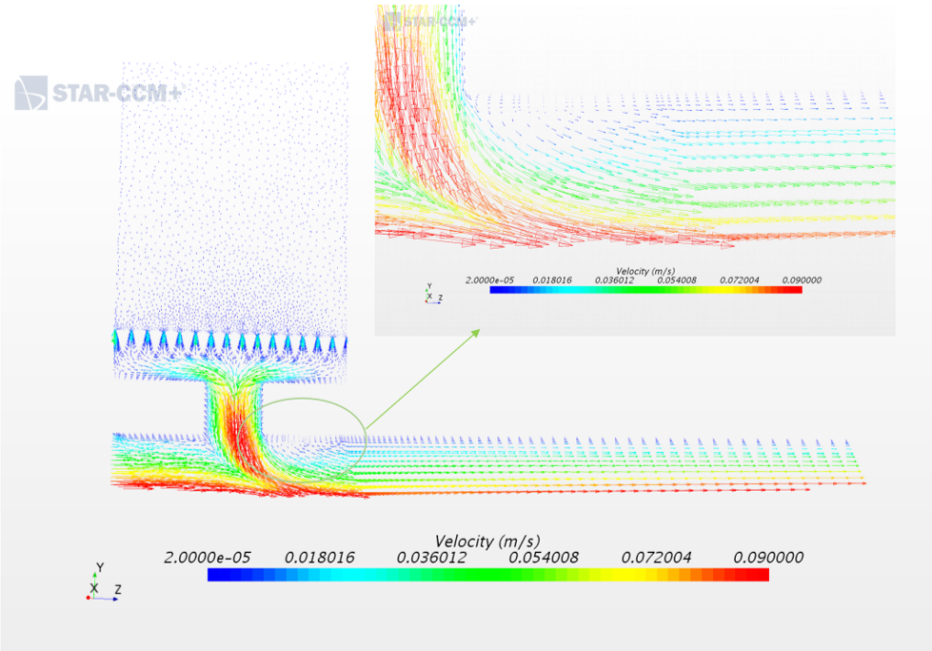

Figure 3.12: Velocity (magnitude) vector and recirculation region.

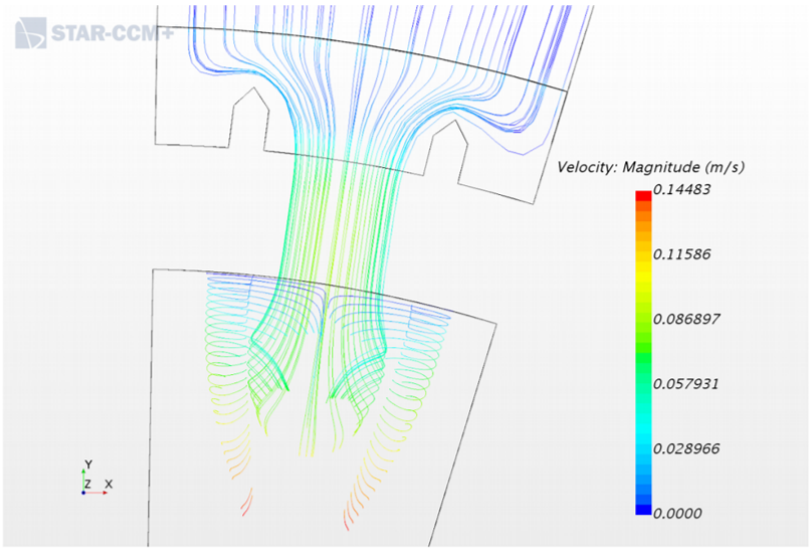

Figure 3.13: Streamlines showing flow separation colored with velocity magnitude.

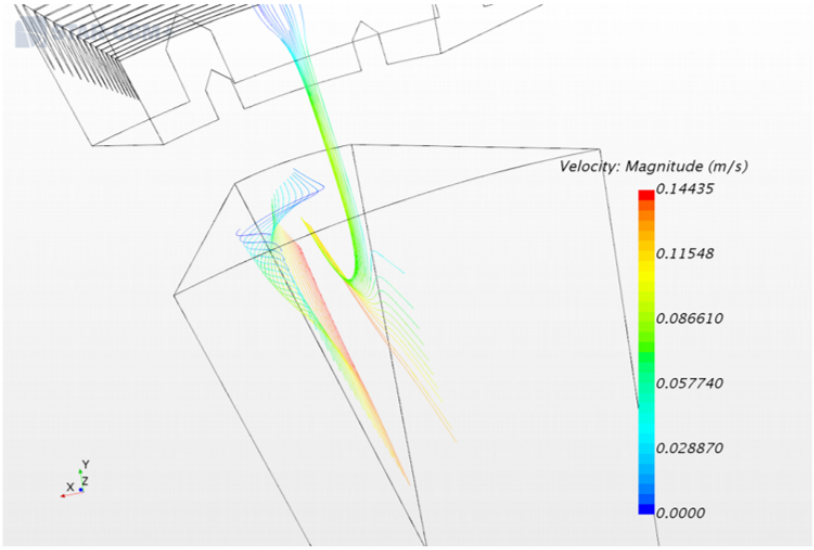

Figure 3.14: Streamlines showing flow separation colored with velocity magnitude.

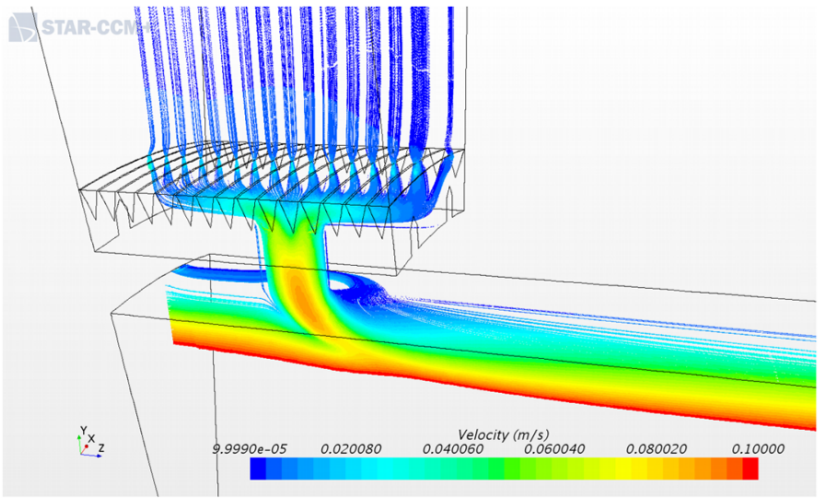

Figure 3.15: High-density streamlines on a middle section plane colored with velocity showing flow separation.

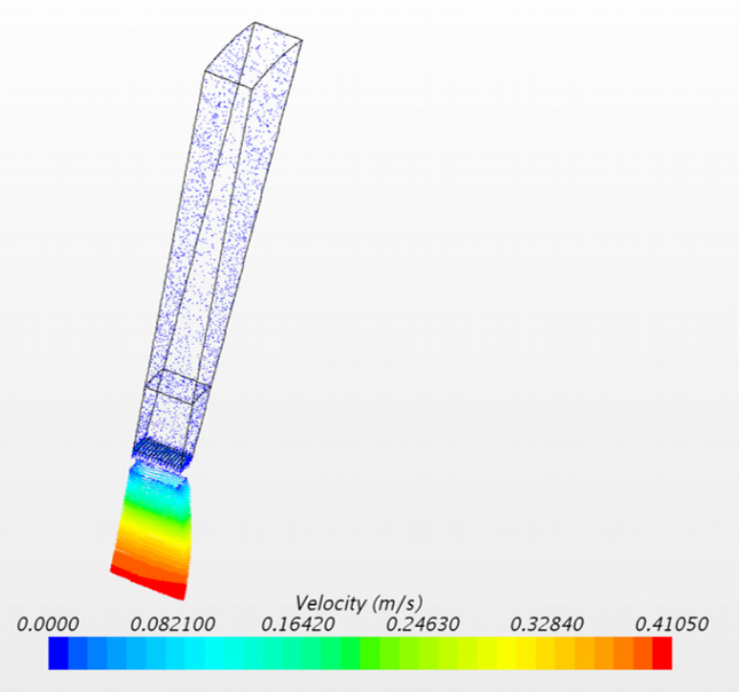

Figure 3.16: Fluid flow simulation in the whole domain: low velocity in the porous media and maximum velocity in the middle of the pipe.

3.1.3 Particle Size Distribution in Porous Region

It is important to investigate the effect of PSD on the flow features in WWS, which is the focus of this part. For this purpose, four simulation cases were studied considering different particle size distributions. D_{10}, D_{50} and UC data sets were taken from the work of Romanova et. al[36]. The effects of packing, grain size, sorting, and grain shape were combined through a general expression for permeability proposed by Berg[94]. This equation gives an approximation for maximum permeability of well-sorted grain. Typical porosity values for well-sorted sedimentary materials are between 30-40 %[97].

Table 3.1: Calculated permeability values for four PSDs based on Berg's equation

Porosity	Case	D10 (micron)	D50	Permeability (darcy)
Consolidated porous region: 30%	1	236	140	1.9678
	2	245	178	1.5505
	3	473	230	33.9705
	4	236	162	1.5664
Unconsolidated porous region: 40%	1	236	140	8.5344
	2	245	178	6.7244
	3	473	230	147.3294
	4	236	162	6.7933

In this work, porosity of the consolidated and unconsolidated regions was set to 30% and 40% respectively for all cases. Having the porosity values and PSDs, permeability was calculated by Berg's formula as presented in Table 3.2. By using Ergun's equation (Equation 3.3)[88], the viscous and inertial resistance factors are calculated and used as an input to the porous media model in STAR-CCM+. Velocity at WWS inlet when flow faces contraction was calculated as 10.73 $\frac{\mathrm{m}}{\mathrm{day}}$. Velocity in porous media would be even smaller than this value.

Low velocity in porous media makes inertial forces small and negligible. Low velocity in porous regions are presented in Figure 3.16. The PSD is connected to the CFD model via Berg's formula and Ergun's equation (Equations 3.1 and 3.3).

3.1.4 Results of Four Case Studies

16 probes were located at various places of the domain to extract and compare the simulated pressure and velocity fields. Some of them are presented in Figures 3.18 and 3.17.

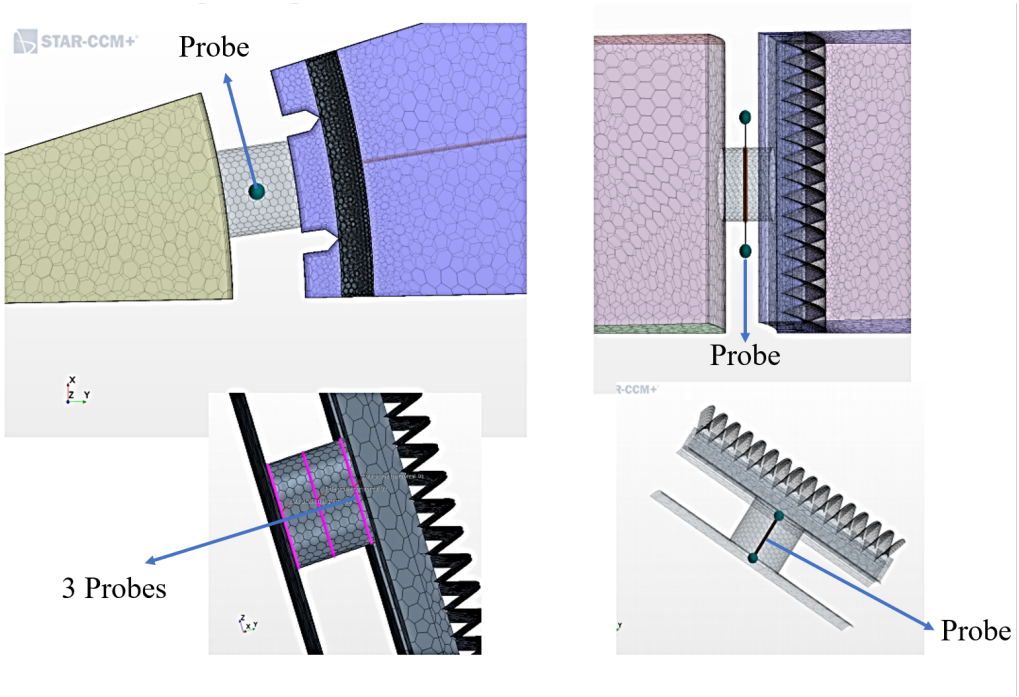

Figure 3.17: Presentation of probes located at various parts of the model to extract data.

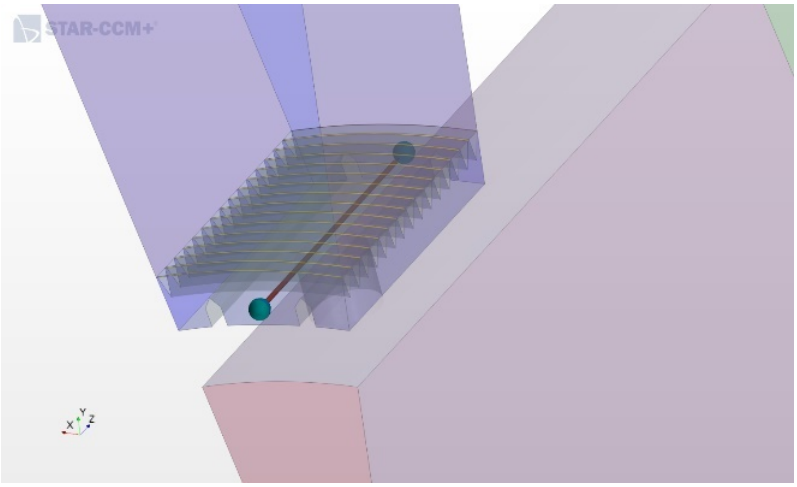

Figure 3.18: Axial probe in the annular region to collect pressure and velocity data.

Pressure drop and velocity fields at the probes locations are presented in Figures 3.20 and 3.21 having 4 PSDs. For the four sets of PSD data, it is found that there was no significant difference in the pressure drop and velocity fields at the probes locations (with various PSDs) specifically the one along the WWS and pipe (axial direction). Experimental work using the same sets of data (Table 3.2) reported less dependence of WWS on PSD than other sand screen devices while having moving particles[36]. No significant difference in the pressure drop and velocity fields at the probes locations having various PSDs suggests that, if we could get similar results while simulating moving particles in addition to the fluid, then we would confirm numerically that "WWS can be used for a wide range of PSDs". This finding will be important, since it potentially reduces the cost of SAGD projects. Additionally, operational risk could be decreased[36].

For the four sets of PSD data, it is found that there was no significant

difference in the pressure drop and velocity fields at the probes locations (with various PSDs) specifically the one along the WWS and pipe (axial direction). Experimental work using the same sets of data (Table 3.2) reported less dependence of WWS on PSD than other sand screen devices while having moving particles[36]. No significant difference in the pressure drop and velocity fields at the probes locations having various PSDs suggests that, if we could get similar results while simulating moving particles in addition to the fluid, then we would confirm numerically that "WWS can be used for a wide range of PSDs". This finding will be important, since it potentially reduces the cost of SAGD projects. Additionally, operational risk could be decreased[36].

In the following, pressure and velocity comparisons for 4 PSD data sets are presented on the probe passing through the whole domain in radial direction (see Figure 3.20 and 3.21). Looking at the pressure and velocity plots, there is no difference between four case studies since there is no moving particles. The results confirm that having various PSDs and no moving particles, PSD will not affect the flow in WWS, annulus, orifice and pipe. Since the permeability is high for these four PSDs, the pressure drop is expected to be small as it is. Mahdi et all[37] showed that in case of slotted liner, which is another type of sand screen device, the pressure drop occurred all in flow concentration region above the slot. That flow contraction region is much smaller in WWS, so the pressure drop is accordingly smaller.

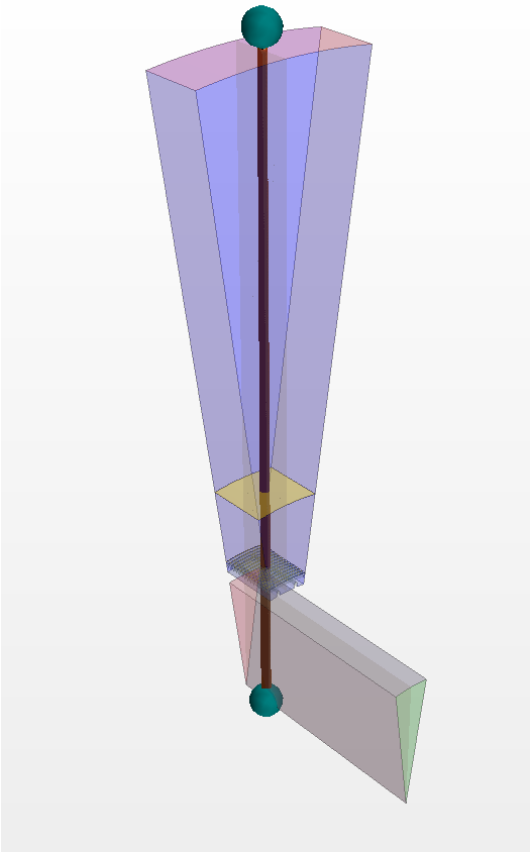

Figure 3.19: Radial probe through the whole domain to collect pressure and velocity data.

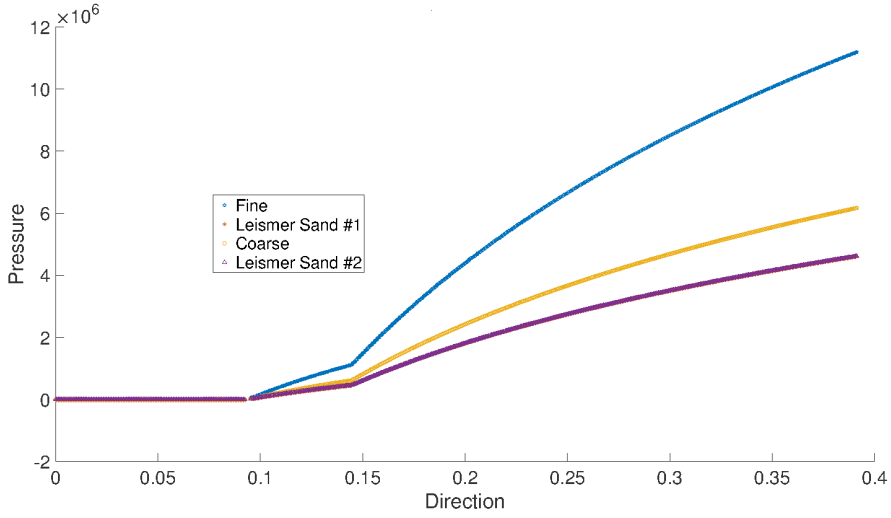

Figure 3.20: Pressure on radial probe through the whole domain for 4 PSDs.

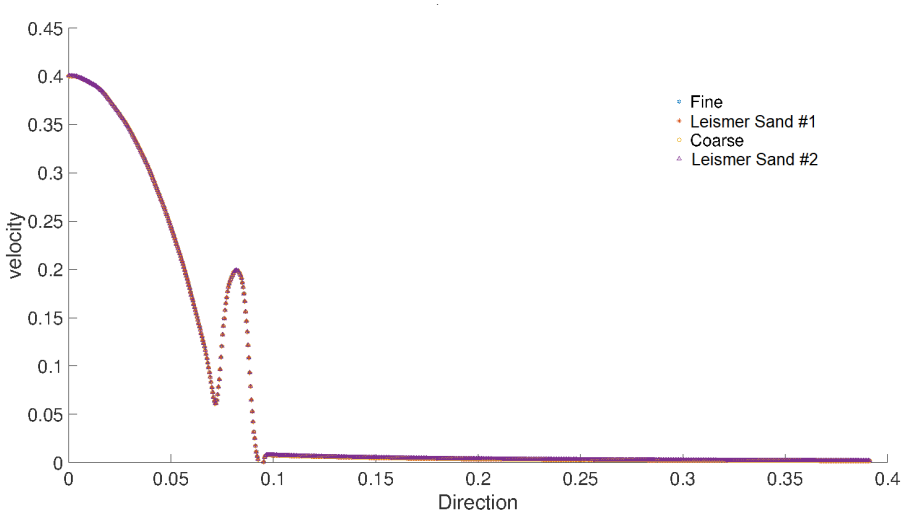

Figure 3.21: Velocity magnitude on radial probe through the whole domain for 4 PSDs.

3.2 Summary

A comparative study of the coupled porous media-WWS model was conducted on "fine" and "coarse" oil sands using conditions that simulates SAGD production well with CFD. Analysis of the pressure and velocity fields along the WWS and pipe confirm that having a single-phase flow of bitumen, flow in WWS is showing no dependence on the particle size distribution in porous media. This result confirms that having various PSDs and no moving particles, PSD will not affect the flow in WWS, annulus, orifice and pipe. Also, it is observed that the pressure drop is small from porous media to WWS, annulus, orifice and finally pipe since flow contraction region is small in WWS and causes lower pressure drop. The novelty of the present work is the analysis of the dependence of the flow in WWS to PSD using CFD.

The calculations conducted in the previous sections of this chapter could be considered as the validation for the CFD model. With no moving particles in porous media, it was expected that no pressure and velocity difference must be seen in the WWS, annulus and pipe as obtained by simulations. Also, mesh independence study was applied which resulted in a verified model. The flow simulation was also conducted on the full-domain of WWS as presented in Figures 3.23 and 3.22. 987638 cells generated by polyhedral mesh for the WWS full domain, annulus and pipe. Velocity field is presented in WWS, Figure 3.23, resulted by CFD simulation of single phase flow of oil in the WWS full domain, annulus, orifice and pipe.

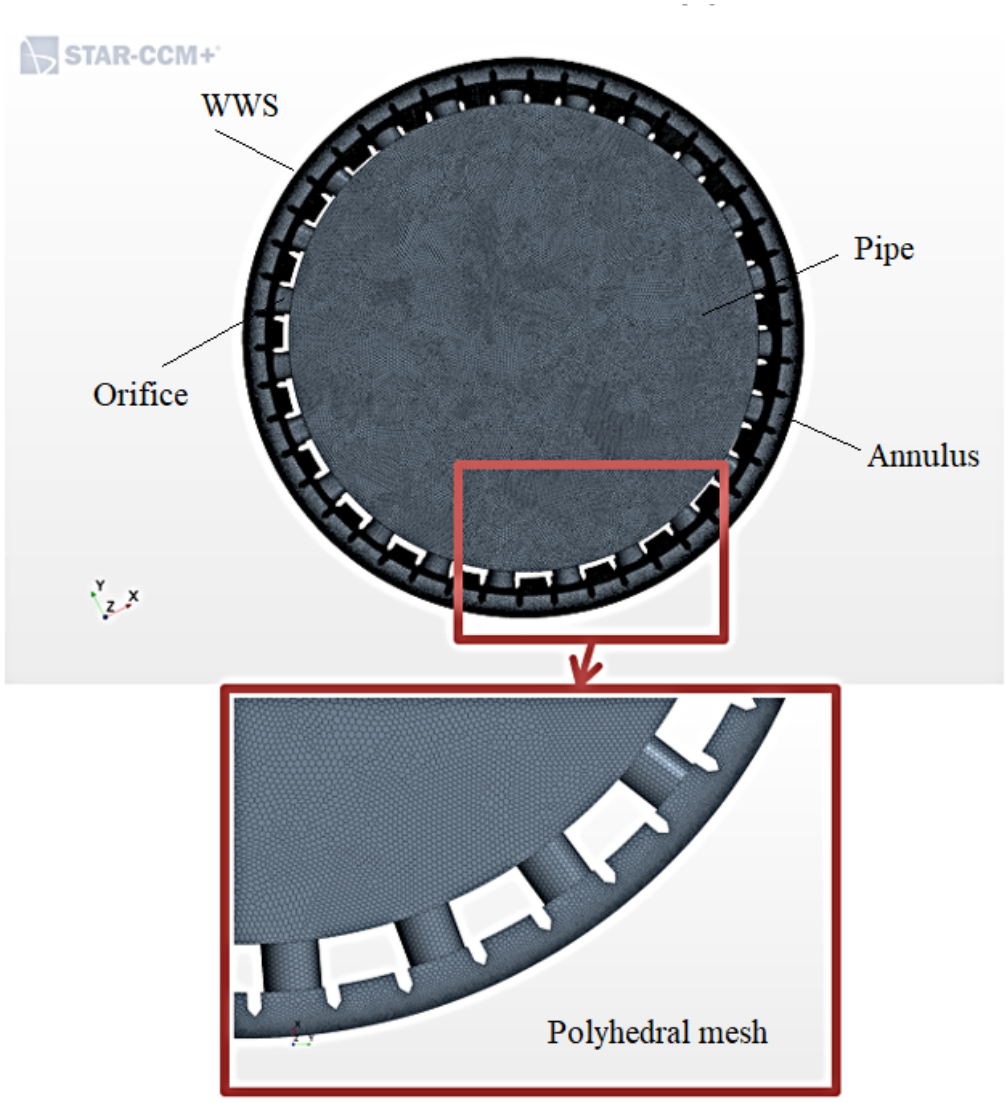

Figure 3.22: Polyhedral mesh for the WWS full domain, annulus, orifice and pipe: 987638 cells.

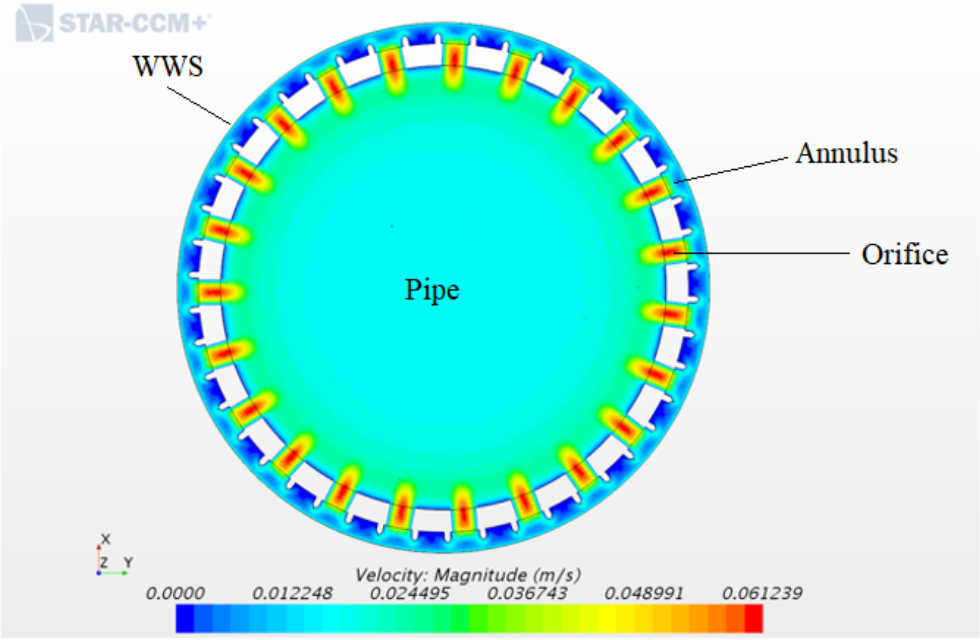

Figure 3.23: Velocity in WWS resulted by fluid flow simulation for the WWS full domain, annulus, orifice and pipe.

3.3 Single and Tandem Particles

3.3.1 Dimensionless Numbers for Particulate Flow Study

Prior to solving problems, it is worth mentioning the two main dimensionless numbers applied to study particulate flow. First is the Reynolds number that is defined separately for dispersed phase (particles) as well as continuous phase and the second one is Stokes' number.

$$Re_p = \frac{\rho_f \, |\boldsymbol{V}_f - \boldsymbol{V}_p| \, D_d}{\mu_c} \tag{3.5}$$

$$Re_f = \frac{\rho_f \boldsymbol{V}_f L}{\mu_c} \tag{3.6}$$

$$St = \frac{(\rho_f - \rho_p) \mid \boldsymbol{V}_f - \boldsymbol{V}_p \mid D_d^2}{18\ \mu_c\ L} \tag{3.7}$$

Equations (3.5) and (3.6) present the particle and fluid Reynolds' number respectively and Equation (3.7) presents the Stokes' number. For large values of the Stokes' number, the trajectory of the particles is independent of the fluid. As the value of the Stokes reduces, the influence of the fluid on the particles' trajectory increases.

For the Stokes' number less than 1, the particles will follow the fluid streamlines closely. In the above equations, ρ_f is the fluid density and ρ_p is the dispersed phase (particle) density. $\boldsymbol{V}_f$ and $\boldsymbol{V}_p$ are velocity of the continuous phase and disperse phase respectively. μ_c is the continuous phase viscosity, D_p is particle diameter and L is the continuous phase characteristic length. At low Reynolds number (laminar flow regime), Reynolds' number and Drag coefficient are reversely proportional. Accordingly, the characteristic time of the particle is defined as:

$$t_0 = \frac{\rho_p\ d_p^2}{18\mu_f} \tag{3.8}$$

where ρ_p is particle density, d_p is particle diameter and μ_f is fluid dynamic viscosity.

A dimensionless time could be defined as follows:

$$t_{DL} = \frac{\rho_p \, d_p^3}{18 \mu_f t W} \tag{3.9}$$

where t is simulation time and W is slot width.

3.3.2 Spherical Particle - Fluid Interaction Validation

In this section, a CFD-DEM model was setup and tested using three classic flow problem. Single particle (spherical shape) settling in a Newtonian fluid was simulated and particle's terminal velocity resulted by CFD-DEM modeling was compared with the theoretical terminal velocity. A suspended (neutrally buoyant) particle was simulated by assigning same density for the particle and the fluid. Additionally, CFD-DEM model was validated by the problem of the settlement of two particles in a Newtonian fluid.

Problems Statement

There was a 3D tank filled with quiescent water that dimensions were 10 cm $\times$ 1 cm $\times$ 20 cm. Sand-like particles were injected in this tank to investigate the interaction between the particles and fluid. There are three scenarios defined to examine particle-fluid interaction as follows:

1. Obtaining single particle settlement velocity in the tank using a CFD-DEM model and comparing the result with the known solution from theory.

2. The second problem was suspending the single particle in problem 1. Having equal density for the continuous and dispersed phases, it is expected that the terminal velocity of the particle will be zero and the particle will become suspended.

3. Third problem was exploring the drag force of the two particles settling in tandem in the quiescent fluid.

The outcome of working on these three scenarios will be validation of the developed CFD-DEM model from the perspective of particle-fluid interaction.

Solution

All sides of the tank are no-slip walls. The velocity outlet boundary condition is assigned to the top face. Mesh is the hexahedral structured mesh. The particles are injected through a point injector. The unresolved coupling approach was used. Computational model was set as Table (3.2).

Water ($\mu_f = 8.8871 \times 10^{-4}$ Pa $\cdot$ s and $\rho_f = 997.561$ $\frac{\text{kg}}{\text{m}^3}$) and steel (density: 7800.0 $\frac{\text{kg}}{\text{m}^3}$) are applied to the fluid and solid phase models respectively. Here is the list of applied assumptions and the computational model setup:

- Fluid viscosity: constant (Newtonian fluid), 8.90×10^{-4} Pa $\cdot$ s
- Fluid density: constant (incompressible), 997 $\frac{\text{kg}}{\text{m}^3} y$
- Particles size: mono-dispersed (d_p= 0.0025 m)
- Particle density: constant, 7800 $\frac{\text{kg}}{\text{m}^3}$

Table 3.2: Computational Model Setup

	Setup
Continuous phase equations	Continuity and NS equations
Fluid phase boundary condition	Top face: velocity outlet
Fluid phase boundary condition	Other faces: no-slip wall
Fluid initial condition	Quiescent fluid
Discrete phase equations	Newton's 2nd law of motion (conservation of linear and angular momentum)
Particle boundary condition	No-slip wall
Particle initial condition	Velocity = 0.014 $\frac{\mathrm{m}}{\mathrm{s}}$
Coupling scale	Coarse Grid Unresolved
Coupling technique	Two-way coupling
Particle type	DEM particles, Spherical
Solid particle material	Glass (solid, sand-like)
Fluid material	Water (liquid)
Forces	Pressure gradient force that counts for the buoyancy
	Drag force
	Gravity
DEM model setting	Residence time for particles
	Track file to track the velocity of particles
	Lagrangian multiphase DEM
	Multiphase interaction
Grid	3D, Hexahedral
$\frac{\partial x}{\partial D_p}, \frac{\partial y}{\partial D_p}, \frac{\partial z}{\partial D_p}$	$\frac{1\ \mathrm{mm}}{0.2\ \mathrm{mm}} = 5$
Number of cells	$10 \times 100 \times 200 = 200000$
Fluid time discretization Scheme	Implicit unsteady
Temporal order of discretization	1st order
Fluid flow solver	Segregated flow
Velocity solver	Algebraic multigrid (AMG) linear solver
Pressure solver	AMG linear solver
Fluid equation of state	Constant density
Continuous phase	Viscous regime and laminar
CFD time-step	0.001 s
DEM time-step	0.01 s

Case 1: Single Particle Settlement Velocity A single particle was injected into the tank at an initial velocity of 0.014 $\frac{\mathrm{m}}{\mathrm{s}}$. It flowed down under the gravity, drag and buoyancy forces until it reached the terminal velocity, where the forces were at equilibrium. Reynolds number of the particle was 72. The simulated terminal velocity by CFD-DEM model was in good agreement with the particle terminal velocity obtained by theory that was obtained by balancing the gravity, buoyancy force and viscous force. The terminal velocity

obtained analytically was 0.02601 $\frac{\mathrm{m}}{\mathrm{s}}$.

Figure 3.24 presents the single particle terminal velocity simulated by CFD-DEM model and the one calculated by theory. The fluctuations in the velocity are due to the wake street behind the particle. Having Re = 72, it is expected to have a vortex shedding behind the falling particle in the fluid [98], [99].

The Strouhal number represents the ratio of inertial forces due to the local acceleration of the flow to the inertial forces due to the convective acceleration [100]. In Case 1 by the periodic motion of the wake behind the particle, the Strouhal number, $\mathrm{S_{tr}}$, is given by the following expression [100]:

$$\mathrm{S_{tr}} = \frac{fL}{U} = \frac{2fd_p}{U} \tag{3.10}$$

where f is the frequency of the flow oscillations ($\frac{1}{\mathrm{s}}$), L is the characteristic length (m) and U is particle velocity ($\frac{\mathrm{m}}{\mathrm{s}}$). In this case, $L = 2d_p = 0.005$ [98], $U = 0.02601\ \frac{\mathrm{m}}{\mathrm{s}}$ and $f = \frac{1}{0.2\ \mathrm{s}}$. The Strouhal number value calculated based on the assigned values is 0.9612 for the falling particle in the quiescent fluid.

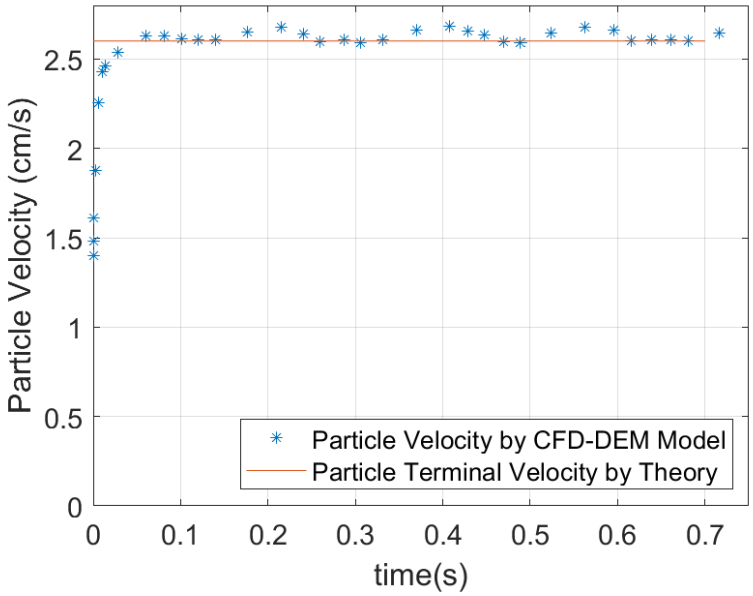

Figure 3.24: Particle terminal velocity: simulation and theory

Case 2: Suspending a Single Particle In the second test case, a single particle was suspended. Having equal density for the continuous and dispersed phases, it is expected that the terminal velocity of the particle will be zero and the particle will become suspended. This is also called neutrally buoyant condition. The particle is injected into the tank at 0.014 $\frac{\mathrm{m}}{\mathrm{s}}$ and its velocity reaches 7.7×10^{-7} $\frac{\mathrm{m}}{\mathrm{s}}$. The difference of this value with zero could be justified with round-off error. If the simulation runs for a longer time, it will even get closer to zero. Figure 3.25 shows the single particle settlement velocity simulated by CFD-DEM model. It confirms that having equal densities for the fluid and solid phases, the DEM model shows the particle is becoming suspended eventually which is equivalent to the zero-terminal velocity.

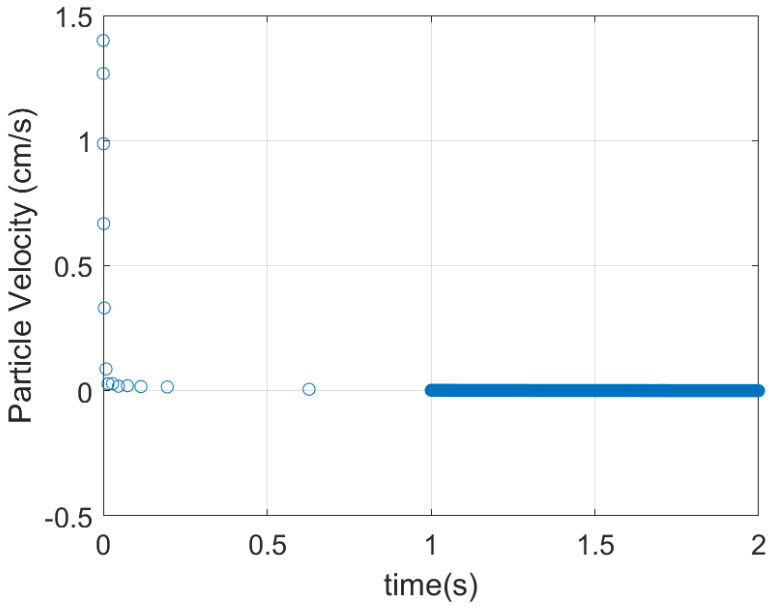

Figure 3.25: CFD-DEM simulation of a suspended particle

Case 3: Two Particles Settlement in Tandem The third problem is the case of settling two particles in the tank filled with quiescent water. The leading particle is injected and after one second, the trailing particle is injected. It is expected that the trailing particle accelerates and moves faster toward the leading particle. The reason for this acceleration is the smaller drag force that the trailing particle feels due to moving fluid behind the leading particle[101], which results in a lower relative velocity. The Reynolds number of the trailing particle is expected to be less than the leading particle as well, due to the lower relative velocity. Figure 3.26, 3.27, and 3.28 show the leading and trailing particles velocities, Reynolds numbers and drag forces, respectively. The CFD-DEM simulation confirms that:

1. The velocity of the trailing particle is increasing at a higher rate (acceler-

ating) and it approaches the leading particle, as expected.

2. Reynolds of the trailing particle is less than the leading particle due to the lower relative velocity between the continuous phase and the trailing particle.

3. The drag force on the trailing particle is less than the drag force on leading particle due to the lower relative velocity between the fluid and the trailing particle.

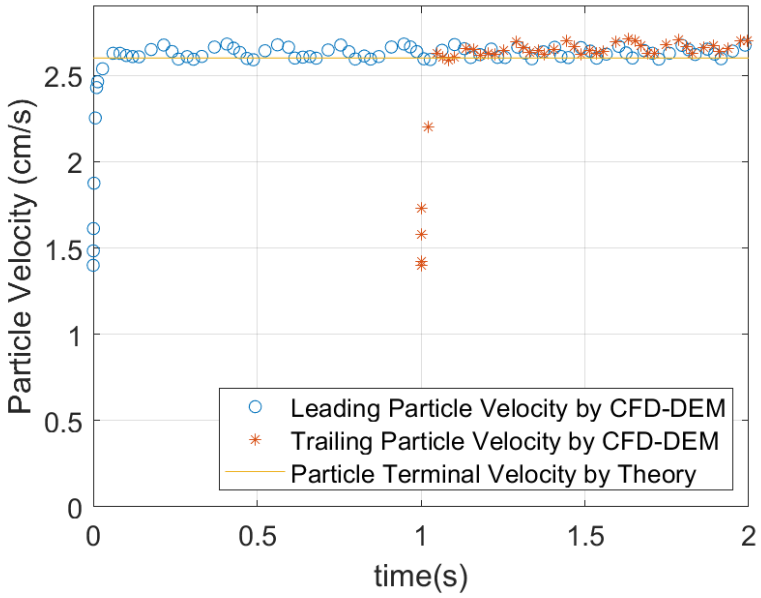

Figure 3.26: Leading and trailing particle velocity contours

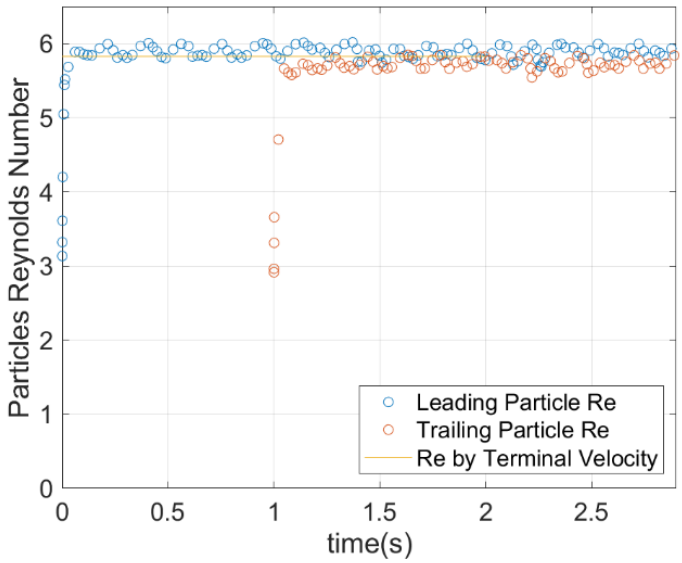

Figure 3.27: Leading and trailing particles Reynolds

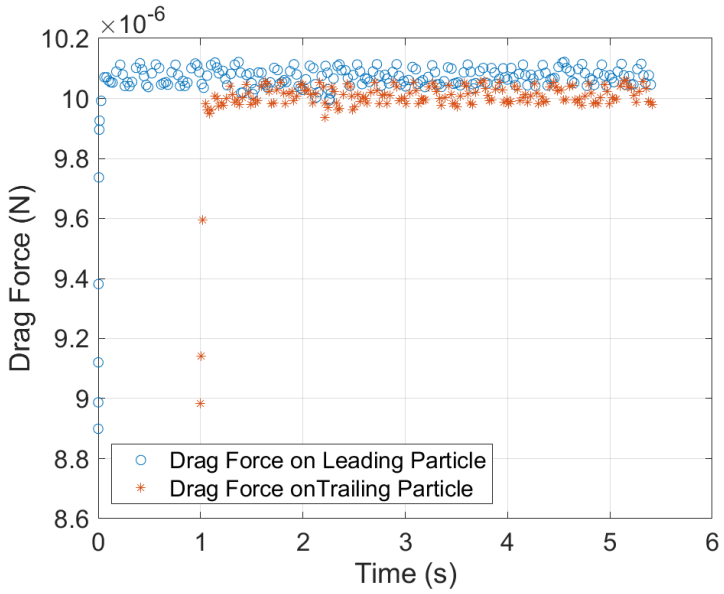

Figure 3.28: Drag force on the trailing particle is less than the leading particle as expected.

3.3.3 Spherical Particle-Wall Interaction Validation

In this section, the goal is to track the trajectory of a falling particle bouncing on a wall through CFD-DEM simulation and comparing the results the experiment.

Problem Statement

Considering the quiescent fluid of silicon oil in a tank made of glass, a steel sphere was falling in oil toward the bottom glass wall. The mass density of the steel sphere is $\rho_p = 7800\ \frac{\text{kg}}{\text{m}^3}$. The Young's modulus of elasticity E is 214×10^9 Pa and the Poisson's ratio v is 0.3. The mass density of silicon oil is $\rho_f = 970\ \frac{\text{kg}}{\text{m}^3}$ and the dynamic viscosity is $\mu = 0.1\ \text{Pa} \cdot \text{s}$ (at T = 20 °C). Size of the steel sphere was $d_p = 0.0053$ m, Re number was 30 and St number was 55. According to the available information, 3 problems will be solved as follows:

1. The falling particle trajectory is simulated with the CFD-DEM model and compared with the experiment[45].

2. Domain sensitivity analysis is performed.

3. Mesh sensitivity analysis is applied to compare the effect of the coupling resolution: smoothed unresolved (refined grid unresolved) vs. coarse grid unresolved.

The outcome of working on these three scenarios will be validation of the developed CFD-DEM model from the perspective of particle-wall interaction. Setting details is found in Table 3.3.

Table 3.3: Computational Model Setup

	Setup
Grid	3D, Hexahedral
Particle size	2.7 mm
Number of cells	300000
Fluid	Glycerol
Solid	Steel spheres
Fluid time discretization Scheme	Implicit unsteady
Temporal order of discretization	2nd order
Fluid flow solver	Segregated flow
Velocity solver	Algebraic multigrid (AMG) linear solver
Pressure solver	AMG linear solver
Fluid equation of state	Constant density
Continuous phase	Viscous regime and laminar
CFD time-step	0.001 s
DEM time-step	0.01 s

Figure 3.29 presents the non-dimensional distance between the bottom apex of the falling particle and the wall. It was obtained by dividing the distance between the bottom apex of the falling particle and the wall by particle radius. x-axis presents the non-dimensional time where U is terminal velocity of the particle and R is the radius of the particle. The solid line shows the experimental trajectory of the particle. Three domain sizes were tested. Results showed close agreement with the experiment which confirms that the model could capture the physics of the particle-wall interactions successfully.

The objective of the next presented study was to investigate the effect of the coupling resolution on the trajectory of the particle. The coarse grid unresolved case presents close trend to the experiment however the smoothed unresolved (refined grid unresolved) cases are much more accurate. The CFD-DEM model can successfully simulate the trajectory of the particle bouncing and its behavior before and after collision with the wall.

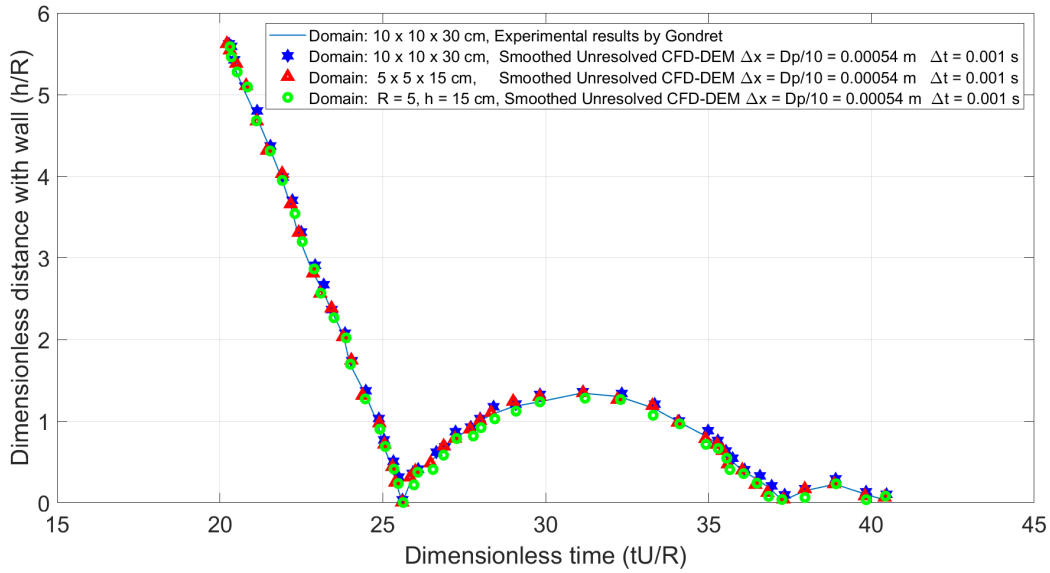

Figure 3.29: Domain sensitivity analysis

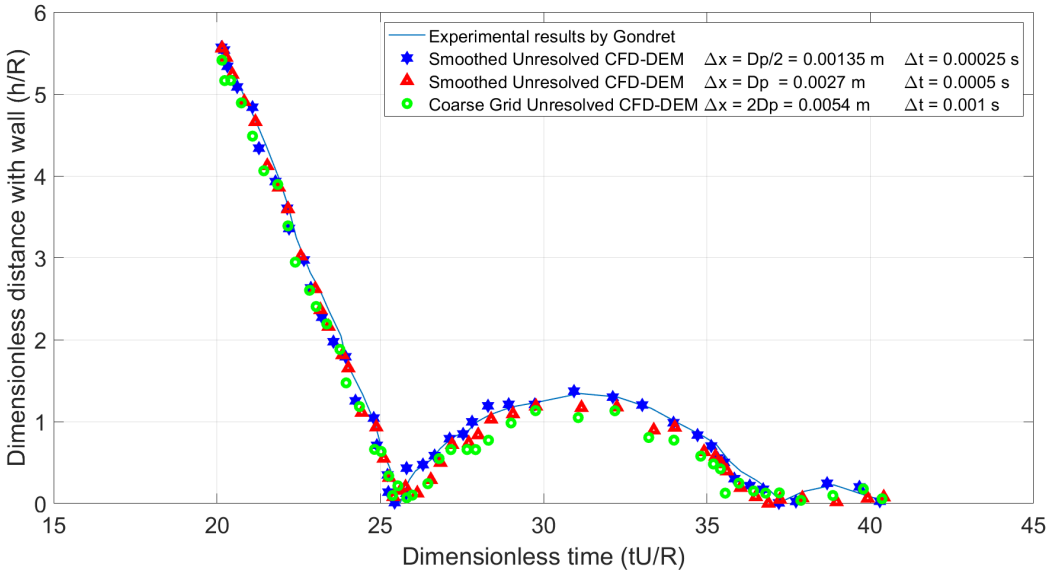

Figure 3.30: Mesh sensitivity analysis: smoothed grid unresolved vs coarse grid unresolved cases

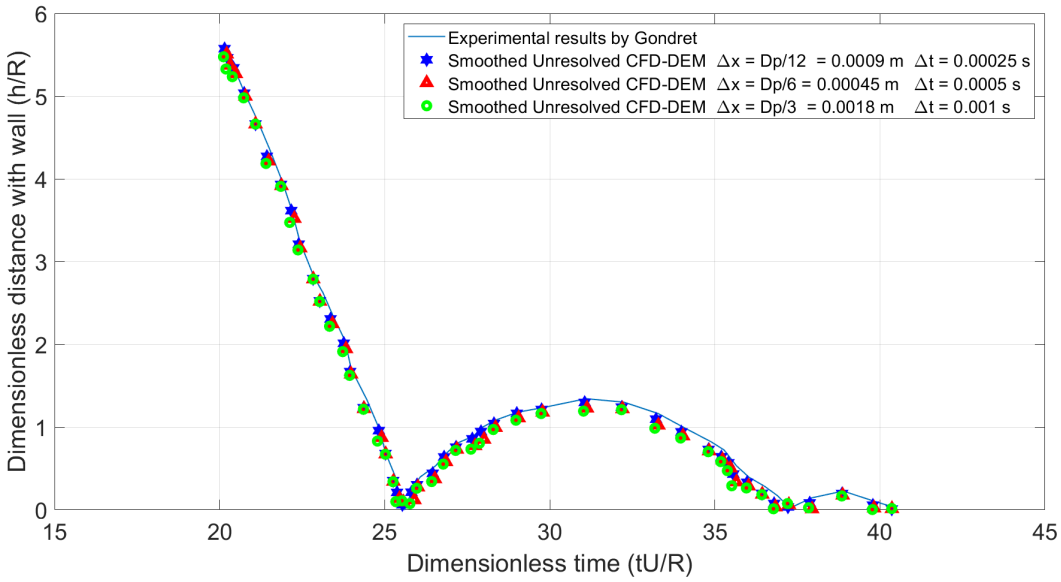

Figure 3.31: Mesh sensitivity analysis: smoothed unresolved (refined grid unresolved) cases

3.3.4 Validation of Spherical Particle-Particle Interaction

In this section, an experimental problem of drafting-kissing-tumbling of two particles[102], is replicated with the CFD-DEM model to investigate the capability of the model capturing the physics involved in particle-particle interaction.

Problem Statement

The benchmark problem considered here concerns the simulation of the motions and interaction of two falling identical balls in a vertical tank with square cross-section. The computational domain size was 0.1 cm $\times$ 0.1 cm $\times$ 0.4 cm. The diameter d of the two balls was $\frac{1}{6}$ mm. The initial translational and

angular velocities of the balls were zero. The density of the incompressible fluid was $\rho_f = 1000\ \frac{\text{kg}}{\text{m}^3}$ and the density of the balls was $\rho_s = 1140\ \frac{\text{kg}}{\text{m}^3}$. The fluid was quiescent. The boundary condition for the tank walls and balls was no-slip. Fluid had a viscosity of 0.01 poise (0.001 $\text{Pa} \cdot \text{s}$). The movement of the two balls was simulated and the distance between them was measured and compared with the DNS[102]. For verification and validation of the model, different time steps and grid spacing were tested to obtain the distance between the two particles at drafting, kissing, tumbling stages and then simulation results compared with the DNS results.

Results

Based on the DNS, two balls falling in the fluid were expected to go through three phases of drafting, kissing and tumbling according. The distance between the two particles were obtained by CFD-DEM simulation. Figure 3.32 presents these three phases predicted by the CFD-DEM model. Table 3.4 presents the model setup for this problem. Numerous cases with various time steps and grid spacing were tested and compared with the DNS solution that is the solid line in Figure 3.33. Figure 3.33 presents the simulated distance between the two particles as well as the DNS result. There is good agreement between the simulated results and the direct numerical simulation solution, the solid line[102].

The unresolved coupling was faster. With high performance computers, the smoothed unresolved (refined grid unresolved) approach with higher accuracy was the choice for the simulation of the particulate flow at micro-scale.

In this validation case, the effect of the coupling resolution (smoothed unresolved (refined grid unresolved/coarse grid unresolved)) also known as mesh sensitivity analysis, 1st and 2nd order time discretization schemes, 1st and 2nd order convection discretization schemes, various volume fractions of each cell in coupling stage as well as the effect of various CFD and DEM time steps were tested.

Table 3.4: Model Setup

	Setup
Grid	3D, Hexahedral
Domain size	0.1 cm $\times$ 0.1 cm $\times$ 0.4 cm
Particle size	$\frac{1}{6}$ mm = 167 μm
Fluid viscosity	0.01 poise
Fluid time discretization Scheme	Implicit unsteady
Convection discretization scheme	2nd order
Temporal order of discretization	2nd order
Fluid flow solver	Coupled flow
Velocity solver	Algebraic Multigrid (AMG) linear solver
Pressure solver	AMG linear solver
Fluid equation of state	Constant density
Continuous phase	Viscous regime and laminar
CFD time-step	Variable
DEM time-step	10 $\times$ CFD time-step
Coupling method	Two-way coupling
Forces active	Gravity, drag force, lift force, buoyancy

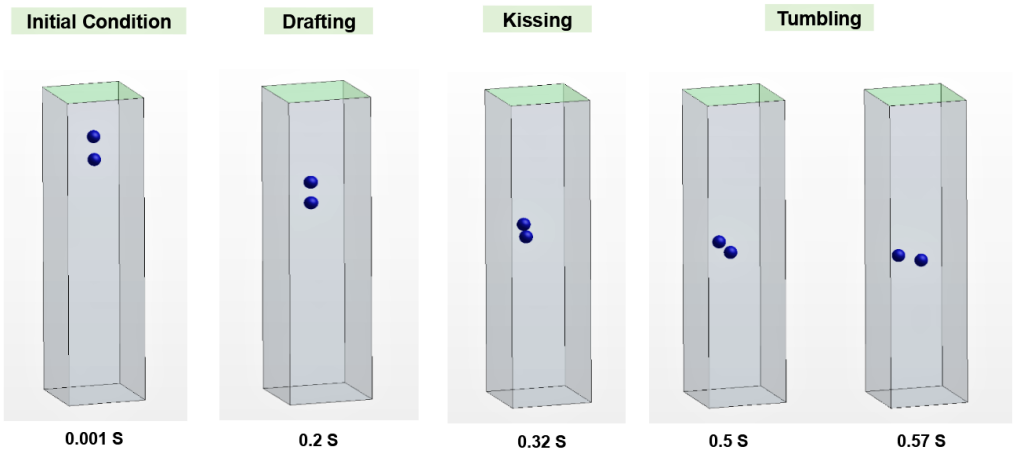

Figure 3.32: CFD-DEM model simulation output: predicated drafting, kissing and tumbling stages by simulation.

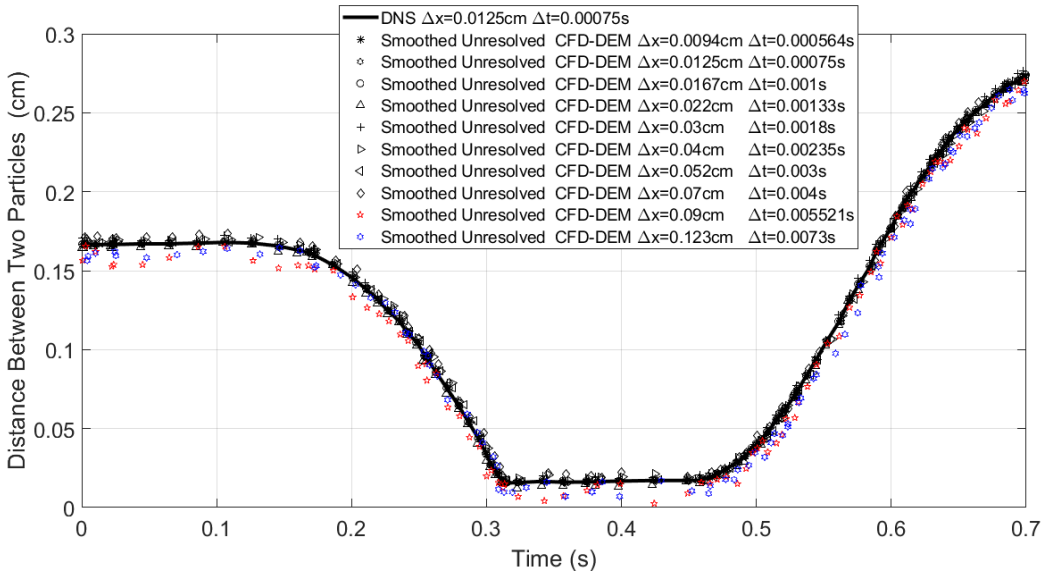

Figure 3.33: Smoothed unresolved (refined grid unresolved) cases: testing various time steps and grid spacing

According to the simulated cases presented in Figure 3.33, the predicated distance between the two particles in three stages of drafting-kissing-tumbling

was in good agreement with the DNS results. It confirmed the capability of CFD-DEM model of capturing the physics involved in the fluid-particle interaction and particle-particle interaction.

3.3.5 Polyhedral Particle-Fluid Interaction Validation

In the previous sections, the CFD-DEM model was validated for the spherical-shape particles. It was necessary to test the model credibility with non-spherical shape particles. The terminal velocity of a polyhedral-shape particle was simulated with the CFD-DEM model and compared to theory.

Terminal Velocity of Polyhedral Particle

In the following equations, it is shown how the terminal velocity of a non-spherical particle is calculated by theory[55].

$$u_* = u_t \left[\frac{\rho_f^2}{\mathbf{g}\ \mu(\rho_s - \rho_f)} \right]^{\frac{1}{3}} \tag{3.11}$$

$$d_* = d_{sph} \left[\frac{\mathbf{g}\ \rho_f(\rho_s - \rho_f)}{\mu^2} \right]^{\frac{1}{3}} \tag{3.12}$$

$$u_* = \left[\frac{18}{d_*^2} + \frac{(2.3348 - 1.7439\ \phi_2)}{d_*^{0.5}} \right]^{-1} \quad 0.5 \leq \phi_2 \leq 1 \tag{3.13}$$

u_* and d_* are the dimensionless terminal velocity and dimensionless particle diameter defined by Haider et al[55]. d_{sph} is the equivalent spherical diameter for non-spherical particle which is the diameter of the sphere which has same

volume as the non-spherical particle. ρ_s and ρ_f are the density of fluid and particle respectively and μ is fluid viscosity. ϕ_2 is particle sphericity that accounts for particle shape and is defined as:

$$\phi_2 = \frac{s}{S} \tag{3.14}$$

where s is the surface of a sphere having the same volume as the particle and S is the particle actual surface area.

First, d_* is calculated from equation (3.12). Having the value for d_*, u_* can be obtained from equation (3.13) and finally the terminal velocity, u_t, is calculated through equation (3.11). Terminal velocity of the polyhedral particle falling in a tank of quiescent water was calculated and compared to the theoretical estimate. The simulated terminal velocity was in agreement with the theory for various sizes of the spherical particle. It confirmed the capability of CFD-DEM model of capturing the physics involved in the fluid-particle interaction and particle-particle interaction. It confirmed the capability of CFD-DEM model of capturing the physics involved in the fluid-particle interaction having non-spherical particle.

Additionally, polyhedral particle-wall interaction has been investigated through investigation of the trajectory of the polyhedral particle bouncing on the wall. This problem will be described in the coming section.

3.4 Application of the CFD-DEM Model

Having a validated CFD-DEM model from the perspective of particle-fluid interaction, particle-wall interaction and particle-particle interaction, this model has been applied to solve problems with various degrees of complexities.

3.4.1 Investigation of Physics Involved in Particulate-Flow

Considering the quiescent fluid of silicon oil in a tank made of glass, a steel particle is falling in oil toward the bottom glass wall. The mass density of the steel sphere is $\rho_p = 7800 \ \frac{\text{kg}}{\text{m}^3}$. The Young's modulus of elasticity E is $214 \times 10^9 \ Pa$ and the Poisson's ratio $v = 0.3$. The mass density of silicon oil is $\rho_f = 970 \ \frac{\text{kg}}{\text{m}^3}$ and the dynamic viscosity is $\mu = 0.1 \ \text{Pa} \cdot \text{s}$ (at T = 20 °C). Diameter of the steel sphere is 0.0053 m. In Table 3.5, the CFD-DEM model setup is presented. In this problem referring to equations (3.7) and (3.5), $St = 30$ and $Re_p = 55$.

Table 3.5: Model Setup

	Setup
Grid	3D, Hexahedral
Fluid	Silicon oil
Particle	Steel sphere
Domain size	10 cm × 10 cm × 30 cm
Particle size	2.7 mm
Fluid time discretization Scheme	Implicit unsteady
Temporal order of discretization	2nd order
Fluid flow solver	Segregated flow
Velocity solver	Algebraic Multigrid (AMG) linear solver
Pressure solver	AMG linear solver
Fluid equation of state	Constant density
Continuous phase	Viscous regime and laminar
CFD time-step	0.001 s
DEM time-step	0.01 s
Coupling method	Two-way coupling
Forces active	Gravity, drag force, lift force, buoyancy

Effect of the Shape of the Particle on the Trajectory of the Particle

This problem was solved for 2 scenarios: a spherical particle and a polyhedral particle in similar conditions explained above. Tracking the trajectory of the particle bouncing on the wall and the difference between the trajectory of the spherical and polyhedral particle confirms that the shape of the particle affects the trajectory of the particle bouncing on a wall, Figure 3.34. In this simulation, characteristic length of the polyhedral particle, which was the longest dimension of the polyhedral particle, was assigned to be the same as the spherical particle diameter for comparison.

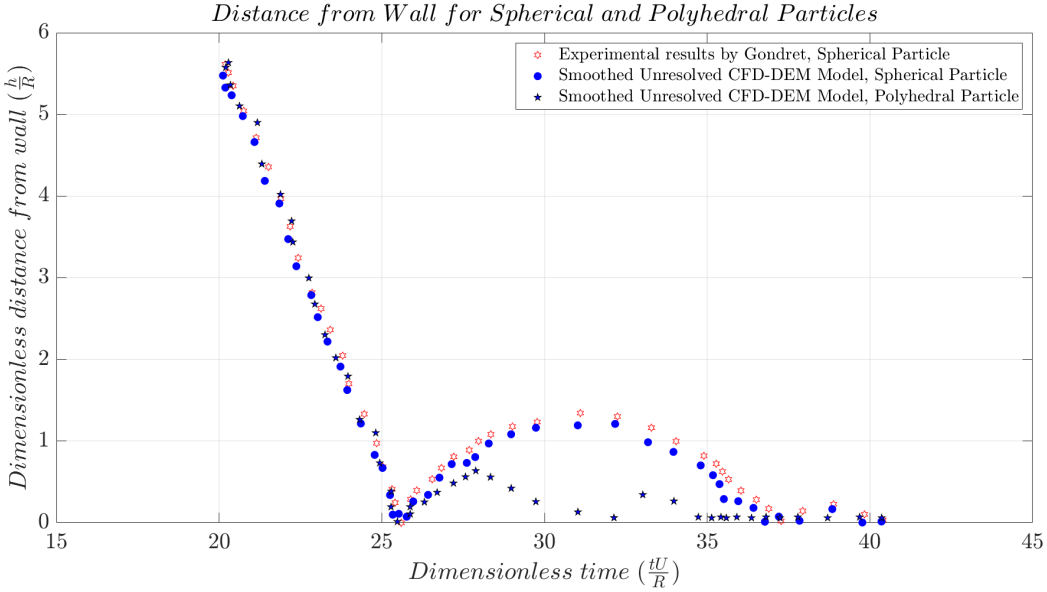

Figure 3.34: Trajectory of a spherical particle bouncing on a wall: plotting the distance from the bottom apex of the particle to wall versus time.

This difference was mainly visible after the particle hits the wall, Figure 3.34. The simulated result compared to experiment and the spherical particle trajectory is in agreement with the experimental trajectory. In addition, the terminal velocity of the polyhedral particle is in agreement with the theory.

Effect of the Changes in Viscous Drag Model on the Trajectory of a Particle Bouncing on a Wall

In this problem, 3 different drag models were applied in the CFD-DEM model: Gidapsow[86], Schiller-Naumann and Di Felice[5]. The simulated trajectory of the particle bouncing on the wall is different having the various drag models which directs the attention towards the importance of the drag model selection. Gidapsow drag model[86] had the closest results with the experimental

trajectory.

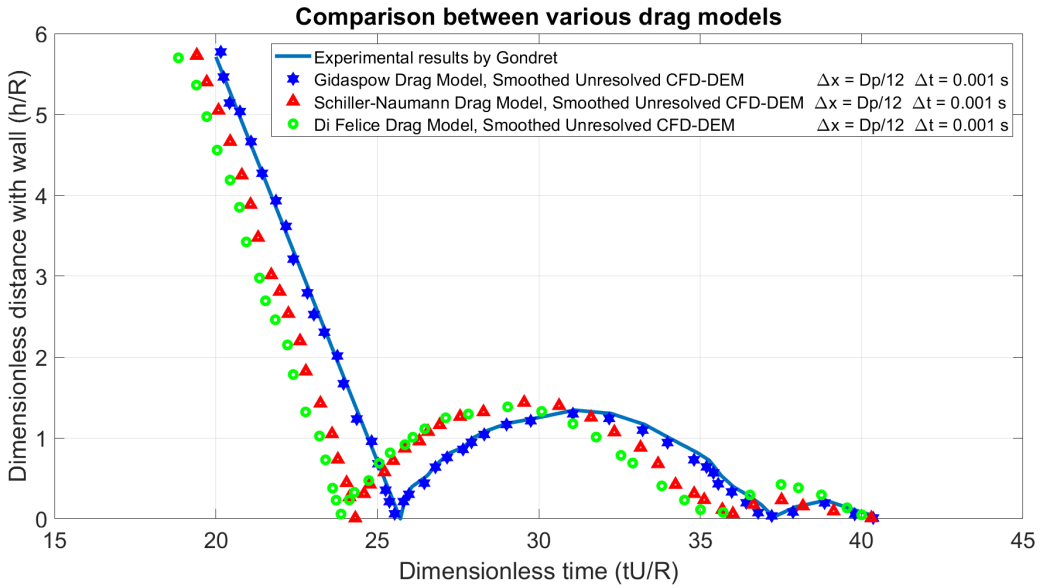

Figure 3.35: Trajectory of a spherical particle bouncing on the wall: the effect of various drag models (plotting particle distance from wall versus time)

Calculating the Restitution Coefficient out of the Developed CFD-DEM Simulation

The developed CFD-DEM model was applied to predict the restitution coefficient in 4 scenarios having different Stokes numbers.

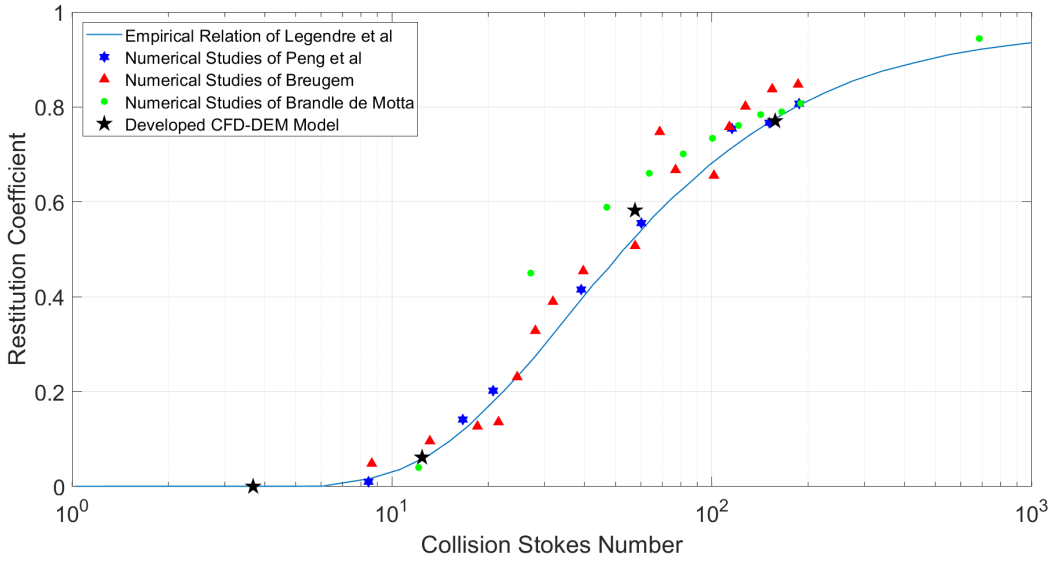

Figure 3.36: The wet restitution coefficients during a particle–wall contact collision as a function of collision Stokes number. The results were compared to the numerical studies of[10],[11] and[12], and the empirical relation of[13].

To calculate the restitution coefficient for each Stokes number, the velocity of the particle falling was tracked and the ratio of the simulated velocity before and after the collision resulted in the simulated restitution coefficient.

The wet restitution coefficients during a particle–wall contact collision as a function of collision Stokes number in Figure 3.36. The results were compared to the numerical studies of[10],[11] and[12], and the empirical relation of[13]. y-axis shows the restitution coefficient and x-axis shows the Stokes number calculated at the time of the particle collision with the surface.

The solid particle has its fixed restitution coefficient of 0.9, which is the value that applies for zero-way coupled cases (natural damping of the solid, which applies to high collision Stokes values and cases of no-fluid or vacuum). At

lower values of the collision Stokes number, the simulated restitution coefficient would remain the same as the solid restitution coefficient, if the lubrication and other surface interaction forces were not included. And if they were included, but were poorly calculated, then the simulated restitution coefficient would not match the experiment. Therefore, STAR-CCM+ is accounting for the lubrication and other surface interaction forces to a good level of accuracy.

3.5 Conclusions

In this chapter, the CFD-DEM model was verified and validated. Here is the summary of the problems solved to validate the CFD-DEM model:

1. Particle-fluid interaction validation: single particle terminal velocity, single particle suspension, two particles falling in tandem.

2. Particle-particle interaction validation by simulating the drafting-kissing-tumbling problem and comparison with DNS.

3. Particle-wall interaction validation by simulating the particle bouncing on a wall.

In addition, mesh sensitivity analysis was completed by comparing numerous smoothed unresolved (refined grid unresolved) and unresolved cases. It was confirmed that while the unresolved cases follow the trend of the experimental results, the smoothed unresolved cases are in better agreement with the experimental results at the scale of this research, micro-scale.

The verification and validation of this model has provided an understanding of simulating the particle-particle interaction, particle-wall interaction and particle fluid interaction considering the spherical and polyhedral shape of the particle.

The main contribution of this research work is outlining a work-flow for CFD-DEM model validation as well as developing a model that works with spherical and polyhedral shapes of the particle. The developed and validated CFD-DEM model provides a platform to explore particulate flow in sand screen devices in oil wells. An interesting problem in sand filters arching phenomenon is under investigation using this CFD-DEM model and the results will be discussed in the next chapters.

With the CFD-DEM model, it is possible to give a scientific description of the sand-retention mechanisms, most importantly sand-arching and advancing this knowledge could be employed to improve the design of the sand filter by the industry partner of this work.

3.5.1 Recommendations on Model Setup for Particulate-Flow Study

This research provides a unique opportunity to advance the understanding of multi-particle bridge formation, stabilization, destruction and reformation at filter opening by numerical modeling of particulate flow at filter opening involving hundreds of particles. This study aims to offer insight into how bridge performs under transient conditions. Advancing the findings will help industry

partner of the research make better decisions about filter selection and design while dealing with common transient well-bore phenomenon.

The first phase of this work involved setting up a numerical model and conducting a rigorous verification and validation of the model to assure that the model was predictive from the perspective of particle-particle, particle-wall and particle-fluid interactions.

Literature was investigated to apply the right particulate-flow modeling approach at micro-scale considering the computational resources. It was found that by the CFD-DEM model, the collision of hundreds of particles and the inter-particle forces could be simulated. The CFD-DEM models were set up and validated from the perspectives of particle-particle, particle-wall and particle-fluid interactions with the benchmark problems as well as the available experimental work from the collaborating labs and literature.

Following the verification (mesh independence analysis) and validation practices, a list of best practices was achieved to set up the model and study particulate flow at filter opening as follows:

1. A mesh should be designed in a way that gives adequate resolution in regions where spatial gradients are high, such as slot entrance. Considering the computational cost and accuracy, the best practices mesh-resolution for a steady state particulate flow case was achieved by smoothed unresolved coupling where the size of the particle was at least as twice as the mesh size. Also, mesh-resolution for a transient particulate flow case was achieved by smoothed unresolved coupling where the size of the particle was at least five times larger than the mesh size. The quality of

the robust simulation model guaranteed by grid independence and error estimation.

2. Any recirculation across a flow boundary should be avoided.

3. The mesh should be aligned with the flow to improve the accuracy and increase the rate of convergence.

4. Grid sensitivity study with two or more meshes must be applied.

5. The unsteady simulation had to start from a converged steady solution and then convert to transient.

6. Second order time discretization was preferred, and a spatial discretization that was based on second-order upwind differencing scheme.

7. A default solver setting (velocity URF = 0.8, pressure URF = 0.2, and of iterations per time step = 5) works well rather than the regular setting which was slower (velocity URF = 0.7, pressure URF = 0.7 , number of iterations per time step = 4 to 10) and the aggressive setting (velocity URF = 1, pressure URF = 0.9 , number of iterations per time step = 3).

8. The segregated solver was preferred to the coupled solver for transient cases considering the accuracy and the computational cost.

9. Freezing the solvers helped initial simulation stability, computational efficiency, and reducing total run time specifically early in the simulation. Convergence issues could arise because of the lack of a good physical initial condition for transient simulations.

10. The preferred boundary condition combination was to use no-slip wall and symmetry for the domain boundaries.

11. The preferred mesh is hexahedral rather than polyhedral considering accuracy and computational cost.

12. A velocity inlet boundary condition type for the upstream, and a pressure outlet boundary condition for the downstream boundary were preferred.

13. It was revealed that Young modulus lower than the actual one could reduce simulation time as DEM time-step was dependent on Young modulus. A reduction up to three order of magnitudes could be applied with sensitivity analysis.

14. Hertz-Mindlin contact model could predict well how particles interact during the collision.

15. The boundary condition is set at continuum level by default and had to setup for each individual boundary of particles.

16. Maximum porosity could be specified as limit after which injection of new particles is stopped. This feature could help building the porous regions with particles.

17. Two-way coupling is recommended to study retention mechanisms where each phase is affected by the other phase for example if drag force is included in the simulation, a momentum source is added to the continuous

phase. The reason for using two-way coupling is all the interactions involved in the collision are included in the simulation.

18. Volume fraction of disperse phase in the continuous phase is dependent on cell size where maximum volume fraction is 1 in case of having larger particles than cells. Solution could be unstable if the disperse phase produces high sources of momentum. Sources could be smeared/smoothed in more cells through DEM solver to avoid instability. It was achieved that the maximum volume fraction specified in the simulations in case of smoothed unresolved coupling was 0.98. Using 1 resulted in the simulations instability.

19. The CFD-DEM model by applying the soft-sphere model was predictive. In the the soft-sphere model, particles could overlap but not deform. The soft-sphere formulation is based on the contact forces that are established during a contact between particles[6]. In this model, contact force is proportional to the overlap and multiple contacts are allowed at the same time.

Chapter 4

Investigation of Multi-Particle Arch Formation

In this chapter, the multi-particle arching phenomenon, the break down of the conditions and parameters involved in multi-particle arching and the bridge response under transient condition, which are the main goal of this research project, will be discussed. This chapter starts with an investigation of the sand-retention mechanisms, specifically, with slurry flow on top of the slot. Then, the multi-particle arching phenomenon with a packed-bed of sand particles on top of the slot is discussed. Various parameters and conditions studied to support multi-particle arch formation, stabilization, destruction and reformation. They are listed as follows:

1. Investigation of the environment on top of the slot: porous region and empty gap between the filter opening and the reservoir.

2. Investigation of the effect of the particle size: considering uniform distri-

bution and non-uniform distribution.

3. Investigation of the effect of physical forces: drag, buoyancy, gravity, virtual mass, cohesive force, lift forces, and interaction forces.

4. Investigation of the effect of the fluid: air, water, and Athabasca oil.

5. Investigation of the effect of slot length and width.

6. Investigation of the effect of the particle concentration.

7. Investigation of the effect of the particle shape: spherical and polyhedral.

8. Investigation of the effect of slot geometry: straight, WWS, keystone and seamed slot.

4.1 Sand-Retention Mechanisms at the Openings of the Sand Filters

Simulation of the sand-retention mechanisms (surface deposition, size exclusion, sequential arching and multi-particle arching) and the investigation of the factors that affect these mechanisms will be helpful to enhance the criteria for the sand screen selection and sand screen design in oil industry [18], [50], [51]. Sand-retention mechanisms can be explored through simulation of the particulate flow around the sand screen device as reviewed in chapter 1. Sand screens act as an obstacle to prevent the solid particles from flowing into the oil production well and they rely on four mentioned mechanisms.

Among the four mechanisms, multi-particle arching is an efficient sand-retention mechanism that is the main interest of this research. In the next section of this chapter, various slurry and packed-bed cases are discussed, and the sand-retention mechanisms with the focus on multi-particle arching phenomenon are explored.

4.1.1 Various Slots: Straight, Keystone, WWS, Seamed Slot

There are four types of sand-filter slots that were examined in this research: straight, keystone, wire-wrapped screen (WWS) and seamed slot (Figure 4.2). The geometry of these slots are different and those differences could affect their sand-retention perfomance.

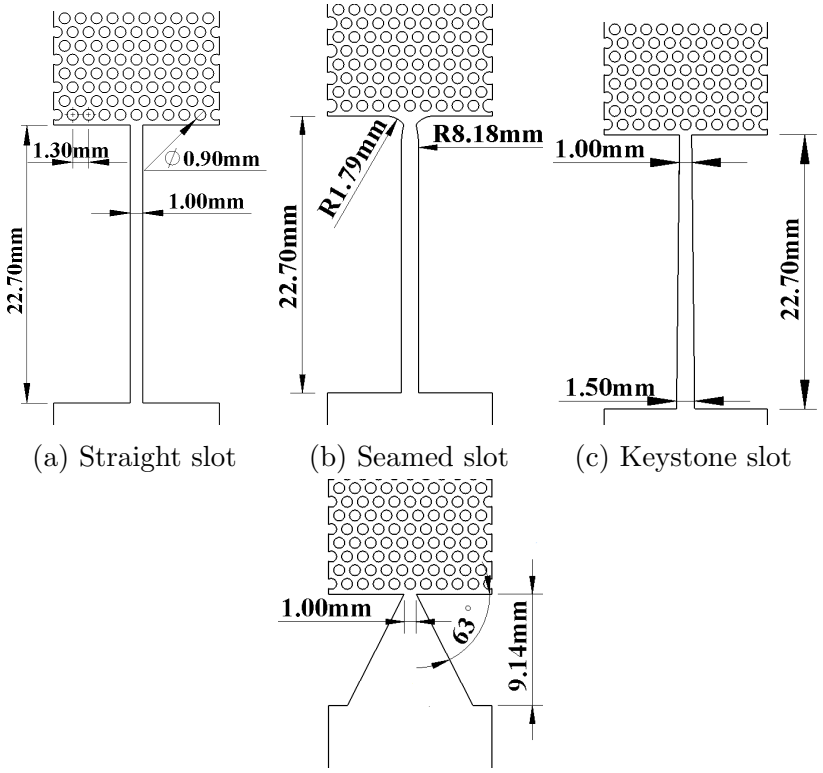

(a) Straight slot (b) Seamed slot (c) Keystone slot

(d) WWS slot

Figure 4.2: Various slot geometries with porous media on top

Figure 4.3 shows the velocity distribution of single phase flow of oil in a single opening of a seamed slot. The inlet velocity was chosen to correspond to the flow through a single slot at a typical production rate for SAGD. As a result, the fluid velocity is very small and the maximum fluid velocity was observed in the middle of the slot close to the slot opening. At the slot opening, the area for fluid entrance reduced, and consequently, the velocity of the fluid increased.

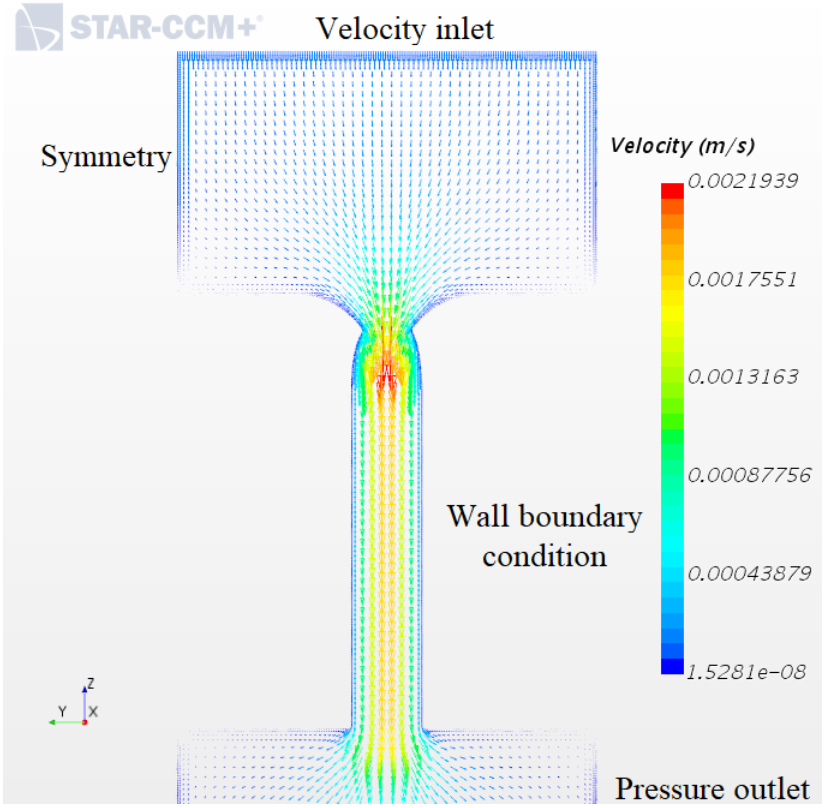

Figure 4.3: Velocity distribution of single phase flow of oil in a seamed slot.

4.2 Slurry Cases

A slurry is a diluted mixture of a fluid and solids denser than the fluid suspended in the fluid phase[103]. The size of solid particles may vary from 1 μm up to hundreds of millimeters. In this case, the solid particles are sand particles at the scale of 200 μm. The fluid phase is the carrier phase transporting solids. In slurry flow, solid phase or dispersed phase could have various concentrations of particles resulting in various slurry concentrations. The slurry concentrations normally range from 6% to 40% for sand slurries[103].

Problem Statement The slurry flow cases considered here consist of Athabasca oil and sand particles on top of a single filter opening. The objective was to investigate the sand-retention mechanisms that occurred with the slurry flow to see if the multi-particle arching occurs. In this section, various parameters and conditions of the slurry flow were tested to get knowledge of retention mechanisms. The geometries and dimensions of the simulation domain, shown in Figure 4.2, were chosen to replicate the shapes of a slurry flow experiment[1] for qualitative comparison. Table 4.1 presents the computational and mathematical setup of the problem.

Table 4.1: Mathematical and computational model setup for slurry cases

	Setup
Continuous phase equations	Continuity and NS equations
Fluid phase boundary condition	Top face: fluid velocity inlet = 0.001 $\frac{\text{m}}{\text{s}}$
Fluid phase boundary condition	Other faces: no-slip wall
Fluid initial condition	Quiescent
Discrete phase equations	Newton's 2nd law of motion (conservation of linear and angular momentum)
Particle boundary condition	No-slip wall
Particle initial condition (at t = 0)	Terminal velocity = 0.0065 $\frac{\text{m}}{\text{s}}$
Coupling scale	Smoothed Unresolved
Coupling technique	Two-way coupling
Particle type	DEM particles, Spherical
Solid particle material	Glass (solid, sand-like)
Fluid material	Athabasca oil
Forces	Pressure gradient force (counts for the buoyancy) Drag force Gravity Interaction forces Lift forces Virtual mass force
DEM model setting	Residence time for particles Track velocity and locations of particles Lagrangian multiphase DEM Multiphase interaction
Grid	3D, Hexahedral
Particle size	$d_p = 200$ μm
Fluid	Athabasca oil ($\mu_f = 0.0136$ Pa $\cdot$ s and $\rho_f = 915.2$ $\frac{\text{kg}}{\text{m}^3}$)
Solid	Glass ($\rho = 2800.0$ $\frac{\text{kg}}{\text{m}^3}$, Poisson's ratio = 0.45, Young's modulus = 517000.0 Pa)
Fluid time discretization Scheme	Implicit unsteady
Temporal order of discretization	2nd order
Fluid flow solver	Segregated flow
Velocity solver	Algebraic multigrid (AMG) linear solver
Pressure solver	AMG linear solver
Fluid equation of state	Constant density
Continuous phase	Viscous regime and laminar (at slot $Re_f = 0.0672, Re_p = 0.106, St = 0.004$)
CFD time-step	0.01 s
DEM time-step	0.1 s

4.2.1 Slurry Cases without and with Porous Media

A structured porous region on top of the slot could have affected particles' interactions and consequently the sand-retention mechanisms. In order to observe the occurrence of various retention mechanisms, one case consists of an open flow area in front of the slot and the other case consists of a structured porous medium with fixed circular obstacles. This case condition and simulation

is presented in Table 4.1. Figure 4.5 presents the two case studies of slurry flow in a single opening of a sand screen device (wire-wrapped screens or WWS) with and without porous media on top.

It was obvious from the simulations that the concentration of the particles are too diluted to result in multi-particle arch formation at the slot.

Here is a list of observations by simulating cases with and without the porous region:

1. A porous region on top of the slot reduced the number of particles passing through the slot in the specified time compared with the case without the porous region.

2. Surface deposition and size exclusion were observed.

3. There was no formation of multi-particle arch in either case.

4.2.2 Slurry Cases with Various Concentration of Particles

Slurry concentrations is the ratio of volume of solids and total volume of the mixture, usually given in percentage. In these simulations, a range of sand particles' concentration (10%, 20%, 25%, 30%, 35%, 36%, 38%, 40%) was tested to investigate the effect of concentration on sand-retention mechanisms, as summarized in Table 4.2. Figures 4.6 shows two sand-retention mechanisms that were observed: surface deposition and size exclusion in this case.

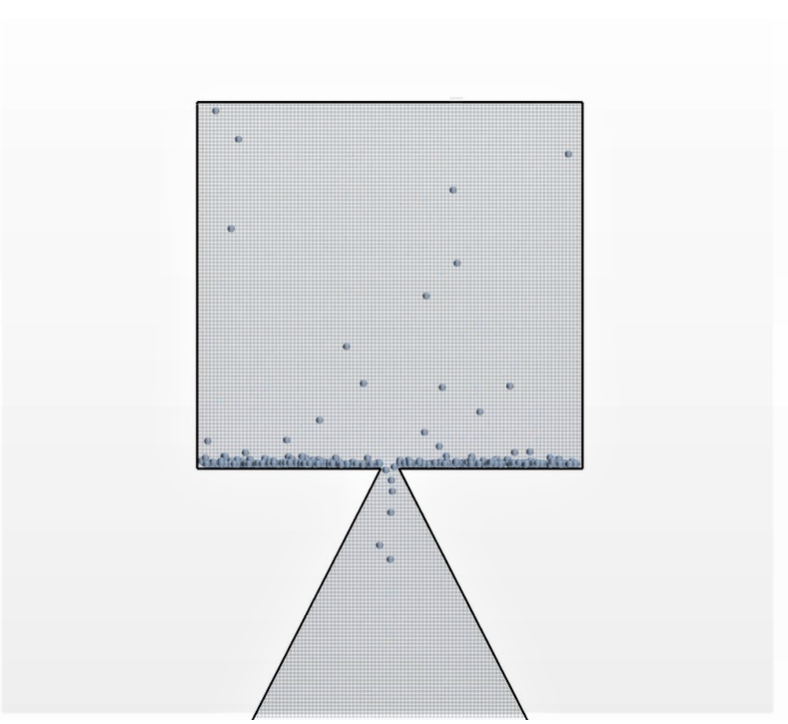

(a) Without porous media

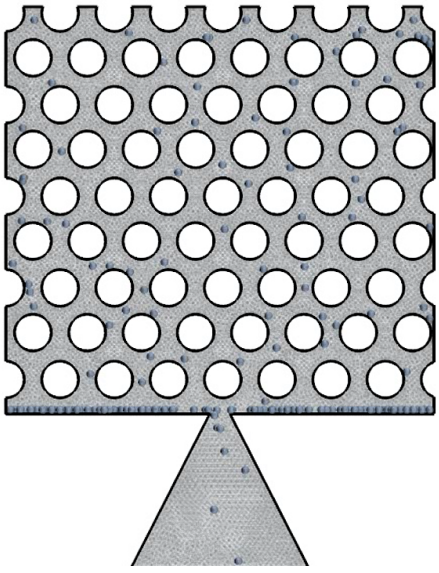

(b) With porous media

Figure 4.5: Slurry flow on a filter opening without and with porous media on top of the slot.

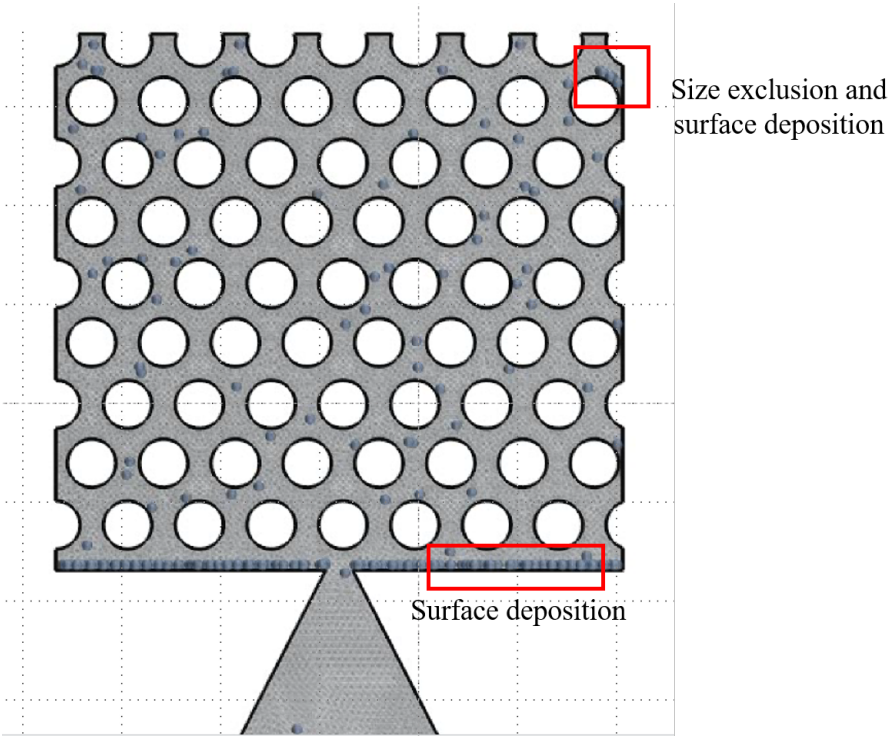

Figure 4.6: Two sand-retention mechanisms were observed: surface deposition and size exclusion in this case with slurry flow of spherical particles and porous media on top of the slot.

Table 4.2: Cumulative numbers of particles that passed the slot during 1.1 s interval (11 DEM time steps): slurry cases with various particle concentrations

Time	**10**%	**20**%	**30**%	**40**%
2-3.1 s	2	4	7	11
4.3-5.4 s	5	9	14	13
9.7-10.8 s	3	6	9	9
15.5-16.6 s	3	5	6	8

The following findings were observed from the simulated scenarios:

1. The number of particles passing through the slot within the time specified (11 DEM time steps = 1.1 s) initially increased at the beginning of the flow and then reduced when particles started to deposit, as shown in Table 4.2.

2. Surface deposition was clearly observed, see Figure 4.6. Size exclusion mechanism occurred at the pores in porous media as the size of the particles was larger than the pore size at some locations.

3. Despite various concentrations of particles within the range for slurry flow, the multi-particle arch and sequential arching did not occur in any case.

4.2.3 Slurry Cases with and without Fluid Flow

To assess the effect of the fluid flow on the retention mechanisms, several simulation scenarios with flow of different fluids were conducted with and without fluid (i.e. without any fluid interaction, as in vacuum). Three fluids

were tested: air ($\mu_f = 1.849 \times 10^{-5}$ Pa $\cdot$ s and $\rho_f = 1.184$ $\frac{\text{kg}}{\text{m}^3}$), Athabasca oil ($\mu_f = 0.0136$ Pa $\cdot$ s and $\rho_f = 915.2$ $\frac{\text{kg}}{\text{m}^3}$) and water ($\mu_f = 8.8871 \times 10^{-4}$ Pa $\cdot$ s and $\rho_f = 997.561$ $\frac{\text{kg}}{\text{m}^3}$).

In the first case, the fluid solver was stopped, also called frozen or no-fluid case to remove the fluid stress, normal and shear, on particles, and to investigate the occurrence of the sand-retention mechanisms in the extreme case of no fluid as in vacuum. The concentration of the slurry flow was 35% for these scenarios. Problem setup is presented in Tables 4.1 and the corresponding non-dimensional numbers are listed in Table 4.3. The study was conducted on WWS with and without porous media on top of the slot.

Table 4.3: Reynolds and Stokes numbers as well as particle terminal velocity in case of the various fluids

	air	**water**	**Athabasca oil**
Re_p	1.87	6.18	0.107
Re_f	0.064	1.12	0.0673
St	1.85	0.059	0.004
Particle terminal velocity ($\frac{m}{s}$)	0.022	0.146	0.0065

Here is a list of findings that were observed out of the scenarios with and without fluid flow:

1. For the case with the most viscous fluid (Athabasca oil), less particles passed through the slot in the specified time, Table 4.4.

2. The presence of viscous fluid (water and oil) slowed down the flow of the particles, compared with the cases of no fluid and air.

3. There was no multi-particle arch formed in any case.

Table 4.4: Average numbers of particles passing through the slot in the specified time (DEM time step = 0.1 s).

	Frozen solver (no fluid)	**Air**	**Water**	**Athabasca oil**
WWS without porous media	4.3	2.7	1.9	1.5
WWS with porous media	3.2	2.3	1.6	1.1

4.2.4 Slurry Cases with Spherical and Polyhedral Particles

In all previous cases, particles were spherical. In this section polyhedral particles, with aspect ratio larger than 1 and with sharp corners, were tested with slurry flow. Three sizes were tested for the particles within the possible range, corresponding to 3 to 5 times smaller than the slot opening (200, 275 and 375 microns). The slot shape is WWS and the cases were tested with and without porous media on top of the slot. Problem setup is the same as presented in Tables 4.1, except that the particles were polyhedral with aspect ratio equal to 1.6 (Figure 4.11) this time.

The following findings were observed in this study:

1. Surface deposition was observed on the filter surface and at the pores. Size exclusion and sequential arching or sequential bridging (Figure 1.3) were observed in pores as retention mechanisms, shown in Figure 4.7.

2. In the case with the uniform-size polyhedral particles, multi-particle arch was also not formed at the slot.

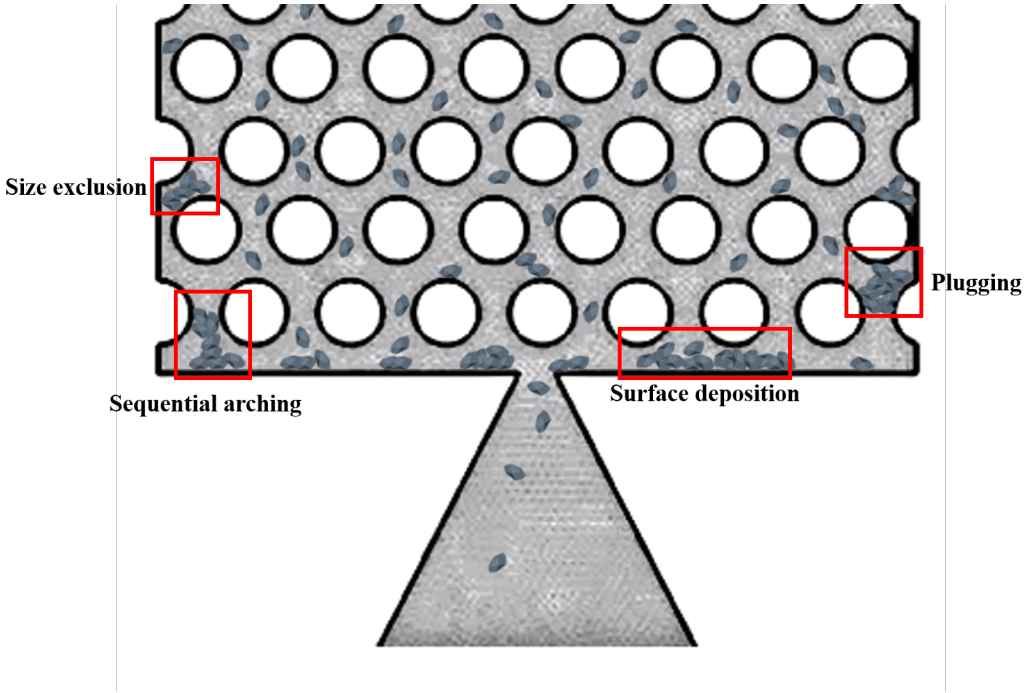

Figure 4.7: Three sand-retention mechanisms were observed: surface deposition, size exclusion and sequential arching in this case with slurry flow of polyhedral particles and porous media on top of the slot (CFD-DEM simulation).

Slurry Case: Particle Build-up Comparison with Experiment The results from the uniform-size polyhedral slurry flow simulation on a WWS opening revealed particle build-up around the slot entrance. They were compared with the particle shadowgraph velocimetry (PSV) experimental results conducted by Kinsale et al[1],[2] on a straight slot. Similar surface deposition and particle build-up around the slots were observed in both simulation and experiment. It could confirm the validity of the simulation results. The scale of the porous media is similar in the experiment and simulation. The experimental particle scale is 40 μm and the scale of the particle used in CFD-DEM simulation is 100 μm. Surface deposition was also observed in both simulation and experiment.

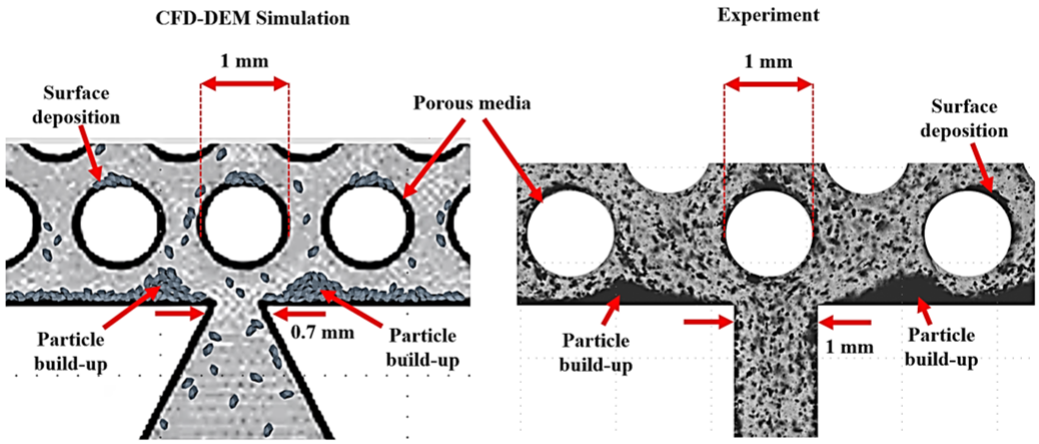

Figure 4.8: Particle build-up comparison between the CFD-DEM simulation on a WWS opening and PSV experiment result[1] on a straight slot

It can be concluded that the difference between the geometry of the two slots had no significant effect on the retention mechanisms and particle build-up

before the slots.

4.2.5 Slurry Cases With Particle Size Distribution

The particle size distribution (PSD) of a slurry defines the relative amount, typically by mass, of particles present in the slurry according to size. In the simulations, PSD was tested to investigate the effect of non-uniform particle distribution on sand-retention mechanisms. Particle size distribution was considered as $D_{10} = 50$ μm, $D_{50} = 200$ μm, $D_{90} = 400$ μm. Problem setup is presented in Table 4.5.

Table 4.5: Mathematical and Computational Model Setup for PSD Case

	Setup
Continuous phase equations	Continuity and NS equations
Fluid phase boundary condition	Top face: velocity inlet = 0.001 $\frac{\text{m}}{\text{s}}$
Fluid phase boundary condition	Other faces: no-slip wall
Fluid initial condition	Quiescent
Discrete phase equations	Newton's 2nd law of motion (conservation of linear and angular momentum)
Particle boundary condition	No-slip wall
Particle initial condition (at t = 0)	Terminal velocity = 0.0097 $\frac{\text{m}}{\text{s}}$
Coupling scale	Smoothed Unresolved
Coupling technique	Two-way coupling
Particle type	DEM particles, Polyhedral
Solid particle material	Glass (solid, sand-like) and heavy/high-density particles
Forces	Pressure gradient force (counts for the buoyancy) Drag force Gravity Interaction forces Lift forces Virtual mass force
DEM model setting	Residence time for particles Track velocity and locations of particles Lagrangian multiphase DEM Multiphase interaction
Grid	3D, Hexahedral
Particle size	$D_{10} = 50$ μm, $D_{50} = 200$ μm, $D_{90} = 400$ μm
Fluid	Athabasca oil ($\mu_f = 0.0136$ Pa $\cdot$ s and $\rho_f = 915.2$ $\frac{\text{kg}}{\text{m}^3}$)
Solid	Glass ($\rho = 2800.0$ $\frac{\text{kg}}{\text{m}^3}$, Poisson's ratio = 0.45, Young's modulus = 517000.0 Pa)
Fluid time discretization Scheme	Implicit unsteady
Temporal order of discretization	2nd order
Fluid flow solver	Segregated flow
Velocity solver	Algebraic multigrid (AMG) linear solver
Pressure solver	AMG linear solver
Fluid equation of state	Constant density
Continuous phase	Viscous regime and laminar ($Re_f = 0.0672, Re_p = 0.239, St = 0.009$)
CFD time-step	0.01 s
DEM time-step	0.1 s

The following is a list of findings observed:

1. Similar to the previous scenario, three sand-retention mechanisms were observed: surface deposition, size exclusion and sequential arching, as shown in Figure 4.9.

2. The average number of particles passing through the slot at the specified equal time was less for the case with PSD than for the uniform case.

3. With polyhedral particles and PSD, multi-particle arch did not form on the slot opening for cases with and without porous media.

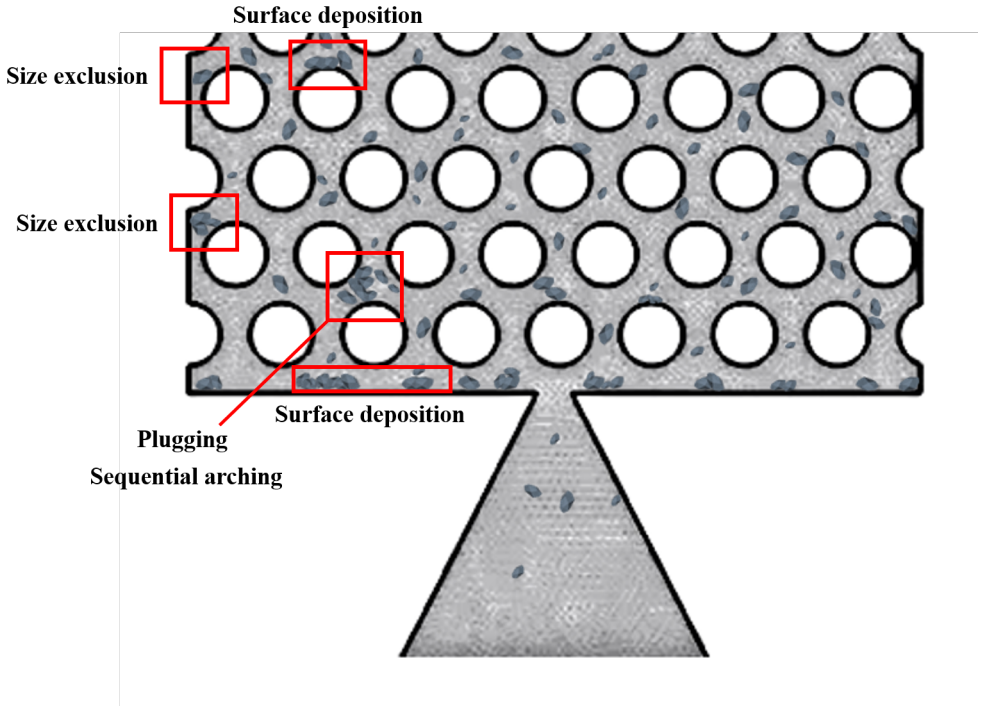

Figure 4.9: Surface deposition, size exclusion and sequential arching were observed with slurry flow, porous media on top of the slot and having PSD.

4.2.6 Slurry Cases: Testing Physical Forces Exclusion

There are various forces playing roles in the simulation of particulate flow passing through the screen slot, which are drag force (fluid stress), buoyancy force, gravity force, virtual mass force, cohesive force, lift force, and solid interaction forces (particle-particle, particle-domain). The summation of the three main forces acted by the fluid on the particles: drag force, buoyancy and virtual mass were considered as the particle-fluid interaction force. Problem

setup is similar to what presented in Tables 4.5. Forces were excluded one by one at a time and the cumulative number of particles passing through the slot in the specified time interval (10 DEM time steps = 1 s) was tracked.

Table 4.6: Cumulative number of particles passing through the slot in the specified time interval (1 s) while a force is removed from simulation.

Omitted force	**WWS without porous media**	**WWS with porous media**
drag force	7	3
buoyancy force	14	5
gravity force	0	0
virtual mass force	12	5
cohesive force	13	5
lift force	12	6
particle-fluid interaction force	6	4
particle-particle interaction force	6	3
particle-wall interaction force	5	3

The main forces that caused particles to pass through the slot were gravity and interaction forces (particle-wall interaction, particle-fluid interaction, particle-particle interaction) since by omitting them there is less particles passing through the slot. Note that the particle-fluid interaction combines the main fluid forces (drag, buoyancy and virtual mass force). In the slurry case, the particle concentration is low and there was no formation of multi-particle arch in any case.

4.2.7 Slurry Cases: Testing Various Slot Shapes

In this series of simulations, four different slot geometries were tested under conditions similar to those presented in Table 4.5. The objective was the investigation of the possibility of arch formation with different slot geometries,

Figure 4.2. These cases were tested having a porous region on top of the slot opening and with/without fluid. The simulation results confirmed that there was no arch formed, neither mechanical nor hydrodynamic. Various geometries (keystone, WWS, straight and seamed slots) could not help with the arch formation, while having slurry flow. Table 4.7 presents the average number of particles passing through each slot in the specified time interval that is 10 DEM time steps = 0.1 s.

Table 4.7: Average number of particles passing through the slot in the specified time interval (0.1 s) for different slot shapes.

	WWS	**Seamed**	**Keystone**	**Straight**
Porous media on top	2.1	1.8	2.2	2.1
No porous media	3	2.5	3.6	2.9

4.2.8 Slurry Cases: Testing Various Slot Widths and Lengths

In these simulations, various slot widths and lengths were tested to investigate the possibility of the arch formation with different slot widths and lengths. Values of $6d_p$, $5.5d_p$, $5d_p$, $4d_p$, $3d_p$, $2.5d_p$ and $2d_p$ were tested for the length and width of the slot, where d_p is the particle diameter. The flow regime was laminar in all cases studied. In any cases, no mechanical or hydrodynamic multi-particle bridges were formed. Cases were also explored, in which particles were deliberately injected in the arch-shape locations initially to support the arch formation. This strategy did not help either. The results confirmed that

the slurry flow does not result in multi-particle arch formation.

4.2.9 Discussion

Following validation of the CFD-DEM model, in various scenarios the possibility of multi-particle arch formation was investigated by modeling the slurry flow with various test conditions. Three retention mechanisms: size exclusion, surface deposition and sequential arching were observed, Figure 4.9. However, no multi-particle arch was formed at the slot. The conclusion is that the multi-particle arching phenomenon does not occur during the slurry flow in various types of sand screen's openings. These results occurred even for a narrow slot.

The slurry flow can occur during the initial phase of a SAGD process, called warm-up[39], followed by formation of a loosened packed-bed[71],[72],[73] called unconsolidated packed-bed in the gap between the sand filter and the oil-sand reservoir. The investigation on slurry cases confirms the finding that the stress from the packed-bed of solid particles on top of the slot opening might be essential to form the multi-particle arch as the retention mechanism.

Particulate flow with a packed-bed on the sand filter will be discussed next in this chapter. It was clear from the majority of the simulated slurry scenarios that the concentration of the particles was too diluted to result in multi-particle arch formation. The results could also suggest the importance of the gravity, particle-fluid interaction force and particle-particle interaction force to model the transport of particles around and into the slot in the slurry flow.

The current work provided the platform to start the next phase of the

research that was modeling and investigating of multi-particle sand arch formation using a packed-bed of the sand particles in the gap between the sand filter and oil-sand reservoir.

4.3 Unstable Packed-Bed

Based on the findings of the previous section, the conclusion was that multi-particle arching could not happen if there was slurry flow in the gap between the reservoir and the sand screen. In this section, no porous medium of fixed obstacles was used. Instead, a packed-bed of loose sand particles was created to apply additional stress to the particles on top of the slot. This was an attempt to achieve the multi-particle arch formation. By increasing the concentration of particles in the gap between the reservoir and the screen, a packed-bed of loose sand particles was formed as the representative of sand layers usually present between the sand screen and the reservoir. This region, which is also called the unconsolidated porous region, has typically a porosity between 0.3 to 0.4[104]. Packed-bed was produced in simulations through two approaches, resulting in unstable and stable beds.

In this section, various scenarios of unstable packed-beds were investigated. The beds were called unstable because they were constantly perturbed by the deposition of the new particles during the fluid flow. Simulations were conducted on slots with various geometries, and the effect of various parameters and conditions that might contribute to the formation and stability of the multi-particle arch were investigated. In these type of investigations, replication of the simulations matters. The same scenarios were simulated multiple times to ensure that the results were reproducible. These studies were conducted at micro-scale level with several sizes of particles ($50\ \mu\text{m} < d_p < 400\ \mu\text{m}$) and various shapes. Athabasca oil was used as the viscous fluid in the majority of

the simulations.

4.3.1 Unstable Packed-Bed Setup

In the simulations to form the packed-bed on top of the slot in the unstable bed, solid particles were continuously injected from the top of the domain in order to keep the porosity of the unconsolidated region equal to the assigned number between 0.3 and 0.4. In unstable packed-bed formation, the slot remained open from the beginning and during the particle injection, which resulted in an unstable bed (see Figure 4.10). Because of this approach, the packed-bed never had a chance to settle and become stable. It is clear from the images in Figure 4.10 that while the packed-bed was created, the slot was open and particles continuously passed through the slot.

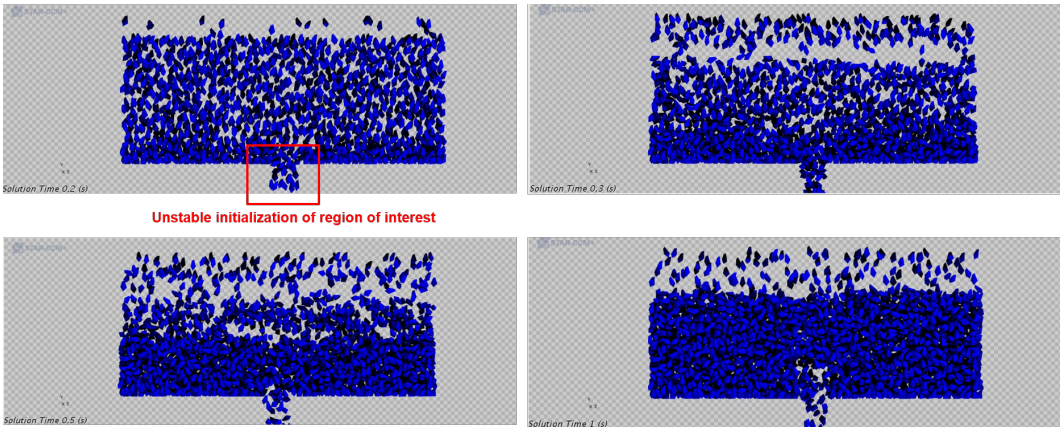

Figure 4.10: Unstable packed-bed formation of polyhedral sand particles

4.3.2 Unstable Packed-Bed without and with Fluid Flow

In this section, the effect of fluid type was investigated in multi-particle arch formation in the unstable packed-bed simulations. In addition to the extreme case of a frozen fluid solver (no fluid), three fluid cases with various thermophysical properties were simulated: Air ($\mu_f = 1.849 \times 10^{-5}$ Pa $\cdot$ s and $\rho_f = 1.184$ $\frac{\text{kg}}{\text{m}^3}$), Athabasca oil ($\mu_f = 0.0136$ Pa $\cdot$ s and $\rho_f = 915.2$ $\frac{\text{kg}}{\text{m}^3}$) and water ($\mu_f = 8.8871 \times 10^{-4}$ Pa $\cdot$ s and $\rho_f = 997.561$ $\frac{\text{kg}}{\text{m}^3}$). These fluids have different viscosities and densities and are assumed to be Newtonian fluids. The problem setup is similar to Table 4.5.

Table 4.8 lists the times when multi-particle arching happened for the first time named stage 1 (arch formed), when this arch broke named stage 2 and when the arch formed again after breakage (arch reformed) named stage 3. In addition, the periods during which the arch was stable and the periods of sand production, until the arch formed again, are also shown.

The following is the list of findings that were observed:

1. In all cases shown in Table 4.8, the multi-particle arch formed with/without fluid, then broke after a period of time and reformed, and this pattern continued.

2. According to Table 4.8, without fluid the arch formed faster at 8.63 seconds. However, it stayed stable for a shorter time and reformed more quickly after breakage. In this case, the particle-particle interaction forces between the particles and the gravity force played key roles in arch formation. The particle-fluid interaction forces could be considered

non-essential in arch formation, as without it the multi-particle arch still formed in the case with no fluid.

3. By increasing the fluid viscosity, it took longer for the initial arch to form. The stabilization period was longer and, following destruction, it took longer for the arch to reform.

Table 4.8: Monitored times (in seconds) for when multi-particle arching happened, broke and reformed as well as stabilization and reformation corresponding periods in a straight slot.

	Frozen Solver (No Fluid)	**Air**	**Water**	**Athabasca oil**
Arch formed	Stage 1: 8.63	Stage 1: 11.35	Stage 1: 13.37	Stage 1: 14.77
Arch broke	Stage 2: 10.12	Stage 2: 14.58	Stage 2: 17.14	Stage 2: 18.87
Arch reformed	Stage 3: 14.42	Stage 3: 19.63	Stage 3: 22.91	Stage 3: 25.01
Stabilization period	1.49	3.23	3.77	4.1
Reformation period	4.3	5.05	5.77	6.14

4.3.3 Unstable Packed-Bed with Spherical Particles and Polyhedral Particles

In this section, the objective is to investigate the effect of the particles' shape on multi-particle arch formation and its stability. The CFD-DEM simulations were conducted with spherical and polyhedral particles on a straight slot in 3D. Problem setup is similar to Table 4.5. The study was done on straight slot with spherical particles and polyhedral particles and different aspect ratios (AR), Table 4.9. The aspect ratio of a particle is defined as the ratio of its major dimension and minor dimension.

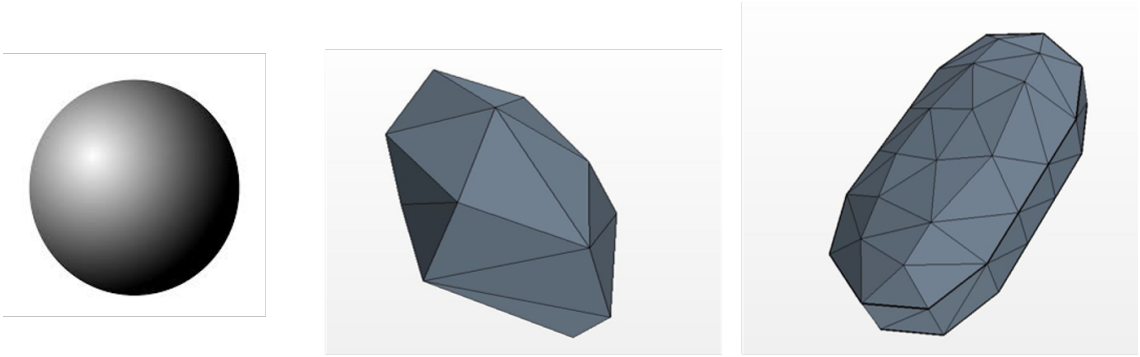

Figure 4.11: Particle shapes with aspect ratios from left to right: 1, 1.6 and 2.3

Table 4.9: Monitored times (in seconds) for when multi-particle arching happened, broke and reformed as well as stabilization and reformation corresponding periods in a straight slot.

	Spherical particle (AR = 1)	**Polyhedral particle (AR = 1.6)**	**Polyhedral particle (AR = 2.3)**
Arch formed	Stage 1: 15.67	Stage 1: 10.73	Stage 1: 12.35
Arch broke	Stage 2: 17.25	Stage 2: 15.23	Stage 2: 16.01
Arch reformed	Stage 3: 23.07	Stage 3: 18.93	Stage 3: 20.74
Stabilization period	1.58	4.5	3.66
Reformation period	5.82	3.7	4.73

The following is the list of findings that were observed:

1. In all cases, multi-particle arching happened with spherical and polyhedral particles.

2. According to Table 4.9, with non-spherical particles the multi-particle arch formed faster initially and also after breakage, it reformed faster. Arch that was formed with polyhedral particles stayed stable for a longer time than the case with the spherical particle.

3. For non-spherical particles with lower aspect ratio (AR = 1.6), the arch stayed stable longer than the polyhedral case with the higher aspect ratio (AR = 2.3). Also, arch reformed in a shorter time with particles with lower aspect ratio.

Arch formation and breakage, having an unstable packed-bed of polyhedral particles on top of the slot, is represented in the Figure 4.12.

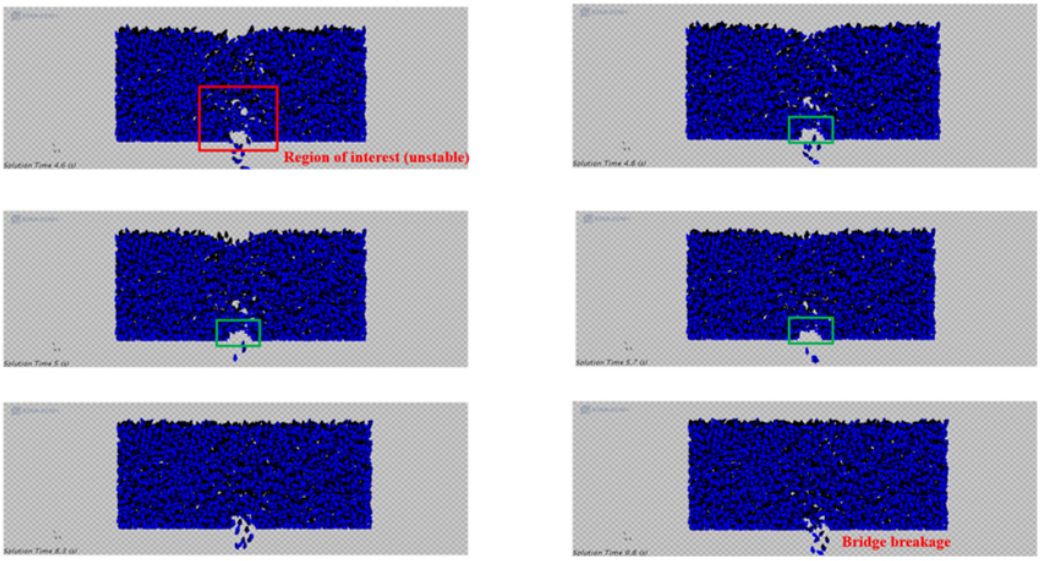

Figure 4.12: Arch formation and breakage with unstable packed-bed of polyhedral particles.

4.3.4 Unstable Packed-Bed with Particle Size Distribution

In this section, the objective is to investigate the effect of the particle size distribution on multi-particle arch formation and stability. The investigations were conducted on WWS. Problem setup is similar to Table 4.5. Results are

presented in Table 4.10.

Table 4.10: Monitored times (in seconds) for when multi-particle arching happened, broke and reformed as well as stabilization and reformation corresponding periods.

	Spherical particle (AR = 1), Uniform	**Polyhedral particle (AR = 1.6), Uniform**	**Polyhedral particle (AR = 1.6), PSD**
Arch formed	15.67	10.73	11.65
Arch broke	17.25	15.23	17.08
Arch reformed	23.07	18.93	21.13
Stabilization period	1.58	4.5	5.43
Reformation period	5.82	3.7	4.05

The following is the list of findings that were observed:

1. For particle size distribution at micro-scale, the initial formation of the multi-particle arch took longer than the case with the uniform-size distribution.

2. With PSD, the multi-particle arch stayed stable for a longer time. It took longer to reform the multi-particle arch compare to the uniform-size case.

4.3.5 Unstable Packed-Bed: Force Exclusion

When a multi-particle arch forms, there are various physical forces involved, such as fluid drag force, interaction forces (particle-particle, and particle-wall), lift forces, gravity force, buoyancy, and virtual mass force as well as the particle-fluid interaction force that is considered as the summation of the drag force, buoyancy and virtual mass force. It is important to understand the role of

each force in multi-particle arch formation and stability. This investigation was done with PSD and uniform cases. The forces were excluded one by one and the cumulative number of particles passing through the slot in the specified time interval (10 DEM time-steps = 1 s) was tracked. Table 4.11 presents the results of these studies.

Table 4.11: Cumulative number of particles passing through the slot in the specified time interval (1 s) while a force was omitted.

Omitted force	**WWS with uniform distribution** (200 μm)	**WWS with PSD**
drag force	5	4
buoyancy force	4	5
gravity force	0	0
virtual mass force	2	5
cohesive force	3	5
lift force	6	4
particle-fluid interaction force	6	4
particle-particle interaction force	16	13
particle-wall interaction force	15	14

The following is the list of the findings that were observed:

1. The forces essential to form the arch are: gravity force and interaction forces. By removing interaction forces, particles passed through the slot by gravity and no arch was formed.

2. Without other individual forces (fluid drag force, lift forces, buoyancy, cohesive force, virtual mass force) multi-particle arch formed, stayed stable, broke and reformed.

3. Without particle-fluid interaction force, which was equivalent to omitting 3 forces (buoyancy, drag and virtual mass), arch formed.

4. This study was conducted on two slot types (WWS and Straight) with PSD and the observations were similar.

5. By the simulations with the unstable packed-bed, it was found that the gravity force and particle-particle interaction forces and particle-wall were main forces in arch formation.

4.3.6 Unstable Packed-Bed with Reservoir Load

In this section, the goal was to add the stress of consolidated reservoir to the simulations and to investigate its effect on the region close to the slot and on the multi-particle arch behavior. The approach chosen to add more stress on top of the packed-bed was to increase the height of the unconsolidated region, that is the height of the packed-bed. Three heights were applied with two porosities (ϕ): 0.3 and 0.4. The multi-particle arch behavior was tested under different stress loads of particles (see Figures 4.13 and 4.14).

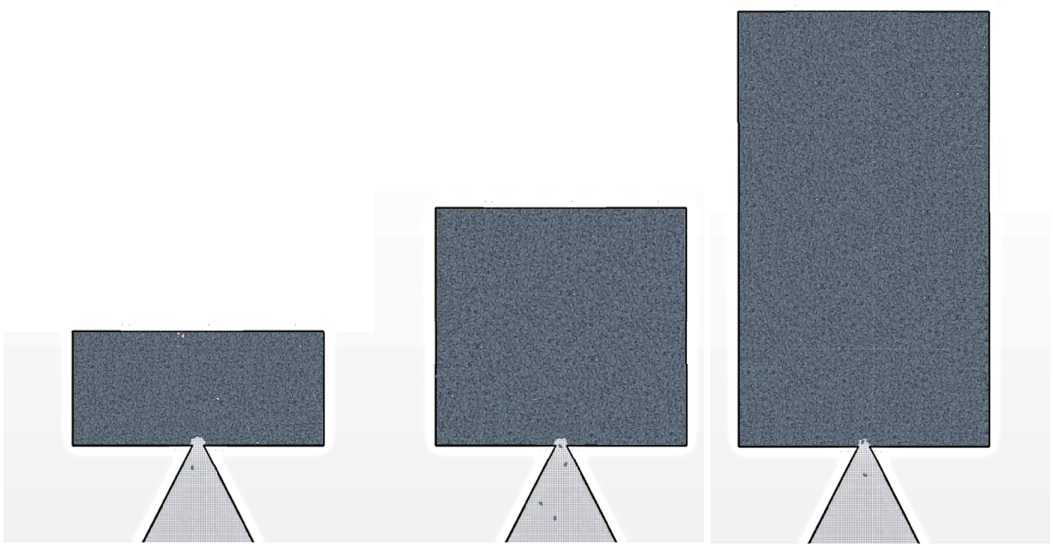

Figure 4.13: Arch formation with various heights of the unstable packed-bed

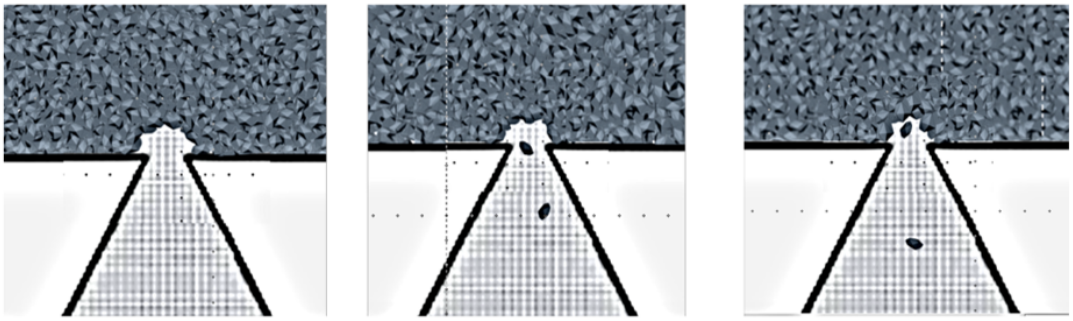

Figure 4.14: Zoom in of Figure 4.13 at the slot locations

Table 4.12: Various reservoir loads ($\phi = 0.3$): Monitored times (in seconds) for when multi-particle arching happened, broke and reformed with polyhedral particles (AR = 1.6) as well as stabilization and reformation corresponding periods.

	Short height	**Medium height**	**Large height**
Arch formed	12.38	10.12	9.35
Arch broke	16.01	14.03	14.86
Arch reformed	22.34	19.41	18.67
Stabilization period	3.63	3.91	5.51
Reformation period	6.33	5.38	3.81

Table 4.13: Various reservoir loads ($\phi = 0.4$): Monitored times (in seconds) for when multi-particle arching happened, broke and reformed with polyhedral particles (AR = 1.6) as well as stabilization and reformation corresponding periods.

	Short height	**Medium height**	**Large height**
Arch formed	13.18	10.89	9.87
Arch broke	16.77	14.53	15.33
Arch reformed	23.45	21.01	19.87
Stabilization period	3.59	3.64	5.46
Reformation period	6.68	6.48	4.44

The following is the list of findings that were observed:

1. In all 6 cases, arch formed, broke and reformed.

2. The increased height of the unconsolidated region resulted in the arch forming for in a shorter period of time, and it was stable for a longer period of time than the case with the shorter height.

3. It took shorter for the arch to reform after breakage for the case with the increased height of the unconsolidated region.

4.3.7 Discussion

Following the research done on the slurry flow, the multi-particle arch formation was studied using an unstable packed-bed. The reason to instability of the bed was that the slot remained open while the sand particles were continuously injected into the packed-bed. In this case, particles did not get a chance to make a settled packed-bed due to perturbation caused by the continuous injection of particles. As a result, the arch formed, however, did not remain stable.

The effects of various parameters and conditions were studied on multi-particle arch formation, stabilization, destruction and reformation, such as the effect of the physical forces, shape and size of the particles, and reservoir load.

The following is the list of the findings that were observed:

1. Two forces were critical to form the multi-particle arch: gravity force and interaction forces between the particles and particle-domain at the micro-scale.

2. Without other forces (fluid drag force, lift forces, buoyancy, cohesive force) the multi-particle arch formed, stayed stable for a short while, broke and reformed.

3. With particle size distribution at micro-scale, the initial formation of the multi-particle arch took longer than the case with uniform-size distribution, and the multi-particle arch stayed stable for a longer time than the case with uniform-size distribution. It took longer to reform the multi-particle arch compared to the uniform case.

4. In all cases, multi-particle arching happened with spherical and polyhedral particles.

5. With non-spherical particles, the multi-particle arch formed faster and stayed stable for a longer period of time than the case with spherical particles.

6. For non-spherical particles with lower aspect ratio, the multi-particle arch stayed stable longer than for the polyhedral case with higher aspect ratio.

7. The increase in height of the packed-bed region resulted in the multi-particle arch forming in a shorter period of time, and the multi-particle arch was stable for a longer period of time than the case with shorter height of the packed bed.

8. This study was conducted on two slot types (WWS and Straight) and the conclusions were similar.

9. It took shorter for the multi-particle arch to form also reform after breakage for the case with the increased height of the packed-bed region (increased stress).

With the unstable packed-bed, the pattern of arch formation, stabilization, destruction and reformation was observed. In the unstable packed-bed cases, the number of the particles passing through the slot decreased significantly following the visible multi-particle arch formation. However, there were always a few particles passing through the slot, even after multi-particle arch formation.

The period of time that the multi-particle arch was stable was relatively brief, and the pattern of arch formation, stabilization, destruction and reformation repeated many times.

In the next section, a study was conducted with a different method of packed-bed creation that aimed at removing the perturbations and creating a stable packed-bed.

4.4 Stable Packed-Bed

In this section, the phenomena of multi-particle arch formation, stabilization, destruction and reformation are discussed on top of the slot with the stable packed-bed. Various stable packed-bed scenarios were examined to improve the knowledge on the arch formation, stabilization, destruction, and reformation. Simulations were conducted on slots with different geometries: WWS, straight, seamed and keystone. In the majority of the cases studied in the following sections, arching occurred, and the effect of various parameters and conditions on the formation and stability of the arch were studied. The same scenarios were run multiple times to assure that same results were obtained. These studies were also conducted at micro-scale level of particle size ($50\ \mu\text{m} < d_p < 400\ \mu\text{m}$) and with Athabasca oil as the viscous fluid.

4.4.1 Stable Packed-Bed Setup

In this section, to form the packed-bed on top of the slot, solid particles were injected from top of the domain and injection continued to reach the porosity

of the region equal to the assigned number between 0.3 and 0.4. In stable packed-bed formation, the slot was initially closed while particle injection was active, and consequently, the packed-bed had a chance to settle and become stable before opening the slot. No further particles were injected after opening the slot. In the next sections, the multi-particle arch behavior under various conditions applied in the stable bed will be discussed.

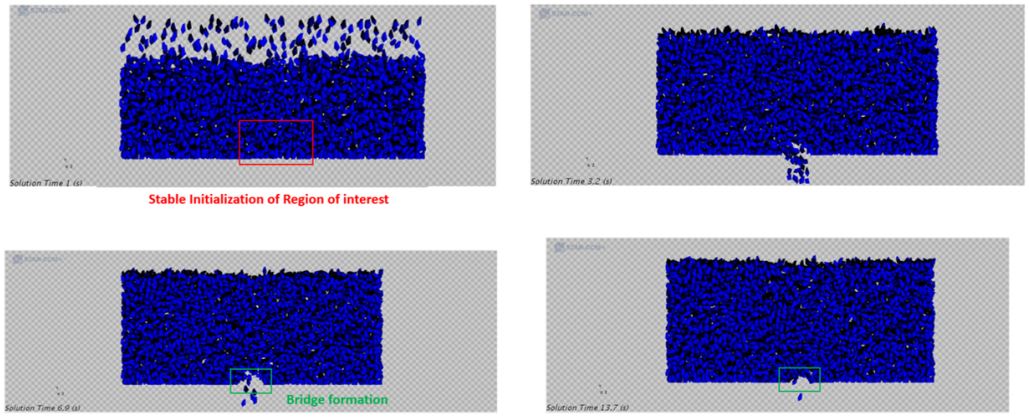

Figure 4.15: Stable packed-bed formation with closed slot and bridge formation after opening the slot.

Figure 4.15 presents how the stable packed-bed was formed while the slot was closed during particle injection into the bed. Following bed formation, the slot was opened and particles passed through the slot until the arch visibly formed and only very few particles passed through the slot.

4.4.2 Stable Packed-Bed: without and with Fluid

In this section, the role of fluid was investigated in multi-particle arch formation. Four cases were studied similar to unstable packed-bed with no fluid, as well

as three fluid cases with various thermophysical properties: air, water and Athabasca oil. Observations out of the simulations were similar to the unstable packed-bed cases. The mathematical and computational model setup was similar to the unstable packed-bed case with and without fluid.

The following is the list of findings that were observed:

1. In all cases shown in Table 4.14, the arch formed with/without fluid, broke after a period of time and reformed again, and this pattern continued, similar to the unstable packed-bed.

2. Without fluid, the arch formed faster. However, it stayed stable for a shorter period of time and reformed more quickly after breakage. In this case, it seems that the particle-particle interaction force and the gravity force played key roles in arch formation. Arch formation without fluid leads to the conclusion that particle-fluid interaction forces might not be essential for multi-particle bridging at micro-scale.

3. Compared to the unstable packed-bed case, the arch stayed stable for a longer time and the number of the particles passing through the slot, following arch formation, was less.

Table 4.14: Monitored times (in seconds) for when multi-particle arching occured, broke and reformed in the case of stable packed-bed with polyhedral particles (AR = 1.6) and a straight slot.

	Frozen solver	**Air**	**Water**	**Athabasca oil**
Arch formed	6.11	8.73	9.16	9.72
Arch broke	10.05	13.13	15.47	17.31
Arch reformed	11.55	16.21	18.83	20.74
Stabilization period	3.94	4.4	6.31	7.59
Reformation period	1.5	3.08	3.36	3.43

4.4.3 Stable Packed-Bed: Spherical and Polyhedral Particles

In this section, the objective was to investigate the effect of the particles' shape on arch formation and stability. The CFD-DEM simulations were conducted with spherical and polyhedral particles. The study was done on WWS and seamed slot with polyhedral particles and different aspect ratios (AR), Table 4.15. Problem setting was similar to the previous case with Athabasca oil.

Table 4.15: Monitored times in seconds: arch formed (stage 1), broke (stage 2) and reformed (stage 3) in case of stable packed-bed and different aspect ratios for particles.

	Spherical particle (AR = 1)	**Polyhedral particle (AR = 1.6)**	**Polyhedral particle (AR = 2.3)**
WWS	Stage 1: 12.34 Stage 2: 16.05 Stage 3: 21.84	Stage 1: 6.85 Stage 2: 12.35 Stage 3: 16.79	Stage 1: 8.02 Stage 2: 13.31 Stage 3: 18.05
Stabilization period	3.71	5.5	5.29
Reformation period	5.79	4.44	4.74
Seamed slot	Stage 1: 13.93 Stage 2: 17.08 Stage 3: 23.05	Stage 1: 9.88 Stage 2: 14.92 Stage 3: 19.78	Stage 1: 10.99 Stage 2: 15.21 Stage 3: 20.92
Stabilization period	3.15	5.04	4.22
Reformation period	5.97	4.86	5.71

Table 4.16: Monitored times in seconds for a straight slot: arch formed (stage 1), broke (stage 2) and reformed (stage 3) as well as stabilization and reformation corresponding periods.

	Spherical particle (AR = 1)	**Polyhedral particle (AR = 1.6)**	**Polyhedral particle (AR = 2.3)**
Straight slot with unstable packed-bed	Stage 1: 15.67 Stage 2: 17.25 Stage 3: 23.07	Stage 1: 10.73 Stage 2: 15.23 Stage 3: 18.93	Stage 1: 12.35 Stage 2: 16.01 Stage 3: 20.74
Stabilization period	1.58	4.5	3.66
Reformation period	5.82	3.7	4.73
Straight slot with stable packed-bed	Stage 1: 11.34 Stage 2: 14.81 Stage 3: 19.07	Stage 1: 8.67 Stage 2: 14.83 Stage 3: 17.93	Stage 1: 11.05 Stage 2: 15.51 Stage 3: 19.03
Stabilization period	3.47	6.16	4.46
Reformation period	4.26	3.1	3.52

Table 4.16 presents the monitored times in seconds for formation, breakage and reformation of the arch in a straight slot with stable and unstable packed beds. The stabilization and reformation corresponding periods are also presented. With the stable packed-bed arch forms faster, stays stable for a longer time and reform faster in comparison to the unstable packed bed.

The following is the list of findings that were observed:

1. In all cases, multi-particle arching occurred with both spherical and polyhedral particles.

2. With non-spherical particles, the arch formed faster and stayed stable for a longer time than the case with spherical particle also in comparison with the unstable packed-bed similar case, the arch stayed stable longer.

3. For non-spherical particles with higher aspect ratio of 2.3, the arch was less stable than the case with the lower aspect ratio of 1.6. The polyhedral shape of the particles used in the simulations was presented in Figure 4.11.

4. There were fewer particles passing through the slot during the stabilization period than in the case of unstable packed-bed. This was a clear difference between the stabilization period in stable and unstable packed bed cases.

Figure 4.16 presents the multi-particle arch in the stable packed-bed that formed and stayed stable during simulation time.

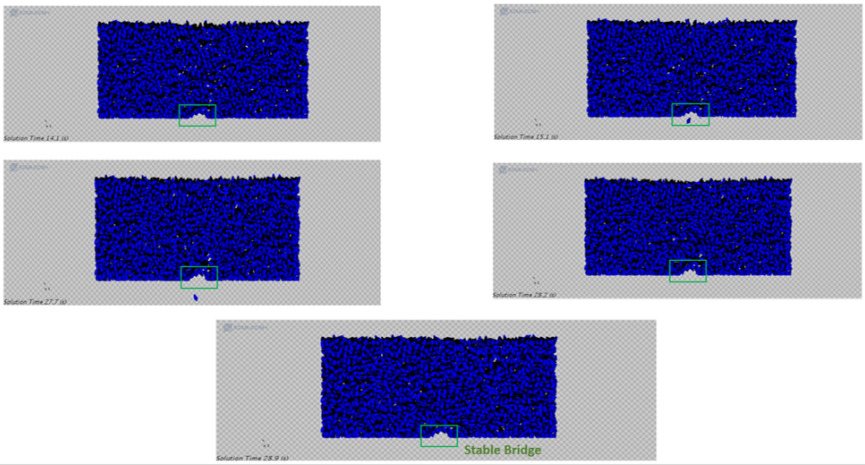

Figure 4.16: Arch formation and stabilization with a stable packed-bed

4.4.4 Stable Packed-Bed: Particle Size Distribution

In this section, the objective was to investigate the effect of the particle size distribution on arch formation and stability. The investigations were conducted on WWS. Problem setup is similar to the unstable packed-bed case with PSD. Table 4.17 presents the monitored times (in seconds) for when multi-particle arching happened, broke and reformed for WWS opening. In this section, the objective was to investigate the effect of the particle size distribution on arch formation and stability. The investigations were conducted on WWS. Problem setup is similar to the unstable packed-bed case with PSD. Table 4.17 presents the Monitored times (in seconds) for when multi-particle arching happened, broke and reformed for WWS opening.

Table 4.17: Monitored times (in seconds) for when multi-particle arching happened, broke and reformed for WWS for a stable packed-bed comparing uniform and PSD cases.

	Spherical particle (AR = 1), uniform	**Polyhedral particle (AR = 1.6), uniform**	**Polyhedral particle (AR = 1.6), PSD**
Arch formed	12.43	8.65	9.13
Arch broke	16.08	13.58	14.81
Arch reformed	20.38	17.47	19.23
Stabilization period	3.65	4.93	5.68
Reformation period	4.3	3.89	4.42

The following is the list of findings that were observed:

1. With the uniform spherical case, it took longer for the arch to form. Arch stayed stable for a shorter period of time compare to the polyhedral cases. It also took longer for the arch to reform after breakage in comparison

with the polyhedral cases. The stabilization period was longer than in the unstable packed-bed case.

2. With polyhedral particle size distribution at micro-scale, the initial formation of the multi-particle arch took longer than the case with the uniform-size distribution similar to what observed with the unstable packed-bed.

3. With PSD case, the arch stayed stable for a longer time than the uniform cases (both polyhedral and spherical). Following arch breakage, it took longer to reform the arch compared to the uniform-size cases.

4.4.5 Stable Packed-Bed: Force Exclusion

In this part, the role of each force in arch formation and stability was explored with stable packed-bed. This investigation was conducted with polyhedral PSD and uniform cases. Time was tracked for three stages as before: arch formation, destruction and reformation. Table 4.18 presents the cumulative number of particles passing through the slot in the specified time interval (10 DEM time steps = 0.1 s) while a force was omitted.

Table 4.18: Cumulative number of particles passing through the slot in the specified time interval (0.1 s) while a force is omitted.

Omitted force	**WWS with uniform distribution of polyhedral particles (AR = 1.6)**	**WWS with PSD of polyhedral particles (AR = 1.6)**
drag force	4	3
buoyancy force	3	4
gravity force	0	0
virtual mass force	2	4
cohesive force	2	3
lift force	3	1
particle-fluid interaction force	5	2
particle-particle interaction force	13	12
particle-wall interaction force	9	11

Arch was formed in all cases but three when the gravity force was omitted, when particle-particle interaction force was omitted and when particle-wall interaction force was omitted. Regarding the role of gravity, in case when the slot is on top of the slotted liner, since the gravity is along the flow direction, it helps the arch to form as we have gravity force plus the momentum force created by the flow. However, in the other case, when the slot is at the bottom of the slotted liner, the momentum force has to overcome the gravity force to form the arch. If not, the arch would not form because it does not have an upward net force. In other words, there should be a net force facing upward to maintain the structure of the arch. In SAGD, the stress load on the particles is caused by the thermal expansion of the reservoir, which produces a stress load much bigger than gravity. However, it cannot be represented in the current CFD model.

The following is the list of the findings that were observed:

1. Gravity force and interaction forces (particle-particle and particle-wall) are essential to form the arch.

2. Without other forces (fluid drag force, lift forces, buoyancy, cohesive force, fluid-particle interaction force, virtual mass force) arch formed, stayed stable, broke and reformed.

This set of simulations confirmed again that with a stable packed-bed gravity force, particle-particle interaction force, and particle-wall interaction force were critical to form the multi-particle arch at the slot opening.

4.4.6 Stable Packed-Bed: with Reservoir Load

In this section, the stress of the reservoir was added to the packed-bed in different ways to investigate its effect on the region close to the slot and on the multi-particle arch behavior. The approaches taken are as follows:

1. A porous medium was placed on top of the unconsolidated region to act as the reservoir. The porous medium had a high density and was simulated as a porous region.

2. The height of the unconsolidated region, that is the height of the packed-bed, was increased to replicate the stress of the reservoir and to add stress on the slot region under two circumstances:

    - All particles were sand particles size-wise and property-wise.
    - Particles added, to increase the height of the unconsolidated region, were huge particles heavier than sand.

Adding the Porous Medium on Top of the Unconsolidated Region

The steps taken to simulate the porous media on top of the unconsolidated region was similar to the simulation and setup of the porous media in Chapter 3 of the thesis. Porous media was simulated as a high-density porous medium with densities equal to 7800, 5000, 3500 $\frac{\text{kg}}{\text{m}^3}$. This study was conducted with the stable packed-bed since particle injection had to stop to setup the porous media on top of the unconsolidated region.

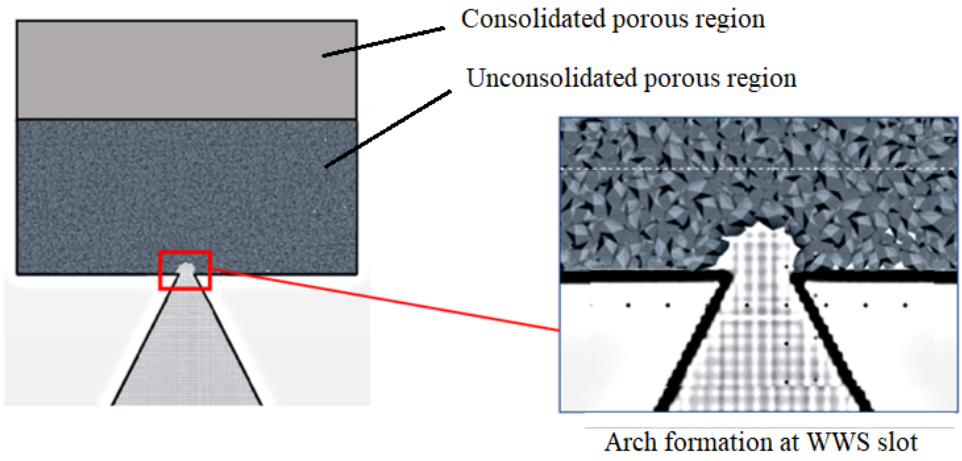

Figure 4.17: Arch formation with a heavy porous region on top of the stable packed-bed (attempt to replicate the consolidated reservoir)

Table 4.19: Testing a porous medium with different densities: Monitored times (in seconds) for arch formation/stabilization/destruction and reformation on WWS.

	$\rho = 3500\ \frac{kg}{m^3}$	$\rho = 5000\ \frac{kg}{m^3}$	$\rho = 7800\ \frac{kg}{m^3}$	**No porous media**
Arch formed	8.02	7.84	8.16	8.11
Arch broke	12.73	12.57	13.02	12.93
Arch reformed	17.39	17.37	18.01	17.88
Stabilization period	4.71	4.73	4.86	4.82
Reformation period	4.66	4.8	4.99	4.95

According to the Table 4.19, applying the fixed porous medium did not affect the arch behavior for each of the three cases with various densities. With this approach, the stress from the porous medium representing the consolidated reservoir was not transferred to the unconsolidated region and consequently did not transfer to the slot region.

Increasing the Height of the Unconsolidated Region

In other cases, the height of the unconsolidated region was increased and the effect of the increased stress caused by the increased height on the slot was studied. This was done using two approaches:

1. The solid particles had size and density similar to the sand particles as presented in Figure 4.18.

2. The solid particles used to increase the height and reservoir load were heavier and larger than sand particles with densities equal to 7800 $\frac{kg}{m^3}$, 5000 $\frac{kg}{m^3}$, 3500 $\frac{kg}{m^3}$ as presented in Figure 4.19.

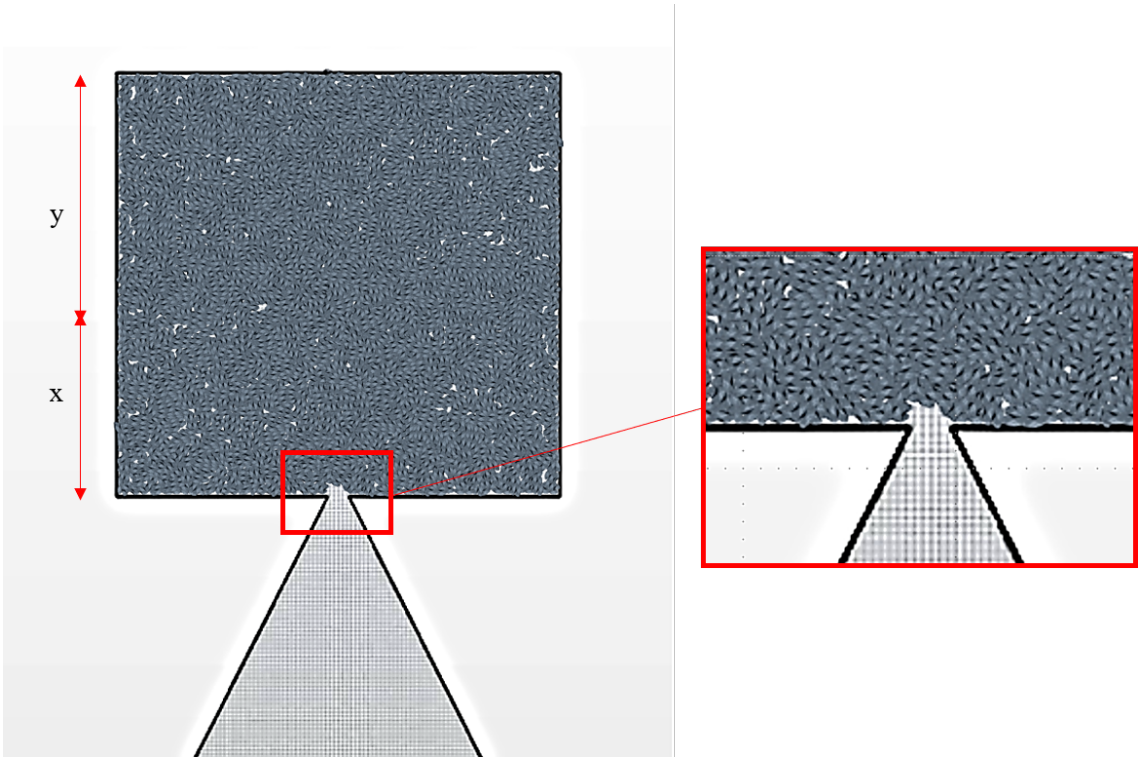

Figure 4.18: Increasing stress load by adding the height y of sand particles.

In Figure 4.18, x was initial height of the packed bed fixed and y was the increased height that could be variable. The results are presented in Table 4.20.

Table 4.20: Increasing reservoir load by increasing the height of the unconsolidated region: monitored times (in seconds) for arch formation/stabilization/destruction and reformation on WWS.

	Stable packed-bed of particles at height x	**Stable packed-bed of sand particles at height x+y**	**Stable packed-bed of sand and heavy particles at height x+y**
Arch formed	9.05	8.64	7.93
Arch broke	12.43	13.31	13.67
Arch reformed	16.71	16.92	17.18
Stabilization period	3.38	4.67	5.74
Reformation period	4.28	3.61	3.51

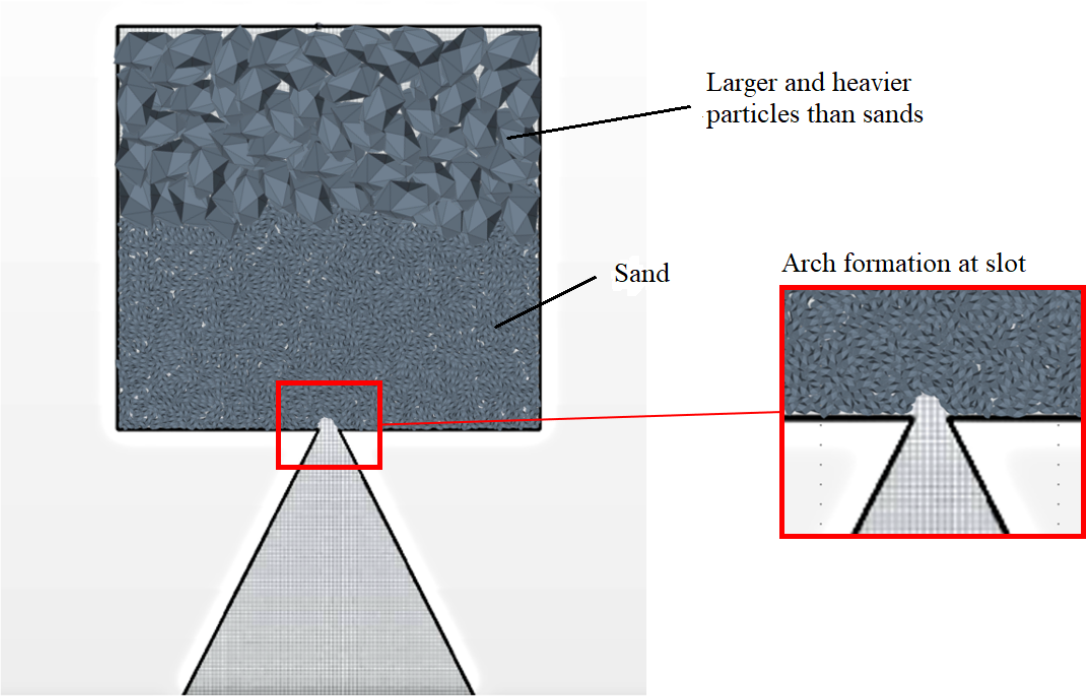

Figure 4.19: Increasing stress load by increasing the height of unconsolidated region with heavier and larger particles than sand.

The following is the list of findings that were observed:

1. In all cases tested, multi-particle arch formed, stayed stable, broke and reformed.

2. The increased height resulted in increased stress over the unconsolidated region near the slot. The increased height with heavy and large particles resulted in a larger increase of the stress load than the increased height with sand particles.

3. As the stress load increased, the arch formed faster, and it was stable for

a longer period of time in comparison with the lower stress load cases.

4. It took shorter for the multi-particle arch to reform after breakage for the cases with increasing stress load.

4.4.7 Stable Packed-Bed: Testing Various Slot Shapes

In this simulation, four different slot geometries were tested under conditions presented in Table 4.21. The objective was the investigation of the arch formation, stabilization, destruction and reformation with different slot geometries.

Table 4.21: Mathematical and computational model setup for various slot shapes

	Setup
Continuous phase equations	Continuity and NS equations
Fluid phase boundary condition	Top face: velocity inlet = 0.001 $\frac{\text{m}}{\text{s}}$
Fluid phase boundary condition	Other faces: no-slip wall
Fluid initial condition	Quiescent
Discrete phase equations	Newton's 2nd law of motion (conservation of linear and angular momentum)
Particle boundary condition	No-slip wall
Particle initial condition	Terminal velocity = 0.0097 $\frac{\text{m}}{\text{s}}$
Coupling scale	Smoothed Unresolved
Coupling technique	Two-way coupling
Particle type	DEM particles, Polyhedral
Solid particle material	Glass (solid, sand-like) and heavy/high-density particles
Forces	Pressure gradient force (counts for the buoyancy) Drag force Gravity Interaction forces Lift forces Virtual mass force
DEM model setting	Residence time for particles Track velocity and locations of particles Lagrangian multiphase DEM Multiphase interaction
Grid	3D, Hexahedral
Particle size	$D_{10} = 50$ μm, $D_{50} = 200$ μm, $D_{90} = 400$ μm
Fluid	Athabasca oil ($\mu_f = 0.0136$ Pa $\cdot$ s and $\rho_f = 915.2$ $\frac{\text{kg}}{\text{m}^3}$)
Solid	Glass ($\rho = 2800.0$ $\frac{\text{kg}}{\text{m}^3}$, Poisson's ratio = 0.45, Young's modulus = 517000.0 Pa)
Fluid time discretization Scheme	Implicit unsteady
Temporal order of discretization	2nd order
Fluid flow solver	Segregated flow
Velocity solver	Algebraic multigrid (AMG) linear solver
Pressure solver	AMG linear solver
Fluid equation of state	Constant density
Continuous phase	Viscous regime and laminar ($Re_f = 0.0672, Re_p = 0.239, St = 0.009$)
CFD time-step	0.01 s
DEM time-step	0.1 s

Table 4.22 presents the simulation results for four slots. The results presented in Table 4.22 confirmed that there were no remarkable differences between three of the geometries: keystone, WWS and straight slots, from the perspective of arch formation, stabilization, destruction and reformation. For the seamed slot, however, it took the longest for the arch to form and the arch was stable for a shorter time. The seamed slot also took longest for the arch to

reform after breakage. The geometry of the seamed slot is more complex than the others, because the slot opening is curved. The curved edges might cause instability and make it harder for the arch to form and stabilize.

Table 4.22: Various slot geometries: Monitored times (in seconds) for arch formation, breakage and reformation.

	WWS	**Seamed**	**Straight**	**Keystone**
Arch formed	9.02	11.81	9.05	9.15
Arch broke	14.81	14.63	15.52	15.87
Arch reformed	19.31	21.06	21.11	20.86
Stabilization period	5.79	2.82	6.47	6.72
Reformation period	4.5	6.43	5.59	4.99

4.4.8 Stable Packed-Bed: Testing Various Slot Widths and Lengths

Various slot widths and lengths (see Figure 4.20) were tested to investigate their role in the multi-particle arch formation, stabilization, destruction and reformation. Problem setup and condition is similar to the previous stable bed problems. The results are presented in Table 4.23. Where d_p is the particle diameter and time slots were chosen to be 11 DEM time steps (1.1 s).

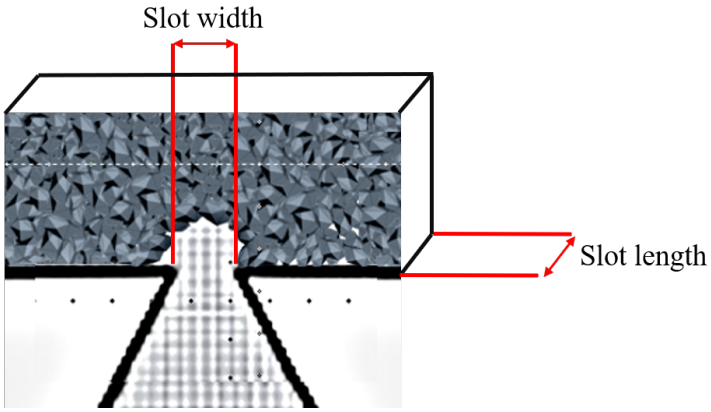

Figure 4.20: Presentation of slot width and length.

Table 4.23: Testing various slot widths to investigate slot width effect on the arch formation, stabilization, destruction and reformation at a WWS slot.

Time	**Cumulative numbers of sand particles passed through the slot in 11 DEM time steps (1.1 s)**	**Slot width**
5-6.1 seconds	11	
9.5-10.6 seconds	9	
12-13.1 seconds	10	$6d_p$
17.3-18.4 seconds	11	
21-22.1 seconds	13	
5-6.1 seconds	9	
9.5-10.6 seconds	10	
12-13.1 seconds	10	$5.5d_p$
17.3-18.4 seconds	8	
21-22.1 seconds	12	
5-6.1 seconds	7	
9.5-10.6 seconds	2	
12-13.1 seconds	0 (arch formation)	$5.25d_p$
17.3-18.4 seconds	4	
23-24.1 seconds	0 (arch reformation)	
6.5-6.6 seconds	7	
8.5-9.6 seconds	5	
12.5-13.6 seconds	0 (arch formation)	$5d_p$
16.4-17.5 seconds	6	
23-24.1 seconds	0 (arch reformation)	
6.5-6.6 seconds	10	
8.5-9.6 seconds	6	
13.0-14.1 seconds	0 (arch formation)	$4d_p$
16.4-17.5 seconds	8	
22-23.1 seconds	0 (arch reformation)	
6.5-7.6 seconds	11	
8.5-9.6 seconds	8	
10.0-11.1 seconds	0 (arch formation)	$3d_p$
15.4-16.5 seconds	7	
22-23.1 seconds	0 (arch reformation)	
6.5-7.6 seconds	6	
8.5-9.6 seconds	5	
10.0-11.1 seconds	0 (arch formation)	$2.75d_p$
15.4-16.5 seconds	5	
22-23.1 seconds	0 (arch reformation)	
5-6.1 seconds	4	
9.5-10.6 seconds	3	
12-13.1 seconds	4	$2.5d_p$
17.3-18.4 seconds	2	
21-22.1 seconds	3	
5-6.1 seconds	3	
9.5-10.6 seconds	2	
12-13.1 seconds	1	$2d_p$
17.3-18.4 seconds	3	
21-22.1 seconds	2	

The results confirmed that for slot widths between $2.75d_p < slotwidth < 5.25d_p$, the multi-particle arch formed. For the slot widths out of this range, no multi-particle arch formed. This result is compatible with the suggested range described in experiments that is $3d_p < slotwidth < 5d_p$ to form the arch[17] and[35].

Additionally, various slot lengths were tested. Results are presented in Table 4.24. The length of the slot had no significant effect on the multi-particle arch formation and stability. In Table 4.24, time periods were chosen to be 11 DEM time steps (1.1 s).

Table 4.24: Testing various slot lengths to investigate the possibility of multi-particle arch formation, stabilization, destruction and reformation (slot width = $4d_p$)

	Numbers of sand particles passed through the slot in 11 DEM time steps (1.1 s)	**Slot length**
6.5-7.6 seconds	10	
8.5-9.6 seconds	6	
13-14.1 seconds	0 (arch formation)	$6d_p$
16.4-17.5 seconds	8	
22-23.1 seconds	0 (arch reformation)	
6.5-7.6 seconds	9	
8.5-9.6 seconds	6	
13-14.1 seconds	0 (arch formation)	$5d_p$
16.4-17.5 seconds	9	
22-23.1 seconds	0 (arch reformation)	
6.5-7.6 seconds	11	
8.5-9.6 seconds	6	
13-14.1 seconds	0 (arch formation)	$4d_p$
16.4-17.5 seconds	8	
22-23.1 seconds	0 (arch reformation)	
6.5-7.6 seconds	10	
8.5-9.6 seconds	6	
13-14.1 seconds	0 (arch formation)	$3d_p$
16.4-17.5 seconds	9	
22-23.1 seconds	0 (arch reformation)	
6.5-7.6 seconds	10	
8.5-9.6 seconds	6	
13-14.1 seconds	0 (arch formation)	$2d_p$
16.4-17.5 seconds	8	
22-23.1 seconds	0 (arch reformation)	

4.4.9 Response to Transient Flow and Comparison with Experiment

The last problem studied with the stable packed-bed was investigation of the effect of time-dependent boundary conditions of the flow on the multi-particle

arch behaviour. The response of the multi-particle arch to time-dependent boundary conditions of the flow is discussed in this section. The response of the arch refers to the following: does the arch break and reform after sudden changes in the velocity of the fluid flow?

Figure 4.21 shows the schematic of a slotted liner with no flow control device where a single slot was magnified as the study domain. Sample time-dependent boundary conditions, that could be representative of the transient flow in the pipe, plotted as changes in pressure with time. The schematic of the bridge destruction under transient boundary condition (back pressure) is also presented in the right side of the figure.

Figure 4.22 shows fluid domain of a single slot under given boundary conditions. Time-dependent fluid flow-rate can be set as a time-dependent velocity boundary condition at the inlet of the slot that is the case studied here. Time-dependent conditions (such as the periodic pressure change in the outlet) could be equivalent to phenomena in the well-bore, such as vibrational flow and water hammer.

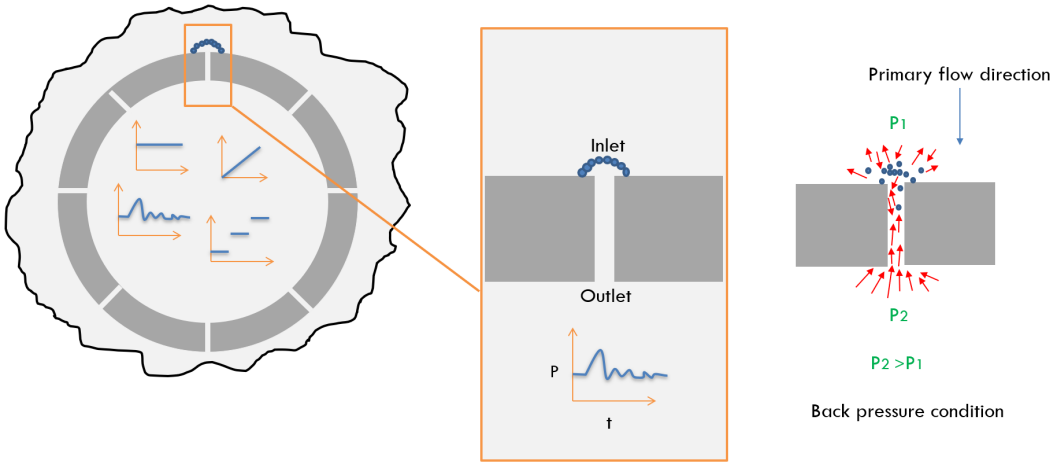

Figure 4.21: Presentation of well-bore, a magnified single slot, the transient condition in the pipe and back pressure state.

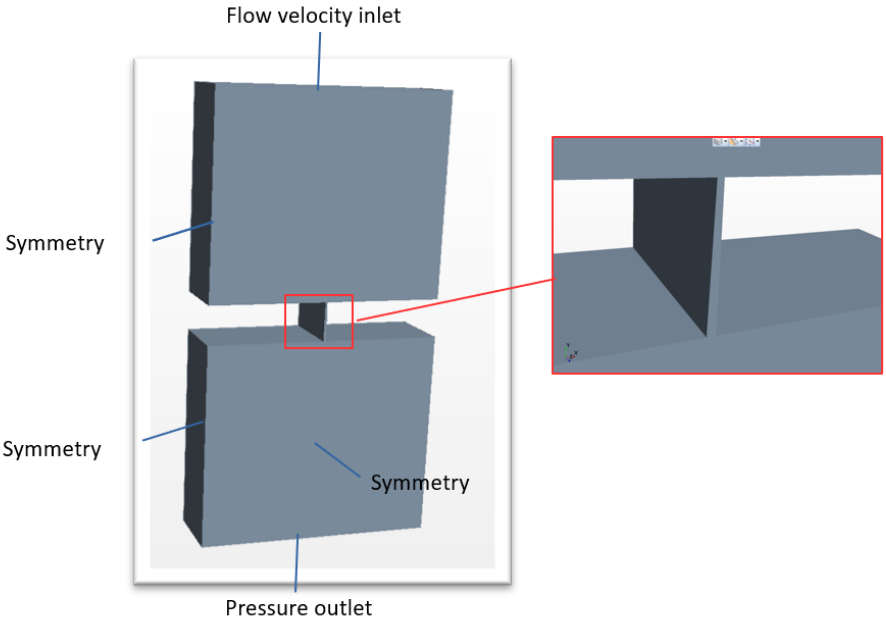

Figure 4.22: Fluid domain of a single keystone slot and the assigned boundary conditions.

In the coming sections, two sand retention test (SRT) problems were

simulated by the CFD-DEM model. There is SRT experimental results available as the reference to compare the simulation results with.

SRT Experiment by Wang et al.[3] and[4]

The SRT experimental testing facility was designed to replicate conditions of the sand-pack around a SAGD well, including stress load on the sand particles. The SRT cells includes the sand-pack, a multi-slot coupon, and weight to provide a stress load on the particles. Sand is collected in a sand trap located after the slots[35], and[37]. The experiment started with the constant flow rate through the sand-pack. The water valve was closed after 4 hours and water flow in the sand-pack was interrupted for 3 minutes to collect produced sands. The water valve was opened again to allow water flow into the sand-pack for 5, 10, 20 and 33 minutes, respectively. Flow interruption time was three minutes for all cases, Table 4.25. The important point is that, while the water valve was closed, the water flow into the sand-pack was interrupted. As a result, there was no drag force on the particles in the sand-pack, and the multi-particle arch broke possibly due to relieved stress load during no-flow. Water flow rate used at different time slots in the experiment was constant as shown in Figure 4.23.

Table 4.25: Sands collected from SRT experiment following arch destruction

Time that SRT experiment is running while water flow is interrupted	**Amount of the collected sand**
4-hour of SRT experiment	Sands collected = A
4-hour + 5 minutes of SRT	approximately $\frac{1}{10}$ of the previous scenario = $\frac{1}{10} \times A$
4-hour + 10 minutes of SRT	approximately $\frac{1}{4}$ of the previous scenario = $\frac{1}{4} \times \frac{1}{10} \times A$
4-hour + 20 minutes of SRT	approximately $\frac{1}{4}$ of the previous scenario = $\frac{1}{4} \times \frac{1}{4} \times \frac{1}{10} \times A$
4-hour + 33 minutes of SRT	approximately $\frac{1}{4}$ of the previous scenario = $\frac{1}{4} \times \frac{1}{4} \times \frac{1}{4} \times \frac{1}{10} \times A$

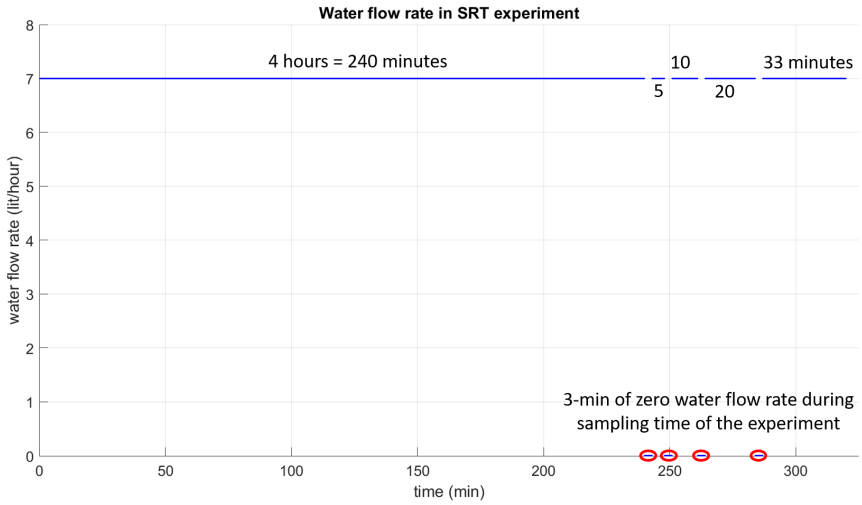

Figure 4.23: Water flow rate applied at different time slots in the SRT experiment by Chenxi[3] and[4]

The amount of the sand, produced during interruptions, was collected and assessed qualitatively as presented in Table 4.25. According to Table 4.25, when the flow was interrupted the multi-particle arch was broken and consequently, some sands produced. Following each fluid flow interruption period, the fluid valve was reopened at the same flow rate, multi-particle arch reformed after a while and destructed again by another fluid flow interruption. This was what

observed in the SRT experiment.

Simulation Plan: Constant Flow Rate and Variable Fluid Velocities

The objective of this study was to simulate of the above process by CFD-DEM simulation and to ensure that the CFD-DEM model was capable of predicting multi-particle arch behavior under transient condition of the fluid flow. Due to computational limitations, the time scale for the simulations was different than the observed experiment. The transient fluid flow rate in the experiment was equivalent to the transient flow velocity inlet in the simulation.

The time scale for the replication of the SRT experiment was chosen based on the best practices obtained through numerous numerical simulations. After the arch forms in order of seconds, there is no need to let the simulation run for longer, as there will be no obvious changes and it wastes computational resources.

Here are the simulation phases conducted:

1. Run the simulation (at fluid velocity inlet 0.001 $\frac{\mathrm{m}}{\mathrm{s}}$) as long as the multi-particle arch was formed and track the numbers of particles passed through the slot as well as track the particles locations (30 seconds).

2. Run the simulation for 1 second with frozen fluid solver at fluid velocity inlet 0 $\frac{\mathrm{m}}{\mathrm{s}}$ (1 second).

3. Similar to phase 1: run the simulation (at fluid velocity inlet 0.001 $\frac{\mathrm{m}}{\mathrm{s}}$) as long as the arch was formed and track the numbers of particles passed through the slot as well as track the particles locations (10 seconds).

4. Similar to phase 2: run the simulation for 1 second with frozen fluid solver at fluid velocity inlet 0 $\frac{\text{m}}{\text{s}}$ (1 second).

5. Similar to phases 1 and 3: run the simulation (at fluid velocity inlet 0.001 $\frac{\text{m}}{\text{s}}$) as long as the arch was formed and track the numbers of particles passed through the slot as well as track the particles locations (9 seconds).

6. Similar to phases 2 and 4: run the simulation for 1 second with frozen solver at fluid velocity inlet 0 $\frac{\text{m}}{\text{s}}$ (1 second).

Table 4.26 presents the mathematical and computational settings for this transient problem. Figure 4.24 presents the arch formation, breakage and reformation phases in the transient case having the fluid flow on and off.

Table 4.26: Mathematical and computational model setup for SRT simulation

	Setup
Continuous phase equations	Continuity and NS equations
Fluid phase boundary condition	Top face: transient velocity inlet =0.001 $\frac{\mathrm{m}}{\mathrm{s}}$, $Re_f = 0.0672$
Fluid phase boundary condition	Other faces: no-slip wall
Fluid initial condition	Quiescent
Discrete phase equations	Newton's 2nd law of motion (conservation of linear and angular momentum)
Particle boundary condition	No-slip wall
Particle initial condition	Terminal velocity = 0.0097 $\frac{\mathrm{m}}{\mathrm{s}}$
Coupling scale	Smoothed Unresolved
Coupling technique	Two-way coupling
Particle type	DEM particles, Polyhedral
Solid particle material	Glass (solid, sand-like)
Forces	Pressure gradient force (counts for the buoyancy) Drag force Gravity Interaction forces Lift forces Virtual mass force
DEM model setting	Residence time for particles Track velocity and locations of particles Lagrangian multiphase DEM Multiphase interaction
Grid	3D, Hexahedral
Particle size	$D_{10} = 50$ μm, $D_{50} = 200$ μm, $D_{90} = 400$ μm
Fluid	Athabasca oil ($\mu_f = 0.0136$ Pa $\cdot$ s and $\rho_f = 915.2$ $\frac{\mathrm{kg}}{\mathrm{m}^3}$)
Solid	Glass ($\rho = 2800.0$ $\frac{\mathrm{kg}}{\mathrm{m}^3}$, Poisson's ratio = 0.45, Young's modulus = 517000.0 Pa)
Fluid time discretization Scheme	Implicit unsteady
Temporal order of discretization	2nd order
Fluid flow solver	Segregated flow
Velocity solver	Algebraic multigrid (AMG) linear solver
Pressure solver	AMG linear solver
Fluid equation of state	Constant density
Continuous phase	Viscous regime and laminar (at slot $Re_f = 0.0672, Re_p = 0.239, St = 0.009$)
CFD time-step	0.01 s
DEM time-step	0.1 s

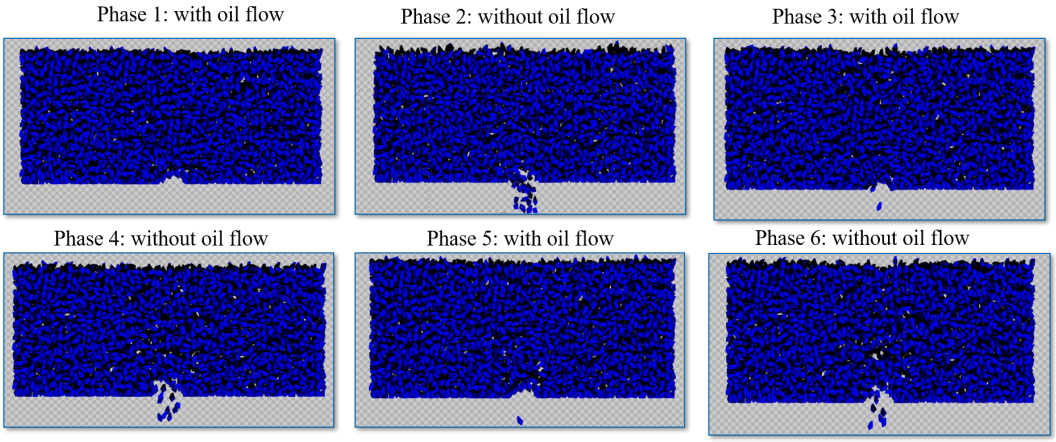

Figure 4.24: Arch formation, breakage and reformation phases in the transient case having the fluid flow on and off.

The objective was to investigate the multi-particle arch formation, stabilization, destruction and reformation under these transient conditions. During the fluid flow interruption time (phases 2 and 4), the velocity of the fluid was zero due to lack of movement of the fluid in the stable sand-pack. The drag force was omitted, which was done by freezing the fluid solver in the simulation. Without drag force, multi-particle arch experienced a shock and broke (phases 2, 4 and 6). The simulation ran with the fluid flow till the new multi-particle arch formed (phases 1, 3 and 5). The numbers of particles passing through the slot were tracked.

The simulation results are presented in Table 4.27. In Table 4.27, various time slots were chosen to be 10 time steps. The cumulative numbers of sand particles passed the slot are presented in Table 4.27. It can be observed from the number of the sand particles passed the slot that the multi-particle arch was formed at 24.9 s in phase 1 where there was no more particles passed the

slot. After 30 seconds, the fluid flow was interrupted in phase 2 and there were 19 particles passing through the slot in 1 second which was a sign of multi-particle arch destruction due to fluid flow interruption.

After 31 seconds, phase 3 started, fluid flowed again in the stable packed bed and arch reformation occurred at 38 seconds. In phase 4, the fluid flow was interrupted at 41 seconds, arch was broken and sands produced. In phase 5, with the restart of the fluid flow, arch formed at 48 seconds and the last phase was similar to phases 2 and 4, where there was no fluid flow in the sand pack and arch was broken.

The pattern of sand production observed in the SRT simulation was similar to the SRT experiment. The decreasing trend of the numbers of the particles passed the slot in the flow interruption periods (numbers 19, 11 and 7 in Table 4.27) is also similar to the decreasing trend of sand production in the experiment presented in Table 4.25. This could confirm that the CFD-DEM model simulation was capable of simulating the arch formation, stabilization, destruction and reformation under transient condition. The multi-particle arch behavior, while the constant fluid flow was interrupted, was interesting. The multi-particle arch broke due to fluid interruption and possibly the lack of the drag force. This is a valuable finding as it highlights the role of the drag force and particle-fluid interaction force in sustaining the stability of the multi-particle arch. In this section, the SRT simulation ran with the constant flow rates in various time slots in the packed bed, when the valve was open.

Table 4.27: Sands collected in SRT simulation phases (WWS)

SRT phases	**SRT simulation time**	**Cumulative numbers of sand particles passed the slot**
Phase 1	6-7 second	15
	8.3-9.3 second	16
	10.7-11.7 second	11
	11.3-12.3 second	13
	12.7-13.7 second	7
	13.1-14.1 second	3
	14.1-15.1 second	4
	18.5-19.5 second	2
	20.5-21.5 second	2
	22.3-23.3 second	1
	23.7-24.7 second	2
	24.9-25.9 second	0 (arch formed)
	25.7-26.7 second	0
	26.5-27.5 second	0
	27.2-28.2 second	0
	27.9-28.9 second	0
	29-30.0 second	0
Phase 2	flow interruption time 30-31 second no drag force	19 (arch destructed)
Phase 3	31.8-32.8 second	14
	33-34 second	11
	34.2-35.2 second	7
	35.5-36.5 second	9
	36.5-37.5 second	3
	38-39 second	0 (arch reformed)
	39-40 second	0
	40-41 second	0
Phase 4	flow interruption time 41-42 second no drag force	11 (arch destructed)
Phase 5	42-43 second	13
	43-44 second	10
	44.2-45.2 second	11
	45.5-46.5 second	8
	46.5-47.5 second	2
	48-49 second	0 (arch reformed)
	49-50 second	0
	50-51 second	0
Phase 6	flow interruption time 52-53 second no drag force	7 (arch destructed)

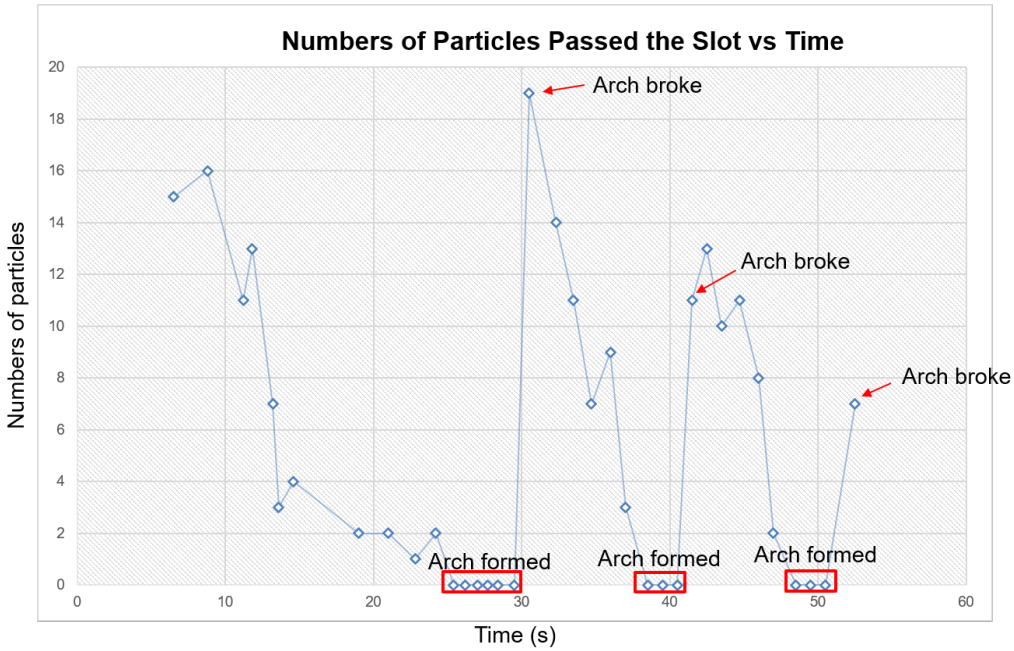

Figure 4.25: Plot of sands collected in SRT simulation phases (WWS). Decreasing trend of the numbers of particles passing through the slot for the 3 periods of arch breakage. It is in agreement with the SRT experiment by Chenxi from Dr. Nouri's lab.

SRT Simulation with Variable Flow Rates

In this case, after interrupting the fluid flow and collecting sand samples for 1 second, the valve was opened to allow fluid flow into the sand-pack again at flow rates double the previous flow rate value, respectively. Flow interruption time was 1 second for all cases to collect sands. Following each fluid flow interruption, the fluid valve was reopened at a higher flow rate.

Simulation Plan: Variable Flow Rate To simulate the above process by the CFD-DEM model, the transient fluid flow rate was considered to be equivalent to the transient flow velocity inlet in the simulation domain.

Here are the SRT simulation phases conducted to investigate this problem:

1. Run the simulation (at fluid velocity inlet 0.001 $\frac{\text{m}}{\text{s}}$, $Re_f = 0.0672$) as long as the multi-particle arch was formed and track the numbers of particles passed through the slot as well as track the particles locations.

2. Run the simulation for 1 second with frozen solver at fluid velocity inlet 0 $\frac{\text{m}}{\text{s}}$.

3. Run the simulation (at fluid velocity inlet 0.002 $\frac{\text{m}}{\text{s}}$, $Re_f = 0.1344$) as long as the multi-particle arch was formed and track the numbers of particles passed through the slot as well as track the particles locations.

4. Run the simulation for 1 second with frozen solver at fluid velocity inlet 0 $\frac{\text{m}}{\text{s}}$.

5. Run the simulation (at fluid velocity inlet 0.003 $\frac{\text{m}}{\text{s}}$, $Re_f = 0.2016$) as long as the multi-particle arch was formed and track the numbers of particles passed through the slot as well as track the particles locations.

During the fluid flow interruption time (phases 2 and 4), the velocity of the fluid was zero due to the lack of fluid movement in the stable sand-pack. Accordingly, the drag force was omitted, which was done by freezing the fluid solver in the simulation. Without drag force, multi-particle arch experienced a shock and broke (phases 2 and 4). The simulation ran with a different fluid flow till the new multi-particle arch formed (phases 1, 3 and 5). The numbers of particles passing through the slot were tracked.

The simulation results are presented in Table 4.28. In Table 4.28, various time slots of 0.1 s were chosen for observation. The cumulative numbers of sand particles passing the slot are presented in Table 4.28. It can be observed from the number of the sand particles passed the slot that the multi-particle arch was formed at the 24.9 s mark in phase 1 after which there was no more particles passing the slot. At the 30 seconds mark, the fluid flow was interrupted in phase 1 and there were 19 particles passed through the slot which was a sign of multi-particle arch destruction. After 31 seconds, phase 3 started, fluid flowed again in the sand pack at a higher flow rate as twice as the initial flow rate in the stable packed bed and arch reformation occurred at 41 seconds (later than the phase 3 of the previous case). In phase 4, the fluid flow was interrupted at 44 seconds, arch was broken and sands produced. In phase 5, with the tripled fluid flow rate arch did not form till the end of the simulation 57 seconds mark. This could have happened due to higher fluid flow rate in comparison with the phase 5 of the previous SRT test simulation with constant fluid flow rate.

Table 4.28: Sands collected in SRT simulation phases with variable fluid flow rates

SRT phases	**SRT simulation time**	**Cumulative numbers of sand particles passed the slot**
Phase 1	6-7 second	15
	8.3-9.3 second	16
	10.7-11.7 second	11
	11.3-12.3 second	13
	12.7-13.7 second	7
	13.1-14.1 second	3
	14.1-15.1 second	4
	18.5-19.5 second	2
	20.5-21.5 second	2
	22.3-23.3 second	1
	23.7-24.7 second	2
	24.9-25.9 second	0 (arch formed)
	25.7-26.7 second	0
	26.5-27.5 second	0
	27.2-28.2 second	0
	27.9-28.9 second	0
	29-30.0 second	0
Phase 2	interruption time 30-31 second no drag force	19 (arch destructed)
Phase 3	31.8-32.8 second	16
	33-34 second	12
	34.2-35.2 second	9
	35.5-36.5 second	11
	36.5-37.5 second	6
	38-39 second	7
	39-40 second	5
	40-41 second	2
	41-42 second	2
	41.8-42.8 second	0 (arch reformed)
	43-44 second	0
Phase 4	interruption time 44.2-45.2 second no drag force	15 (arch destructed)
Phase 5	45.5-46.5 second	16
	46.5-47.5 second	20
	48-49 second	14
	49-50 second	11
	51-52 second	12
	52-53 second	9
	53.6-54.6 second	8
	55-56 second	9
	56-57 second	11

It was observed that at the higher flow rate, more sand particles were produced in comparison with the constant flow rate SRT.

4.4.10 Results and Discussion

Following the research conducted on the sand retention mechanisms specifically multi-particle arch formation, stabilization, destruction and reformation in the slurry cases and unstable packed bed cases, the final part of this thesis was about transient cases in the stable packed bed to explore the physics behind arching. The effect of various parameters and conditions on the multi-particle arch formation, stabilization, destruction and reformation were studied with a stable packed bed of particles.

The following is the list of findings that were observed:

1. In all cases of different fluids (Table 4.14), the multi-particle arch formed with/without fluid, broke after a period of time and reformed, and this pattern continued, similar to the unstable packed bed.

2. The multi-particle arch formed even without fluid. In this case, the arch formed faster. However, it stayed stable for a shorter time and reformed more quickly after breakage. The particle-particle interaction force and the gravity force again played key roles in multi-particle arch formation and the particle-fluid interaction forces were not essential for the arch formation.

3. Compared to the unstable packed bed case, multi-particle arch stayed stable for a longer time and the number of the particles passing through

the slot, following multi-particle arch formation, was less in the case of stable packed bed.

4. With non-spherical particles, the multi-particle arch formed faster, and it reformed faster after breakage. stayed stable for a longer time than the case with spherical particle. For non-spherical particles with higher aspect ratio, the arch was less stable than the arch formed with the polyhedral case with the lower aspect ratio.

5. With polyhedral particle size distribution at micro-scale, the initial formation of the arch took longer than the case with the uniform-size distribution, and the multi-particle arch stayed stable for a longer time than the uniform cases (both polyhedral and spherical). Following breakage, it took longer to reform the arch compare to the uniform-size cases, however, the reformation took shorter than the unstable packed bed case as happened with the unstable packed bed.

6. There were fewer particles passing through the slot during the stabilization period. This was the main difference between the stabilization period in stable and unstable packed bed cases.

7. Gravity force and interaction forces are essential forces to form the multi-particle arch at micro-scale. Without other forces (fluid drag force, lift forces, buoyancy, cohesive force, fluid-particle interaction force, virtual mass force) multi-particle arch formed, stayed stable, broke and reformed.

8. The increased height of the unconsolidated region resulted in increased

stress over the slot region. The stress load was increased further with the use of large and heavy particles. As the stress load increased, the arch formed faster, it was stable for a longer period and it took shorter for the arch to reform compared with the cases with lower stress load.

9. The CFD-DEM model simulation was capable of simulating the arch formation, stabilization, destruction and reformation under transient condition of flow domain. The SRT simulation and the experiment follow similar decreasing trend of sand particles passing through the slot after arch destruction due to fluid flow interruption.

10. The arch behavior while the constant fluid flow was interrupted was very revealing. It was clear that the arch broke due to the lack of the drag force when the flow was interrupted, showing that transient flow conditions can destabilize the multi-particle arch. This is a valuable insight provided by the current investigation at the micro-scale.

11. Slurry flow is too diluted for multi-particle arch formation at the opening.

12. Stress from the packed-bed is necessary to form the arch.

13. Stable packed-bed supports arch formation and stability.

14. High viscosity of fluid supports arch stability.

15. Aspect ratio larger than 1 supports arch formation and stability.

16. Particle size distribution supports arch stabilization.

17. Larger stress supports arch formation and stabilization.

18. Curved slot is not the best geometry choice for arch formation and stability.

19. Length is not a critical designing factor from the perspective of arch performance.

Considering the investigation and research on the numerical simulation of retention mechanisms, under the effects of conditions and parameters involved, a good understanding of the multi-particle arching phenomenon and the relevant physical aspects was achieved. The study provides insight into which parameters and conditions could affect arch formation, stabilization, destruction and reformation and the effect of parameters such as: size and shape of the particles, particle concentration, existence of porous media, transient flow velocity, particle size distribution, viscosity of fluid and geometry of the slot. This research provides the researchers with the platform to investigate this phenomenon further in the well-bore and add to this knowledge to improve the criteria for selecting the sand screen devices and possibly suggesting an improved design for slot openings, which supports the arch formation and stabilization. This design and improved criteria would be of high value for the industry.

Chapter 5

Conclusion

This final chapter gives a summary of the findings of this thesis. At the end of this chapter, potential future work will be discussed. The first phase of this work involved setting up a numerical model and conducting a rigorous verification and validation of the model to assure that the model was predictive from the perspective of particle-particle, particle-wall and particle-fluid interactions. Literature was investigated to apply the particulate-flow modeling approach at micro-scale considering the computational resources. It was found that by the CFD-DEM model, the collision of hundreds of particles and the inter-particle forces could be simulated. The CFD-DEM models were set up and validated from the perspectives of particle-particle, particle-wall and particle-fluid interactions with the benchmark problems as well as the available experimental work from the collaborating labs and literature.

Following the verification (mesh independence analysis) and validation practices, a list of best practices was achieved to setup the model and study

particulate flow at filter opening as follows:

1. A mesh should get designed in a way that gives adequate resolution in regions where spatial gradients are high, such as slot entrance. Considering the computational cost and accuracy, the best practices mesh-resolution for a steady state particulate flow case was achieved by smoothed unresolved (refined grid unresolved) coupling where the size of the particle was at least as twice as the mesh size. Also, mesh-resolution for a transient particulate flow case was achieved by smoothed unresolved (refined grid unresolved) coupling where the size of the particle was at least five times larger than the mesh size. The quality of the robust simulation model guaranteed by grid independence and error estimation.

2. Second order time discretization was preferred, and a spatial discretization that was based on second-order upwind differencing scheme.

3. The segregated solver was preferred to the coupled solver for transient cases considering the accuracy and the computational cost.

4. Freezing the solvers helped initial simulation stability, computational efficiency, and reducing total run time specifically early in the simulation. Convergence issues could arise because of the lack of a good physical initial condition for transient simulations.

5. It was revealed that Young modulus lower than the actual one could reduce simulation time as DEM time-step was dependent on Young modulus. A reduction up to three order of magnitudes could be applied

with sensitivity analysis.

6. Hertz-Mindlin contact model could predict well how particles interact during the collision.

7. The boundary condition is set at continuum level by default and had to setup for each individual boundary of particles.

8. Maximum porosity could be specified as limit after which injection of new particles is stopped. This feature could help building the porous regions with particles.

9. Two-way coupling is recommended to study retention mechanisms where each phase is affected by the other phase for example if drag force is included in the simulation, a momentum source is added to the continuous phase.

10. Volume fraction of disperse phase in the continuous phase is dependent on cell size where maximum volume fraction is 1.0 in case of having larger particles than cells. Solution could be unstable if the disperse phase produces high sources of momentum. Sources could be smeared/smoothed in more cells through DEM solver to avoid instability. It was achieved that the maximum volume fraction specified in the simulations in case of smoothed unresolved coupling was 0.98. Using 1.0 resulted in instability of the simulations.

11. The CFD-DEM model by applying the soft-sphere model was predictive. In the the soft-sphere model, particles could overlap but not deform. The

soft-sphere formulation is based on the contact forces that are established during a contact between particles. In this model, contact force is proportional to the overlap and multiple contacts are allowed at the same time.

Following validation of the CFD-DEM model, numerous scenarios planned to investigate the possibility of arch formations by modeling the slurry flow with different test conditions. Size exclusion, surface deposition and sequential arching were observed as retention mechanisms. Multi-particle arching phenomenon did not occur with the slurry flow in various types of sand screen's openings. These results occurred even for a narrow slot. The slurry flow could be considered as the initial phase followed by formation of loosened packed bed called unconsolidated packed bed in the gap between the sand filter and the oil-sand reservoir. The investigation on slurry cases lead to the fact that the stress from the packed bed of solid particles on top of the slot opening was essential to form the multi-particle arch[71], [72] and [73]. It was clear from the majority of the simulated slurry scenarios that the concentration of the particles was too diluted to result in multi-particle arch formation and the stress of the packed bed of particles was essential for the multi-particle arch formation.

Following the research done on the slurry flow, the multi-particle arch formation was studied using an unstable packed bed. The reason to instability of the bed was that the slot was open while the sand particles were continuously injected into the packed bed. In this case, particles did not get a chance to make a settled packed bed due to perturbation resulted from the continuous

injection of particles. The simulations with the unstable packed bed resulted in several indications of relevant parameters and conditions that impact multi-particle arch formation, stabilization, destruction and reformation, such as the effect of the physical forces, shape and size of the particles, and reservoir load. But it was clear that the instabilities caused by the numerical setup did not correspond to the physical flow that was being investigated.

The period of time that the multi-particle arch was stable was relatively brief, and the pattern of arch formation, stabilization, destruction and reformation repeated many times. Study the effect of various parameters was useful to indicate which conditions/parameters supported arch formation and stability, such as the increased height of the packed bed region, the non-spherical shape of the particles and the non-uniform-size distribution. A true predictive simulation required a method of modeling a stable packed bed.

In the next phase of the research, a study was conducted on the stable packed bed to investigate the multi-particle arch formation, stabilization, destruction and reformation. In order to achieve stability of the packed bed, the particles were first allowed to settle, while the slot was kept closed. The slot was only opened and the flow started after the particles were settled and no further particles were added. This resulted in a stable packed bed that allowed for the detailed investigation under steady and transient flow conditions. As a result of the stable packed bed model, there were fewer particles passing through the slot during the stabilization periods. This was the main difference between the stabilization period in stable and unstable packed bed cases.

Here is the list of findings that were observed:

1. Without fluid, the multi-particle arch formed faster. However, it stayed stable for a shorter time and reformed more quickly after breakage. The particle-particle interaction force and the gravity force played key roles in multi-particle arch formation. The particle-fluid interaction forces (fluid drag force, buoyancy, virtual mass force) and the lift and cohesive forces could be neglected at this scale and the multi-particle arch still formed, stayed stable, broke and reformed, revealing them as not essential for arch formation.

2. The following factors supported the multi-particle arch to form faster and to stay stable for a longer time:

   (a) Polyhedral particles performed better than spherical particles. However, the lower aspect ratio ($AR = 1.6$) particles performed better than the higher aspect ratio ($AR = 2.3$) particles.

   (b) With polyhedral particles with PSD, the multi-particle arch stayed stable for a longer time than with the uniform cases (both polyhedral and spherical). However in the PSD case, it took longer for the arch to form initially and it also took longer to reform the arch compared to the uniform-size cases. There are both supportive and non-supportive aspects of having PSD on arch formation and stability.

   (c) With increasing the stress over the slot region, represented by an increased height of the packed bed or by the addition of large/heavy particles, the arch formed faster and it was stable for a longer period

of time. It also took shorter for the arch to reform after breakage as the stress load was increased.

3. The performance comparison between four types of slots with different slot widths provided partial validation of the sand retention simulation results:

   (a) The filtration efficiency of various slot widths was in good agreement with the slot dimensions recommended by the sand retention test (SRT) experiment.

   (b) The seamed slot showed lower arch stability and longer time of arch formation than the keystone, straight and WWS slots. The curved shape of the seamed slot could be a justification for this arch performance.

Following the research conducted on the sand retention mechanisms in stable packed bed having steady flow, the final part of this thesis was about simulation of the transient cases and investigation of the performance of the arch under transient flow condition.

The main findings of transient flow simulations are provided as following:

1. The CFD-DEM model simulation was capable of simulating the arch formation, stabilization, destruction and reformation under transient flow condition. The SRT simulation and the experiment follow similar decreasing trend of sand particles passing through the slot after arch destruction due to fluid flow interruption.

2. The arch behavior, while the constant fluid flow was interrupted, revealed the interesting finding that the arch broke due to the interruption of the flow and lack of the drag force at micro-scale.

The key contributions of the present research, that improved the understanding of the arching phenomenon as an efficient sand retention mechanism, are summarized as follows:

1. The computational fluid dynamic (CFD)- discrete element method (DEM) model is capable of predicting multi-particle arch formation, stabilization, breakage and reformation under steady and transient conditions of the well-bore.

2. Multi-particle arching does not occur at the slot opening in the slurry flow even for a narrow slot with the width equal to $2d_p$. To form a multi-particle arch, particles should get at the entrance of the slot simultaneously. This is the main difference between sequential arching (which occurs in the slurry flow) and multi-particle arching.

3. The load stress from the packed bed of solid particles on top of the slot opening is essential to form the multi-particle arch. The increased stress results in multi-particle arch formation/reformation in a shorter time and arch stabilization for a longer time, that is, improved sand retention.

4. Two forces were critical to forming the multi-particle arch: gravity force and interaction forces between the particles and particle-domain at the micro-scale.

5. In the numerical simulations, three retention mechanisms at filter openings were achieved: surface deposition, size exclusion and multi-particle bridging. In the cases with the porous region, surface deposition, sequential bridging and size exclusion were also achieved at pores.

6. Particle size distribution supports the multi-particle arch and it stays stable for a longer time than the case with the uniform-size distribution.

7. Particle shape affects the arch stability. Non-spherical particles with sharp corners result in a more stable arch, but aspect ratio should not be too large.

8. A stable packed bed supports stabilization of the multi-particle arch. Instabilities caused by transient flow changes, such as flow interruptions, can result in arch breakage and increased sand production.

9. The results showed that multi-particle arching was the result of particle interaction and surface deposition at the slot entrance. The ratio of the particle size to the sand screen opening was an important factor in arch formation. A curved surface at the slot entrance, such as the modeled seamed slot shape, can result in lower arch stability and larger sand production.

5.1 Future Work

Finally, areas for further research were identified.

1. Calculate and add the stress of the reservoir based on the soil mechanics to the model and investigative its effect on arching.

2. Include other reservoir fluids in the multi-phase simulations including water, steam and gas and study arching further considering multi-phase fluid flow.

3. Consider energy equation and temperature changes in the simulations and study arching with respect to temperature alteration.

4. Explore the effect of multiple slots on arch formation and stabilization.

5. Undertake further investigation of the bridge stability and destabilization under various transient conditions of the well-bore such as vibrational flow and water hammer.

6. Undertake further exploration of the range of the screen opening size where stable bridging occurs.

7. Investigate different screen opening designs with various geometries that could improve plugging prevention and support the multi-particle arch formation and stabilization.

8. Explore these problems by using the openFOAM (non-commercial software) and investigate the possibility of applying deep learning and grid-free CFD to suggest a new efficient design for filter opening that supports arching.

Bibliography

[1] Lisa Kinsale and David S Nobes. The study of flow through porous media within the near-slot region of SAGD operations using PSV. *5th Int. Conf. Exp. Fluid Mech. – ICEFM 2018 Munich, Munich, Ger. July 2-4, 2018*, pages 1–6, 2018.

[2] Lisa K. Kinsale, Mohammad A. Kazemi, Janet A.W. Elliott, and David S. Nobes. Transportation and deposition of spherical and irregularly shaped particles flowing through a porous network into a narrow slot. *Exp. Therm. Fluid Sci.*, 109(July):109894, 2019.

[3] Chenxi Wang, Yu Pang, Mahdi Mahmoudi, Mohammad Haftani, Mahmoud Salimi, Vahidoddin Fattahpour, and Alireza Nouri. A set of graphical design criteria for slotted liners in steam assisted gravity drainage production wells. *J. Pet. Sci. Eng.*, 185, 2020.

[4] Chenxi Wang, Jesus D. Montero Pallares, Mohammad Haftani, and Alireza Nouri. Protocol for optimal size selection of punched screen in Steam Assisted Gravity Drainage operations. *J. Pet. Sci. Eng.*, 196(January 2020):107689, 2021.

[5] Siemens PLM. STAR-CCM +® Documentation. 2016.

[6] Hamid Reza Norouzi, Reza Zarghami, Rahmat Sotudeh-gharebagh, and Navid Mostoufi. *Coupled CFD - DEM Modeling and Application to Multiphase Flows*. WILEY, 2016.

[7] Siemens. Simcenter STAR-CCM + Product Overview. 2019.

[8] George King. Sand Control Methods. *Georg. E. King Eng.*, 2009.

[9] Y Kawamura and Y Kobayashi. Basic Study on Application of Discrete Element Method for Slope Failure Analysis. *Proceeding 15th world Conf. Earthq. Eng.*, 2012.

[10] Cheng Peng, Orlando M. Ayala, and Lian-Ping Wang. A direct numerical investigation of two-way interactions in a particle-laden turbulent channel flow. *J. Fluid Mech.*, 875:1096–1144, 2019.

[11] Wim-paul Breugem. A Combined Soft-Sphere Collision / Immersed Boundary Method for Resolved Simulations Of Particulate Flows. 2010.

[12] J. C. Brändle de Motta, J. L. Estivalezes, E. Climent, and S. Vincent. Local dissipation properties and collision dynamics in a sustained homogeneous turbulent suspension composed of finite size particles. *Int. J. Multiph. Flow*, 85:369–379, 2016.

[13] Dominique Legendre, Roberto Zenit, Claude Daniel, and Pascal Guiraud. A note on the modelling of the bouncing of spherical drops or solid

spheres on a wall in viscous fluid. *Chem. Eng. Sci.*, 61(11):3543–3549, 2006.

[14] Maurice Dusseault and F.J. Santarelli. A conceptual model for massive solids production in poorly-consolidated sandstones. *ISRM Int. Symp.*, pages 789–797, 1989.

[15] Jamie Stuart Andrews, Statoil Stavanger, Joseph A Ayoub, Rajesh A Chanpura, Somnath Mondal, and Mukul M Sharma. Sand Screen Selection. *Oilf. Rev.*, 27(2), 2015.

[16] Jon Carlson, Gurley Derrel, Price-smith Colin, and Waters Frank. Sand Control: Why and How? *Oilf. Rev.*, October:41–53, 1992.

[17] CJ Coberly. Selection of Screen Openings for Unconsolidated Sands. *Drill. Prod. Pract.*, pages 37–189, 1938.

[18] Vahid Fattahpour, Mahdi Mahmoudi, Alireza Nouri, Saman Azadbakht, Michael Leitch, Brent Fermaniuk, and Colby Sutton. A Critical Review of Sand Control Design for SAGD Wells. *World Heavy Oil Congr. 2016*, (September):1–13, 2016.

[19] Sanjay Vitthal and Mukul M. Sharma. A Stokesian dynamics model for particle deposition and bridging in granular media. *J. Colloid Interface Sci.*, 153(2):314–336, 1992.

[20] Mahdi Mahmoudi Eshkaftaki. New Sand Control Design Criteria and

Evaluation Testing for Steam Assisted Gravity Drainage (SAGD) Wellbores. *PhD Thesis*, 2017.

[21] E. Loth. Drag of non-spherical solid particles of regular and irregular shape. *Powder Technol.*, 182(3):342–353, 2008.

[22] Julio R. Valdes and J. Carlos Santamarina. Clogging: bridge formation and vibration-based destabilization. *Can. Geotech. J.*, 2008.

[23] Xavier Choi Yuqing Feng. Evaluation of Sand Screen Performance using a Discrete Element Model. 2012.

[24] Jeffrey S. Marshall and Shuiqing Li. *Fluid Forces on Particles*. 2014.

[25] Fuat Odar and Wallis S. Hamilton. Forces on a sphere accelerating in a viscous fluid. *J. Fluid Mech.*, 18(2):302–314, 1964.

[26] Tushar Shani and Tinish Gupta. Hydraulic Transient Flow Analysis. pages 14812–14827, 2017.

[27] Jacob Bear. *Advances in Transport Phenomena in Porous Media*. Published in corporation with NATO Scientific Affairs Division, 1987.

[28] P. Risnes, R., Bratli, R.K., y Horsrud. Sand Stresses Around a Wellbore. *Soc. Pet. Eng. J.*, 22(6):883–898, 1982.

[29] Julio R. Valdes and J. Carlos Santamarina. Particle Clogging in Radial Flow: Microscale Mechanisms. *SPE J.*, 2006.

[30] Hans M. Wyss, Daniel L. Blair, Jeffrey F. Morris, Howard A. Stone, and David A. Weitz. Mechanism for clogging of microchannels. *Phys. Rev. E - Stat. Nonlinear, Soft Matter Phys.*, 74(6):1–4, 2006.

[31] R.M. Butler. Steam-Assisted Gravity Drainage: Concept, Development, Performance And Future. *J. Can. Pet. Technol.*, 33(02):44–50, 1994.

[32] Yutaka Tsuji Clayton T. Crowe, John D. Schwarzkopf, Martin Sommerfeld. *Multiphase Flows with Droplets and Particles*. CRC Press, 2nd edition, 2011.

[33] Jaime Jimenez. The Field Performance of SAGD Projects in Canada. *2008 Int. Pet. Technol. Conf.*, (December):1, 2008.

[34] Somnath Mondal, Mukul M. Sharma, Rajesh A. Chanpura, Mehmet Parlar, and Joseph A. Ayoub. Numerical Simulations of Sand-Screen Performance in Standalone Applications. *SPE Drill. Complet.*, 26(04):472–483, 2011.

[35] V Fattahpour, M Mahmoudi, C Wang, O Kotb, M Roostaei, and A Nouri. SPE-189539-MS Comparative Study on the Performance of Different Stand-alone Sand Control Screens. 2018.

[36] U G Romanova, G Gillespie, J Sladic, T Ma, T A Solvoll, and J S Andrews. A Comparative Study of Wire Wrapped Screens vs . Slotted Liners for Steam Assisted Gravity Drainage Operations. *World Heavy Oil Congr.*, pages 1–23, 2014.

[37] M Mahmoudi, R G L Reservoir, S Nejadi, M Roostaei, and J Olsen. SPE-188167-MS Design Optimization of Slotted Liner Completions in Horizontal Wells : An Analytical Skin Factor Model Verified by Computational Fluid Dynamics and Experimental Sand Retention Tests. 2017.

[38] Rolf K Bratli and Rasmus Risnes. Stability and Failure of Sand Arches. *Spe*, pages 236–248, 1981.

[39] Yujia Guo. Effect of Stress Build-up around SAGD Wellbores on the Slotted Liner Performance. *MSc Thesis, Univ. Alberta*, 2018.

[40] Venkatachalam Ramachandran and H. Scott Fogler. Plugging by hydrodynamic bridging during flow of stable colloidal particles within cylindrical pores. *J. Fluid Mech.*, 385:129–156, 1999.

[41] Yishak Yusuf, Shadi Ansari, Michael Bayans, Reza Sabbagh, Mouhammad El Hassan, and David S Nobes. Study of Flow Convergence in Rectangular Slots using Particle Shadowgraph Velocimetry. *5th Int. Conf. Exp. Fluid Mech. – ICEFM 2018 Munich, Munich, Ger. July 2-4, 2018*, pages 1–6, 2018.

[42] Somnath Mondal. Flow of Particulate Suspensions through Constrictions : Multi-Particle Effects. 2013.

[43] M. J. Hiluer. The dynamics of sand moulding. *Int. J. Prod. Res.*, 6(2):155–164, 1967.

[44] B. Wu, S. K. Choi, Y. Feng, R. Denke, T. Barton, C. Y. Wong,

J. Boulanger, W. Yang, S. Lim, M. Zamberi, S. Shaffee, M. B. Jadid, Z. Johar, and B. B. Madon. Evaluating Sand Screen Performance Using Improved Sand Retention Test and Numerical Modelling. In *Offshore Technol. Conf. Asia*, 2016.

[45] P. Gondret, M. Lance, and L. Petit. Bouncing motion of spherical particles in fluids. *Phys. Fluids*, 14(2):643–652, 2002.

[46] Wei Wei and Ian Donald Gates. On the Relationship between Completion Design, Reservoir Characteristics, and Steam Conformance Achieved in Steam-based Recovery Processes such as SAGD, 2010.

[47] John G. Manchuk and Olena Babak. Geostatistical Modeling of Particle Size Distributions in the McMurray Formation. *CIM J.*, 4(2), 2013.

[48] Jean-luc Olsen. CFD Analysis of One Dimensional Slotted Liner Experimental Setup. 2018.

[49] Michael Leitch, Yishak Yusuf, and Yongsheng Ma. Interdisciplinary semantic model for managing the design of a steam-assisted gravity drainage tooling system. *J. Comput. Des. Eng.*, 5(1):68–79, 2018.

[50] Rajesh A Chanpura, Richard M Hodge, Jamie S. Andrews, Ezio P. Toffanin, Terje Moen, and Mehmet Parlar. A Review of Screen Selection for Standalone Applications and a New Methodology. *SPE Drill. Complet.*, (March):84–95, 2011.

[51] Mahdi Mahmoudi, Vahidoddin Fattahpour, Alireza Nouri, Ting Yao,

Beatrice Anne, Michael Leitch, and Brent Fermaniuk. New Criteria for Slotted Liner Design for Heavy Oil Thermal Production. *SPE Therm. Well Integr. Des. Symp.*, 2016.

[52] Mohan Sivagnanam, Jingyi Wang, and Ian D. Gates. On the fluid mechanics of slotted liners in horizontal wells. *Chem. Eng. Sci.*, 164:23–33, 2017.

[53] H.J. Herrmann, J. P Hovi, and Stefan Luding. *Physics of Dry Granular Media*. 1998.

[54] C. Zhu, S. C. Liang, and L. S. Fan. Particle wake effects on the drag force of an interactive particle. *Int. J. Multiph. Flow*, 20(1):117–129, 1994.

[55] O.l Levenspiel and A. Haider. Drag Coefficient and Terminal Velocity of Spherical and Nonspherical Particles. *Powder Technol.*, 58:63–70, 1989.

[56] Shadi Ansari, Michael Bayans, Faezeh Rasimarzabadi, and David S Nobes. Flow visualization of the Newtonian and non- Newtonian behavior of fluids in a Tesla-diode valve. *5th Int. Conf. Exp. Fluid Mech. – ICEFM 2018 Munich, Munich, Ger. July 2-4, 2018*, 2018.

[57] Tung V Tran, Faruk Civan, and Ian D Robb. Correlating Flowing Time and Condition for Perforation Plugging by Suspended Particles. *SPE Drill. Complet.*, 24(03):398–403, 2009.

[58] Gbedo Constant Agbangla, Éric Climent, and Patrice Bacchin. Experimental investigation of pore clogging by microparticles: Evidence for a

critical flux density of particle yielding arches and deposits. *Sep. Purif. Technol.*, 101:42–48, 2012.

[59] Alfredo Guariguata, Masika A. Pascall, Matthew W. Gilmer, Amadeu K. Sum, E. Dendy Sloan, Carolyn A. Koh, and David T. Wu. Jamming of particles in a two-dimensional fluid-driven flow. *Phys. Rev. E - Stat. Nonlinear, Soft Matter Phys.*, 86(6), 2012.

[60] Jianjun Dai and John R. Grace. Blockage of constrictions by particles in fluid-solid transport. *Int. J. Multiph. Flow*, 36(1):78–87, 2010.

[61] S.A. L. C. B. Bianco and P. M. Halleck. Mechanisms of Arch Instability and Sand Production in Two-Phase Saturated Poorly Consolidated Sandstones, 2001.

[62] Venkatachalam Ramachandran and H. Scott Fogler. Plugging by hydrodynamic bridging during flow of stable colloidal particles within cylindrical pores. *J. Fluid Mech.*, 385:129–156, 1999.

[63] Yanhui Han and Peter Cundall. Verification of two-dimensional LBM-DEM coupling approach and its application in modeling episodic sand production in borehole. *Petroleum*, 3(2):179–189, 2017.

[64] Adolfo Polillo and Ramona M Graves. Simulation of Sand Arching Mechanics Using an Elasto-Plastic Finite Element Formulation This paper presents a method to simulate sand production mechanics using an George D . Vassilellis , SPE , Richardson Operating Company James W . Crafton , SPE © 1994 . 1994.

[65] Kiwing To, Pik Yin Lai, and H. K. Pak. Jamming of granular flow in a two-dimensional hopper. *Phys. Rev. Lett.*, 86(1):71–74, 2001.

[66] A. Janda, I. Zuriguel, A. Garcimartín, L. A. Pugnaloni, and D. Maza. Jamming and critical outlet size in the discharge of a two-dimensional silo. *Epl*, 84(4), 2008.

[67] Patrick G. Lafond, Matthew W. Gilmer, Carolyn A. Koh, E. Dendy Sloan, David T. Wu, and Amadeu K. Sum. Orifice jamming of fluid-driven granular flow. *Phys. Rev. E - Stat. Nonlinear, Soft Matter Phys.*, 87(4):1–8, 2013.

[68] L. Pournin, M. Ramaioli, P. Folly, and Th M. Liebling. About the influence of friction and polydispersity on the jamming behavior of bead assemblies. *Eur. Phys. J. E*, 23(2):229–235, 2007.

[69] F. Chevoir, F. Gaulard, and N. Roussel. Flow and jamming of granular mixtures through obstacles. *Epl*, 79(1), 2007.

[70] M Roostaei, A Nouri, V Fattahpour, M Mahmoudi, and R G L Reservoir. SPE-189528-MS Sand Control Design through Assessment of Mathematical Models Representing Particle Size Distribution of Reservoir Sands. 2018.

[71] Yujia Guo, Morteza Roostaei, Alireza Nouri, Vahiddodin Fattahpour, Mahdi Mahmoudi, and Heeseok Jung. Effect of stress build-up around standalone screens on the screen performance in SAGD wells. *J. Pet. Sci. Eng.*, 171(July):325–339, 2018.

[72] Chenxi Wang, Yu Pang, Jesus Montero, Mohammad Haftani, Vahidoddin Fattahpour, Mahdi Mahmoudi, and Alireza Nouri. Impact of anisotropic stresses on the slotted liners performance in steam assisted gravity drainage process. *Soc. Pet. Eng. - SPE Therm. Well Integr. Des. Symp. 2018, TWID 2018*, 2018.

[73] Vahidoddin Fattahpour, Saman Azadbakht, Mahdi Mahmoudi, Yujia Guo, Alireza Nouri, and Michael Leitch. Effect of near wellbore effective stress on the performance of slotted liner completions in SAGD operations. *Soc. Pet. Eng. - SPE Therm. Well Integr. Des. Symp. 2016*, pages 142–153, 2016.

[74] Lei Li. Lei_Li_Denfense_Jan_15, 2018.

[75] Mohamed S. Ghidaoui, Ming Zhao, Duncan A. McInnis, and David H. Axworthy. A Review of Water Hammer Theory and Practice. *Appl. Mech. Rev.*, 58(1):49, 2005.

[76] A. B. Yu and B. H. Xu. Particle-scale modelling of gas-solid flow in fluidisation. *J. Chem. Technol. Biotechnol.*, 78(2-3):111–121, 2003.

[77] Christoph Kloss, Christoph Goniva, Alice Hager, Stefan Amberger, and Stefan Pirker. Models, algorithms and validation for opensource DEM and CFD-DEM. *Prog. Comput. Fluid Dyn. An Int. J.*, 2012.

[78] H. P. Zhu, Z. Y. Zhou, R. Y. Yang, and A. B. Yu. Discrete particle simulation of particulate systems: A review of major applications and findings. *Chem. Eng. Sci.*, 63(23):5728–5770, 2008.

[79] P.A. Cundal and O.D.L. Strack. A discrete numerical model for granular assemblies, 1979.

[80] Mohsen Bayati. Numerical Optimization of Cryogenic Separation of Oil Sands and Clay in Fluidized Beds. *Univ. Alberta MSc Thesis*, 2016.

[81] H. P. Zhu, Z. Y. Zhou, R. Y. Yang, and A. B. Yu. Discrete particle simulation of particulate systems: Theoretical developments. *Chem. Eng. Sci.*, 62(13):3378–3396, 2007.

[82] Y Tsuji, T Kawaguchi, and T Tanaka. Discrete particle simulation of two-dimensional fluidized bed. *Powder Technol.*, 77:79–87, 1993.

[83] Heng Xiao and Jin Sun. Algorithms in a robust hybrid CFD-DEM solver for particle-laden flows. *Commun. Comput. Phys.*, 2011.

[84] Tong Shan. Coupled CFD-DEM Modeling of Fluid- Particle Interaction In Geomechanics. 2015.

[85] Oleh Baran. Discrete Element Method in STAR-CCM+. *STAR Korean Conf. 2012*, 2012.

[86] Ariane Bérard, Gregory S. Patience, and Bruno Blais. Experimental methods in chemical engineering: Unresolved CFD-DEM. *Can. J. Chem. Eng.*, 98(2):424–440, 2020.

[87] Surya Deb and Danesh K. Tafti. A novel two-grid formulation for fluid-particle systems using the discrete element method. *Powder Technol.*, 246:601–616, 2013.

[88] I. F. Macdonald, M. S. El-Sayed, K. Mow, and F. A.L. Dullien. Flow through Porous Media—the Ergun Equation Revisited. *Ind. Eng. Chem. Fundam.*, 18(3):199–208, 1979.

[89] Sommerfeld. *Theoretical and Experimental Modelling of Particulate Flows.* Technical Report Lecture Series 2000-06, von Karman Institute for Fluid Dynamics, 2000.

[90] P. G. Saffman. The lift on a small sphere in a slow shear flow. *J. Fluid Mech.*, 22(2):385–400, 1965.

[91] KR Ahlert. Effects of particle impingement angle and surface wetting on solid particle erosion of AISI 1018 steel. (University of Tulsa), 1994.

[92] Vahidoddin Fattahpour, Saman Azadbakht, Mahdi Mahmoudi, Yujia Guo, and Alireza Nouri. SPE-182507-MS Effect of Near Wellbore Effective Stress on the Performance of Slotted Liner Completions in SAGD Operations. 2016.

[93] Wei Wei and Ian Donald Gates. On the Relationship between Completion Design, Reservoir Characteristics, and Steam Conformance Achieved in Steam-based Recovery Processes such as SAGD, 2010.

[94] Robert R Berg. From Reservoir Rock Properties 1. *Gulf Coast Assoc. Geol. Soc.*, XX:303–317, 1970.

[95] R Byron Bird. Transport Phenomena. *Appl. Mech. Rev.*, 55(1):R1–R4, 2002.

[96] Hossein Nourozieh, Mohammad Kariznovi, and Jalal Abedi. Density and Viscosity of Athabasca Bitumen Samples at Temperatures Up to 200C and Pressures Up to 10 MPa. *SPE Reserv. Eval. Eng.*, 18(03):375–386, 2015.

[97] Jacob Bear. *Dynamics of Fluids in Porous Media*. American Elsevier, 1988.

[98] H. Hanazaki, K. Kashimoto, and T. Okamura. Jets generated by a sphere moving vertically in a stratified fluid. *J. Fluid Mech.*, 638:173–197, 2009.

[99] A. Doostmohammadi and A. M. Ardekani. Interaction between a pair of particles settling in a stratified fluid. *Phys. Rev. E - Stat. Nonlinear, Soft Matter Phys.*, 88(2):1–10, 2013.

[100] Nikolaos D. Katopodes. Free-Surface Flow Environmental Fluid Mechanics. *Book*, 2019.

[101] A. Doostmohammadi and A. M. Ardekani. Interaction between a pair of particles settling in a stratified fluid. *Phys. Rev. E - Stat. Nonlinear, Soft Matter Phys.*, 88(2):1–11, 2013.

[102] R. Glowinski, T. W. Pan, T. I. Hesla, D. D. Joseph, and J. Périaux. A Fictitious Domain Approach to the Direct Numerical Simulation of Incompressible Viscous Flow past Moving Rigid Bodies: Application to Particulate Flow. *J. Comput. Phys.*, 2001.

[103] Pavel Vlasak and Zdenek Chara. Effect of particle size distribution and

concentration on flow behavior of dense slurries. *Part. Sci. Technol.*, 29(1):53–65, 2011.

[104] CD HALL and HARRISBERGER WH. Stability of Sand Arches. a Key To Sand Control. *JPT, J. Pet. Technol.*, 22(7):821–829, 1970.

[105] Roger Butler. SAGD comes of age! *J. Can. Pet. Technol.*, 37(7):9–12, 1998.

[106] Andrea J. Liu and Sidney R. Nagel. Granular and jammed materials. *Soft Matter*, 6(13):2869–2870, 2010.

Appendix A: definitions of terms

Oil sand and SAGD - Oil sand is a highly viscous mixture ($> 10,000\ cP$) of sand, clay, water, and bitumen[33]. This viscous oil is also called heavy oil and is immobile under reservoir conditions. Steam-assisted gravity drainage (SAGD) is a heavy oil recovery technique broadly used in Alberta, Canada. In SAGD operations, there are two horizontal wells drilled in the depth of about 300 meters in the reservoir. The wells are five meters apart, and their length is between 500 to 1000 meters. Steam is injected into the top well injection well to warm up the formation and lower the viscosity of the heavy oil. Due to gravity, heated oil flows down to the production well located underneath the injection well and get produced to the surface[105].

Sand production and sand screen - In most oil sand reservoirs, sand is produced with oil. Control and mitigation of sand production are crucial to achieving maximum well productivity as well as wellbore stability.

Sand control - Sand control, also known as sand retention, refers to the utilization of screens to cut down the sand production risks. Slotted liners (SL) and wire-wrapped screens (WWS) are two types of sand control devices commonly used for thermal oil sands recovery operations, such as SAGD, in both injection and production wells[52].

Failure mechanisms - Particle buildup and plugging (clogging) at the entrance and throughout the length of the sand screen opening (for instance slot or WWS aperture), are the common failure mechanism in sand screen devices. Plugging in sand screen device is the reduction in the open flow area

of the sand control media due to trapped sand and fines and different types of scale. It will decline the production and increase the draw-down pressure. Particle buildup also happens due to the transport of particles less than $44\mu m$ known as fines[19]. This process is referred to as fines migration. Migration, the buildup of fines and bridging could cause the plugging in the pore throats of formation and the plugging near the opening of the sand control device. This phenomenon decreases the permeability and productivity of the reservoir as well as quality performance of the sand screen device.

Granular system - Granular systems consist of commonly discrete solid and macroscopic particles ($> 100\mu m$) that interact with each other closely[19]. These systems are motivating topics of research due to their complicated rheology and showing special phenomena such as bridging and jamming[106]. They are broadly used in various industries, such as mining, oil, and gas, food and medicine. Accordingly, understanding and modelling of granular systems is an interdisciplinary research area. In most of the granular systems, fluid (gas or liquid) drives the solid particles also known as particulate flow or particle-laden flow. An example of this in heavy oil recovery techniques is the sand transport and sand retention in down-hole completions. A recognized aspect of the particulate flow is plugging or jamming which occurs in the media that particulate fluid flows as well as at the filter screen possibly used for filtering the particles. Multi-particle bridge formation on filter opening reduces the chance of plugging.

Bridging - Bridging theory and laboratory tests show that particles will bridge on a screen (filter) opening and this phenomenon will help sand control and

prevent plugging[17]. The multi-particle bridging phenomenon can be seen in Figures 1.2 and 1.3. There are definitions that help to understand and investigate bridging based on Coberly's definitions[17]. "A stable bridge is defined as a bridge which, when broken, will reform nearly fast on a stable opening. A stable opening is a screen opening size on which a stable bridge will form. The maximum opening is a screen opening size on which a bridge will not form even by obstructing the opening. The bridging range is defined as the ratio of the maximum opening to the stable opening. The bridging grain size is the spherical particle diameter which would form a stable bridge on a given filter opening" [17].